Timing and evolution of metasomatic alteration and mineralization in the Lyon Mountain Granite and related iron oxide apatite (IOA) ores; constraints from apatite and titanite U-Pb geochronology, Sm-Nd isotopes and trace-elements

by

© Angela L. Buchanan

A thesis submitted to the School of Graduate Studies

in partial fulfillment of the requirements for the degree of

Master of Science in Geology

Earth Sciences Department, Faculty of Science

Memorial University of Newfoundland

May 2015

St. John's, Newfoundland and Labrador

ABSTRACT

The Lyon Mountain granite (LMG) in the northeastern Adirondack Mountains of New York State hosts numerous low-titanium iron oxide apatite (IOA) ore deposits, with most deposits containing apatite that has unusually high rare earth element (REE) concentrations (total lanthanides > 20 wt. %, and up to 8 wt. % Y) as does titanite from the metasomatically altered host rocks (total lanthanides up to 3.4 wt. %, and up to 1.4 wt. % Y). The ores are predominately hosted by perthitic granite, which has been extensively metasomatised to albite and microcline granite by Na- and K-bearing hydrothermal fluids.

To better understand the timing and evolution of the metasomatism and subsequent mineralization, and to develop a genetic model for the formation of REE-IOA deposits, U-Pb isotope dilution thermal ionization mass spectrometry (ID-TIMS) dating of apatite and titanite, laser ablation multi collector inductively coupled plasma mass spectrometry (LA-MC-ICPMS) Sm-Nd analyses of apatite and titanite from the ore and host rocks and laser ablation inductively coupled plasma mass spectrometry (LA-ICPMS) U-Pb zircon geochronology were combined with LA-MC-ICPMS Lu-Hf isotope measurements. In addition to field and petrologic observations and newly obtained major- and trace-element data for rock forming and accessory minerals present in the ores and hosts, this integrated dataset indicates a multi-stage protracted history for the origin of these enigmatic deposits. U-Pb ID-TIMS dates of apatite and titanite show that these minerals formed during a later fluid event, likely the same event which formed the LMG

ores and the initial Nd isotopic composition of both ore and host-rock apatite, and host-rock titanite, suggests a local source for the REE.

ACKNOWLEDGEMENTS

I would like to acknowledge Peter Valley for collecting the samples for this study and for his previous detailed work on the LMG. I would also like to acknowledge John Fournelle for conducting electron microprobe analyses on the apatite and titanite, Jim Crowley for performing ID-TIMS on the apatite and titanite and Chris Fedo for his work with the CIA diagrams. I would like to express my gratitude to Phil Piccoli of the University of Maryland EPMA lab for his assistance in collecting EPMA data. I would like to recognize Wilfredo "Jiggs" Diegor, Mike Tubrett and Rebecca Lam of the CREAIT network at Memorial University and Chris Fisher for their help in LA-ICPMS and LA-MC-ICPMS data collection and reduction. I would also like to thank Matthew Steele-MacInnis and Chris Fisher for the time and effort they put into helpful comments and edits. Finally, I would like to thank my supervisor John Hanchar and committee member Roger Mason for taking the time to take me on as a student and my family and friends for their endless support. This research was made possible by a Discovery Grant to John Hanchar by the Natural Sciences and Engineers Research Council of Canada (NSERC).

Table of Contents

List of Tables

List of Figures

List of Appendices

Appendix A:

Appendix B: See supplementary data for Tables B-1 to B-7

TABLE B-7: Whole-rock geochemistry of the Lyon Mountain granite and associated rocks modified from Valley et al. (2011).

List of Abbreviations

Ab	albite
ADK	Adirondack
AMCG	anorthosite-mangerite-charnockite-granite
An	anorthite
Ap	apatite
BSE	back-scattered electron
Cc	Calcite
CCD	charge-coupled device
CCSZ	Carthage-Colton shear zone
CHUR	chondritic uniform reservoir
CL	cathodoluminescence
CPX	clinopyroxene
εHf (t)	epsilon Hf at time (t)
εNd	epsilon Nd
EDS	energy dispersive spectroscopy
EPMA	electron probe microanalyzer
Fsp	feldspar
Fl	fluorite
HFSE	high field strength element(s)
Hm	hematite
HREE	heavy rare earth element(s)
HR-ICPMS	high-resolution inductively coupled plasma mass spectrometer
ID-TIMS	isotope dilution thermal ionization mass spectrometry
IOA	Iron oxide, apatite
IOCG	Iron oxide, copper, gold
LA-ICPMS	laser ablation inductively-coupled plasma, mass spectrometry
LMG	Lyon Mountain granite
LILE	large ion lithophile element(s)
LREE	light rare earth element(s)
LA-MC-ICPMS	laser ablation multi-collector inductively-coupled mass spectrometry
MSWD	mean square of weighted deviates
Mc	microcline
Mt	magnetite
MUN	Memorial University of Newfoundland
NIST	National Institute of Standards and Technology
NYS	New York State
Or	orthoclase
Qtz	quartz
REE	rare earth element
RGB	red-green-blue
SEM	scanning electron microscope
SIMS	secondary ion mass spectrometry

ID-TIMS	isotope dilution thermal ionization mass spectrometry
Ttn	titanite
Zr	zircon

Chapter 1. Introduction

1.1 Overview

The Lyon Mountain Granite (LMG) in the northeastern Adirondack Mountains of New York State (Fig. 1-1) is host to numerous low-titanium magnetite-apatite ore deposits (e.g., Whitney and Olmsted, 1988; Valley et al., 2011). These deposits are sometimes classified as iron oxide-copper-gold (IOCG) deposits, but are perhaps more appropriately referred to as iron oxide apatite (IOA) or "Kiruna-type" (Reynolds, 2000; Harlov et al., 2002, Valley et al., 2009) deposits because they lack the Cu or Au mineralization characteristic of IOCG deposits, such as Olympic Dam, Australia (Reynolds, 2000). Iron oxide apatite ores are commonly associated with felsic volcanic or plutonic rocks (Hitzman et al., 1992) that have undergone extensive Na- and K-metasomatism. In the case of the LMG, and for this paper LMG refers to the metasomatically altered host rocks for the IOA ores, and spatially and temporarily related metasomatically altered granites. Such deposits are also commonly associated with mobilization of elements typically considered to be "immobile," including the rare earth elements (REE), Zr, and U. Thus, minerals such as apatite in the ore are commonly anomalously enriched in those elements (Foose and McLelland, 1995).

The physical and chemical processes responsible for mobilizing and subsequently concentrating immobile elements in the LMG IOA ore are unclear, and both magmatic and hydrothermal processes may have contributed. The LMG igneous protolith (prior to Na- and/or K-metasomatism) is thought to be an A-type or ferroan granitoid (Lupulescu et al., 2011), according to the criteria described by Whalen et al. (1987) and Frost and

Frost (1997; 2011). Generally, A-type granites have high concentrations of halogens (e.g., Cl, F) as well as incompatible elements such as REE, Zr, Nb, and Ta (Frost and Frost, 1997; 2011), which may have facilitated enrichment of these elements in the IOA ores. REE and high field-strength elements (HFSE) may be mobilized by hydrothermal fluids as fluoride or chloride complexes (e.g., Wood, 1990; Salvi and Williams-Jones, 1996; Willams-Jones et al., 2012), which may also have played a role in concentrating these elements in the LMG IOA ores. Valley et al. (2009) described that at least some of the minerals in the IOA ore bodies (e.g., zircon) are hydrothermal in origin. In-situ U-Pb SIMS analyses of zircon from several of the IOA ore bodies reveal that hydrothermal zircon growth occurred after LMG magmatism (~1060 Ma), with hydrothermal zircon ages between ~1039 Ma to ~1000 Ma (Valley et al., 2009; 2011). Microanalytical studies of other suspected hydrothermal minerals, such as apatite and titanite, and the rock forming minerals, may provide additional insights into the history of metasomatism in this system, and help to decipher the ultimate origins of IOA mineralization. For the purposes of this study, metasomatism is defined as the process by which compositional changes in the rock are caused by hydrothermal fluids via replacement or recrystallization of existing minerals, or precipitation of new minerals from solution.

The main objectives of the study are as follows: 1) determine the nature of the metasomatism recorded in the rock-forming and accessory minerals of the host and ore rocks and the role of this metasomatism (if any) in the formation of the LMG IOA deposits; 2) constrain potential source material(s) of the elevated REE in the IOA ore and host rock minerals (e.g., apatite and titanite) and explain why the LMG apatite are so

elevated in REE; and 3) resolve the timing of LMG emplacement, metasomatic alteration, and IOA mineralization by establishing a genetic model for the formation of REE enriched IOA deposits at the LMG with applications to other IOA deposits globally.

Constraints on the timing and evolution of the LMG are based on new high-precision U-Pb geochronologic data, from zircon, titanite, and apatite in both ore and host rock samples. The nature of the metasomatic processes is addressed using a combination of whole-rock, and rock forming (feldspar, clinopyroxene etc.) and accessory mineral geochemistry (zircon, titanite, and apatite). Finally, additional constraints on the timing and source of REE of LMG IOA deposits are gained from the Sm-Nd isotope compositions of apatite and titanite. Results are combined with earlier observations by Valley et al. (2009; 2010; 2011).

1.2 Previous work

Previous work has been completed on the samples from this study by Valley et al. (2009; 2010; 2011). Valley et al. (2009) studied the Fe-oxide (Cu, Au) mineralization in the LMG using zircon crystals obtained from the ore and adjacent host rocks. The zircon ages showed that the ore bodies were 20-60 m.y. younger than their host granites, these ages are supported by earlier work done by McLelland et al. (2001). Valley et al. (2009) concluded that it seemed unlikely that the mineralization is directly related to the emplacement of the granites and they suggested the mostly likely explanation is the ore formed from hydrothermal fluids caused by extension and orogenic collapse. The

purpose was to constrain the timing of Fe mineralization and hydrothermal alteration which provides crucial information ore genesis, crustal fluids, and the tectonic evolution of the Adirondack region.

Valley et al. (2010) focused on Lu-Hf isotopes from LMG ore and host rock zircon in order to characterize the fluids and processes that resulted in hydrothermal alteration and Fe mineralization. Most of the ore zircon revealed extremely radiogenic Hf isotopic signatures indicating that the fluids involved in the Fe mineralization likely broke down a pre-existing early LMG ore body consisting of Lu-rich apatite and clinopyroxene or the fluids were interacting with garnet bearing rocks resulting in scavenging of HFSE and REE, to create to extremely radiogenic signature. Valley et al. (2010) concluded that the presence of the radiogenic Hf in most of the ore zircon and the younger ore zircon ages indicated multiple processes involved in the ore formation and modification of pre-existing ores.

Valley et al. (2011) completed a comprehensive study of the LMG and associated Fe ore deposits. That study entailed field work, whole-rock geochemistry, individual mineral (feldspar, clinopyroxene, olivine and magnetite) EPMA analyses and U-Pb SIMS dating of LMG host granite zircon and associated rocks. Valley et al. (2011) characterized the sequence and alteration styles of the LMG and ores as well as proposed a model for emplacement. This model indicates that the LMG was emplaced at 1060-1050 Ma with the first generation of ore deposits consisting of clinopyroxene, magnetite and apatite (and lacking zircon) forming as a result of late stages of granite crystallization. Twenty to sixty million years later the LMG and the first generation Fe ores were hydrothermally altered. This younger alteration event was dominantly Na-rich and resulted in the

formation of the current Fe ore deposits from the alteration and remobilization of pre-existing LMG clinopyroxene-magnetite mineralization during continued extension of the Highlands.

1.3 Geologic Setting

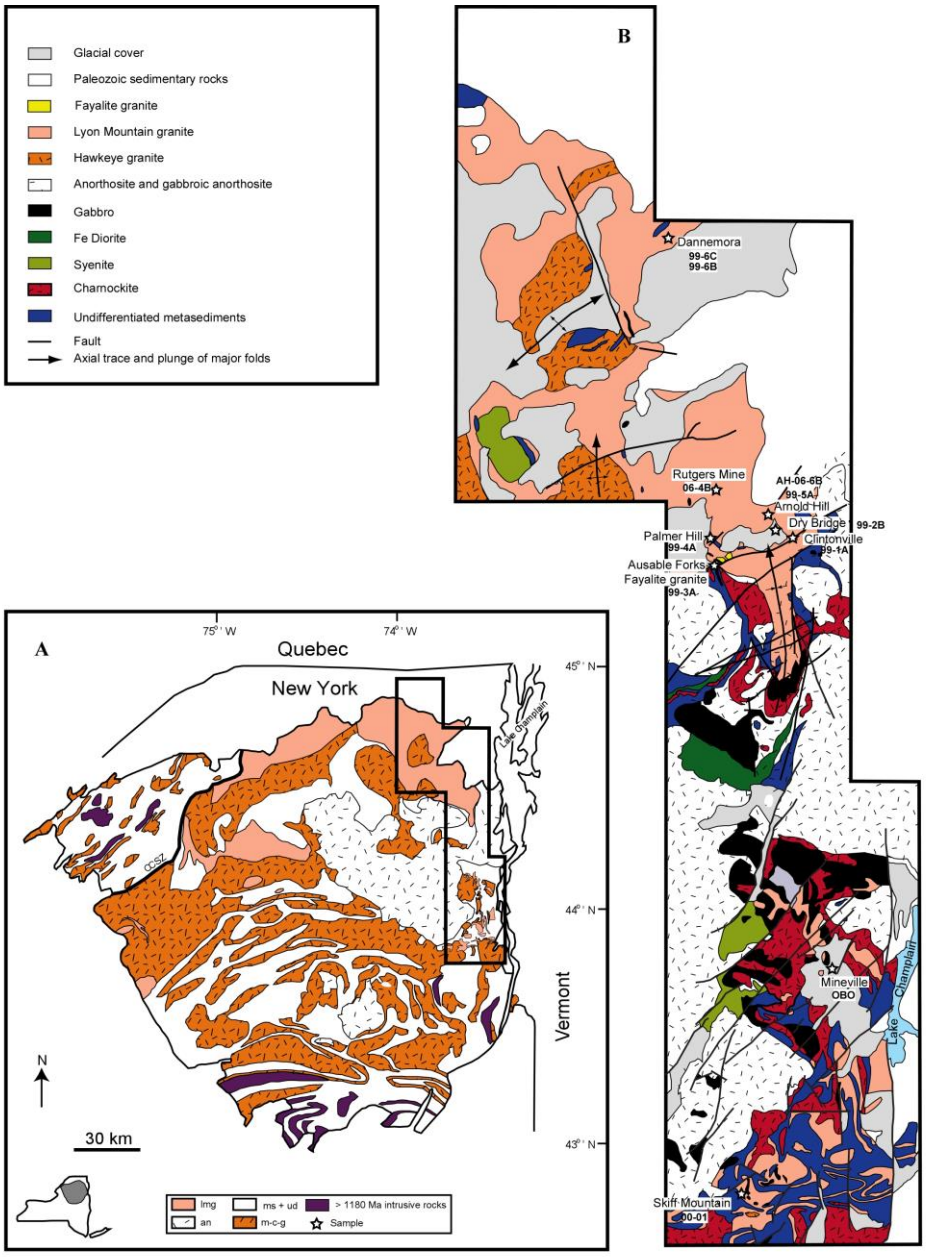

Figure 1-1**:** Geologic map of the Adirondack Mountains, New York State, after Valley et al. (2011). A) Overview map of Adirondacks, lmg: Lyon Mountain Granite; an: anorthosite; ms: metasediment; ud: undivided; m: mangerite; c: charnockite; and g: granite. B) Detailed map of the Lyon Mountain Granite and associated rocks with sample names and locations from this study.

The Adirondack Mountains comprise approximately 27,000 km^2 of the Proterozoic Grenville Province in northern New York State. The Adirondacks are divided into the Adirondack Highlands and Lowlands, which are separated by the Carthage-Colton shear zone (CCSZ; McLelland and Isachsen, 1985). During the Shawinigan Orogeny approximately 1210 to 1170 Ma (McLelland and Chiarenzelli, 1990; Rivers, 1997) most of the Adirondacks were regionally metamorphosed due to the collision of the Adirondack-Green Mountain block with the southeastern margin of Laurentia (Wasteneys et al., 1999). Following the Shawinigan Orogeny, the anorthosite-mangerite-charnockite-granite (anorthosite-mangerite-charnockite-granite [AMCG]) suite was emplaced at ~1150 Ma (e.g., McLelland et al., 2004). The AMCG suite was subsequently metamorphosed and intruded by syn- to post-tectonic granites between 1090-1040 Ma during the Ottawan Orogeny (McLelland et al., 2001). The ~1060 Ma LMG, located in the northeastern Adirondack Highlands (Fig. 1-1a), consists primarily of mesoperthite granite, which has locally been pervasively metasomatised to microcline granite and albite granite (Whitney and Olmsted, 1988; Valley et al., 2011). Most LMG lithologies from this study contain disseminated magnetite and rarely martite (pseudomorphic replacement of magnetite by hematite). Magnetite is the predominant mafic mineral in these rocks, although olivine (fayalite) and clinopyroxene (hedenbergite and aegerine-augite) occur locally. Mafic minerals usually comprise <10 vol% of the host rocks, but in some cases make up 80 vol% of the ore. The ores consist of magnetite or hematite (commonly martite) associated with highly variable amounts of apatite, microcline, quartz, clinopyroxene, amphibole, and accessory zircon. Much of the LMG and other

lithologies in the central and southern areas are crosscut by northeast trending faults of an unknown age (Isachsen and Fisher, 1971).

1.4. Rock Descriptions and Sample Petrography

Representative locally metasomatised granites, host granites and ore samples were selected for this study based on previous work completed by Valley et al. (2009; 2010; 2011). The host and other locally metasomatized granites were selected based on their compositional range in order to determine the nature of the metasomatism and its relationship to ore formation. Similarly, ores of different compositions were selected in order to study the IOA mineralization styles and their formation as outlined below.

1.4.1 Host and other locally metasomatised granites

Figure 1-2: Photographs of representative samples. A) 99-1A, perthite granite, least altered. B) 99-2B, albite granite, Na-altered. C) 99-3A, fayalite granite, weakly Na-altered. D) 99-5A, perthite granite, varying Na-alteration. E) 99-6C, microcline granite, K-altered.

The granites are fine- to medium-grained with a "sugary" equigranular texture in hand sample and thin section (Fig. 1-2a-e), and can be classified into three main types: perthite granite; microcline granite; and albite granite. Fayalite granite is also associated with the LMG, but is relatively uncommon. The perthite granite is interpreted to be the earliest mineral assemblage in the LMG consisting of perthitic feldspar, quartz, magnetite, hematite-ilmenite intergrowths, titanite, apatite, and zircon (Valley et al., 2011). The original perthite granite has experienced varying degrees of K- or Na-alteration resulting in the formation of the microcline and albite (Valley et al., 2011). The microcline granite is the result of K-alteration that has replaced the original perthitic feldspars with microcline, but commonly also exhibits Na-alteration around areas of Fe ore mineralization. Secondary minerals associated with the Na-alteration in the microcline granite consists of albite, quartz, apatite, zircon and magnetite and some microcline granite samples show evidence of another episode of later K-alteration. The K-alteration is constrained to prior to ~1040 Ma, evidenced by a plagioclase dyke that crosscuts the microcline granite and Na-alteration and Fe-mineralization associated with ore zircon formation at ~1040 Ma, which overprints the microcline granite (Valley et al., 2011).

The albite granite is also the result of near-complete replacement of the original perthitic feldspar by albite due to Na-alteration. The pervasive albitization of the albite granite in some cases precludes unequivocal assessment of which minerals are primary versus secondary in origin; however, based on petrography, it is likely much of the albite, quartz, apatite, titanite, zircon and magnetite are secondary. Na-alteration is commonly

associated with secondary albite, quartz, magnetite, zircon, apatite, titanite, amphibole, garnet and biotite. The Na-alteration event has been constrained by Valley et al. (2011) to younger than ~1047 Ma due to its crosscutting and overprinting nature, the development of albite flame lamellae in the fayalite granite and the age of the ore zircon. The fayalite granite is markedly different from the other granites of the LMG in that it contains olivine and flame perthite. It has experienced weak Na-alteration, and contains albite, quartz, fluorite, apatite and magnetite as secondary minerals.

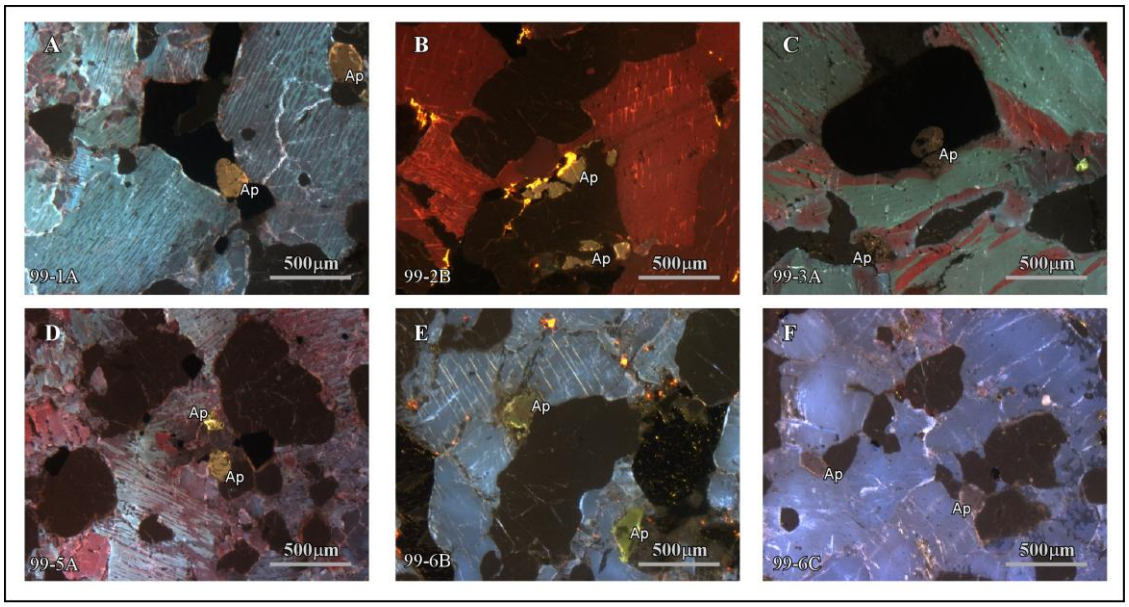

Figure 1-3: Cathodoluminescence photomicrographs of in situ apatite from host rock LMG samples. Apatite in the host rocks generally occur as discrete grains typical of igneous accessory apatite however vary in color under CL. The variation in apatite CL colors indicates the REE CL activation is overwhelming the more commonly observed Mn^{2+} CL activation (Roeder et al., 1987). Note: Albite exhibits red CL and microcline exhibits blue CL in the LMG samples. A) 99-1A. B) 99-2B. C) 99-3A. D) 99-5A. E) 99-6B. F) 99-6C.

99-1A: Sample 99-1A is a perthite granite from Clintonville (Fig. 1-2a), dated at ~1047 Ma (Valley et al., 2011). This sample has experienced the least amount of alteration among the samples, and is composed of quartz, perthite (microcline and albite), accessory magnetite, amphibole, apatite and zircon. This rock occurs distally with respect to the ore bodies and hydrothermal alteration zones (Valley et al., 2011). Apatite in this rock is yellow-orange to pale purple in CL and is associated with quartz, albite, and magnetite, and also occurs as inclusions within magnetite (Fig. 1-3a, 1-4j).

99-2B: Albite granite from Dry Bridge (Fig. 1-2b), dated at ~1055 Ma (McLelland et al., 2001). This sample has undergone extensive Na-alteration and consists almost entirely of albite plus quartz, clinopyroxene (aegerine-augite), minor magnetite and accessory apatite, titanite and zircon. Petrographic evidence of Na-alteration is observed where the original feldspar, likely perthite, has been completely replaced by multiple generations of albite (Valley et al., 2011). Apatite occurs in altered areas of the rock and ranges in CL color from yellow-orange to purple (Fig. 1-3b, 1-4k).

99-3A: Fayalite granite from Ausable Forks (Fig. 1-2c), dated at ~1047 Ma (McLelland et al., 2001). The extent of alteration of this sample is unclear but it is likely weakly Na-altered as indicated by the presence of late albite. Mineralogy of this sample includes perthite, quartz, clinopyroxene (hedenbergite), olivine (fayalite) and accessory zircon. Secondary mineralogy likely due to albitization consists of albite, quartz, magnetite, fluorite and apatite (Valley et al., 2011). Apatite in this sample is associated with alteration, in close proximity to fluorite and in some cases within quartz. CL color ranges from yellow-orange to purple (Fig. 1-3c, 1-4g).

99-5A: This sample is a perthite granite (Fig.1- 2d) from Arnold Hill, dated at ~1061 Ma (Valley et al., 2011). This sample appears to have undergone two generations of Na-alteration, as evidenced by two generations of albite in CL. Mineralogy consists of perthite, quartz, microcline, late albite, magnetite and accessory titanite, apatite and zircon. Apatite in this sample occurs along grain boundaries and associated with magnetite, and ranges in CL color from yellow-orange to purple (Fig. 1-3d, 1-4h).

99-6B: This sample is a pegmatite from Dannemora dated at ~1017 Ma (Valley et al., 2011) that is closely associated spatially with sample 99-6C below. This sample has undergone extensive K-alteration and consists dominantly of microcline with quartz, magnetite-hematite exsolution lamellae, and accessory apatite and zircon. Apatite occurs along grain boundaries and in altered areas and ranges in color from yellow to yellow-green in CL (Fig. 1-3e, 1-4i).

99-6C: This sample consists of a microcline granite from Dannemora (Fig. 1-2e), the host of pegmatite 99-6B and dated at ~1051 Ma (Valley et al., 2011). This sample has also been extensively K-altered and is composed predominantly of microcline with quartz, magnetite and accessory titanite, apatite and zircon. Apatite occurs along grain boundaries with quartz, magnetite and microcline and exhibits blue to purple CL (Fig. 1-3f, 1-4l)

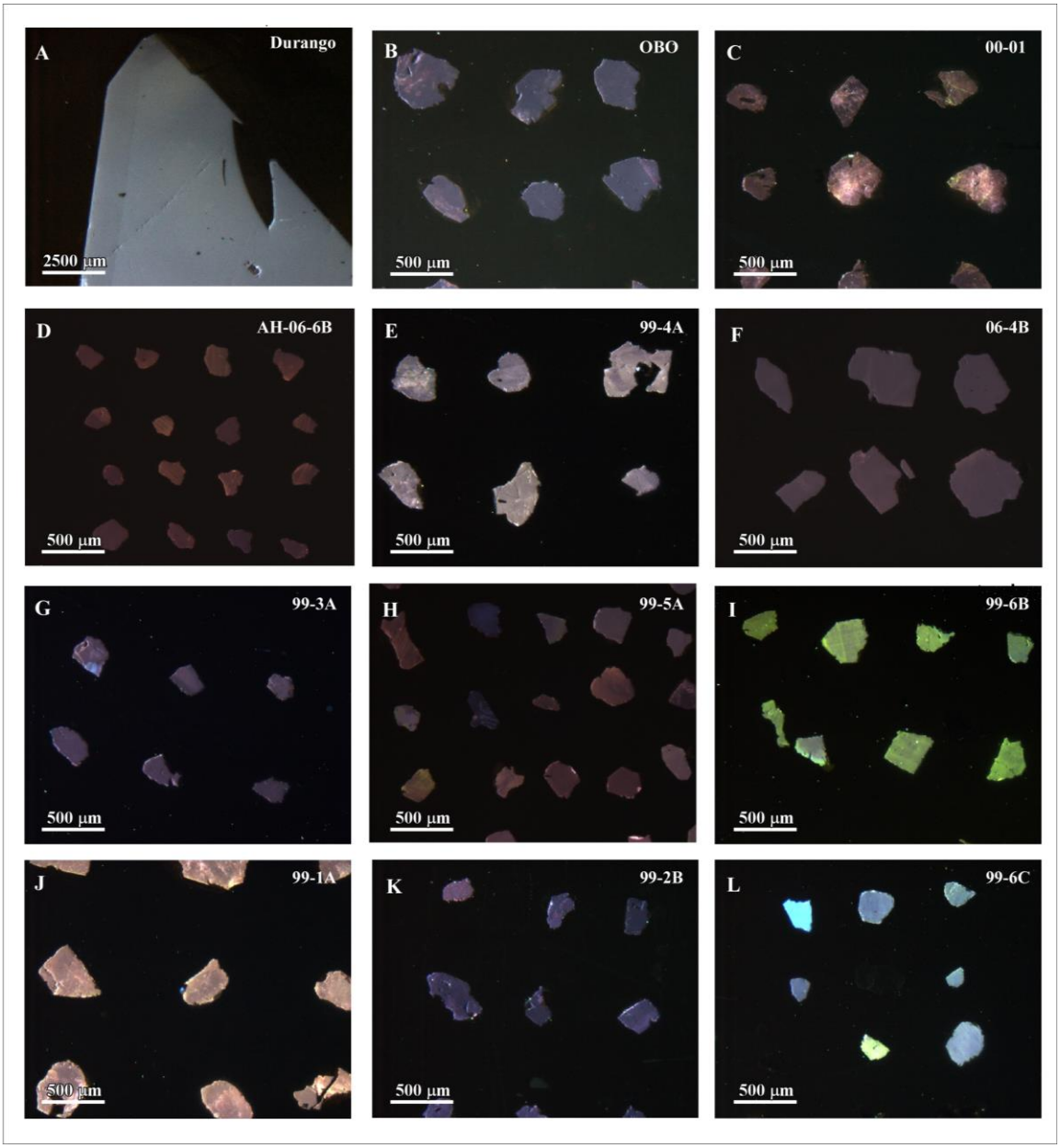

Figure 1-4: Compilation of CL photomicrographs of apatite showing the range in CL colors exhibited by apatite from the LMG with comparative photomicrograph of the Durango Standard. A) Durango apatite, used as a standard for the LA-ICPMS analyses. B) OBO, C) 00-01, D) AH-06-6B, E) 99-4A, F) 06-4B, G) 99-3A, H) 99-5A, I) 99-6B, J) 99-1A, K) 99-2B, L) 99-6C.

1.4.2 Ores

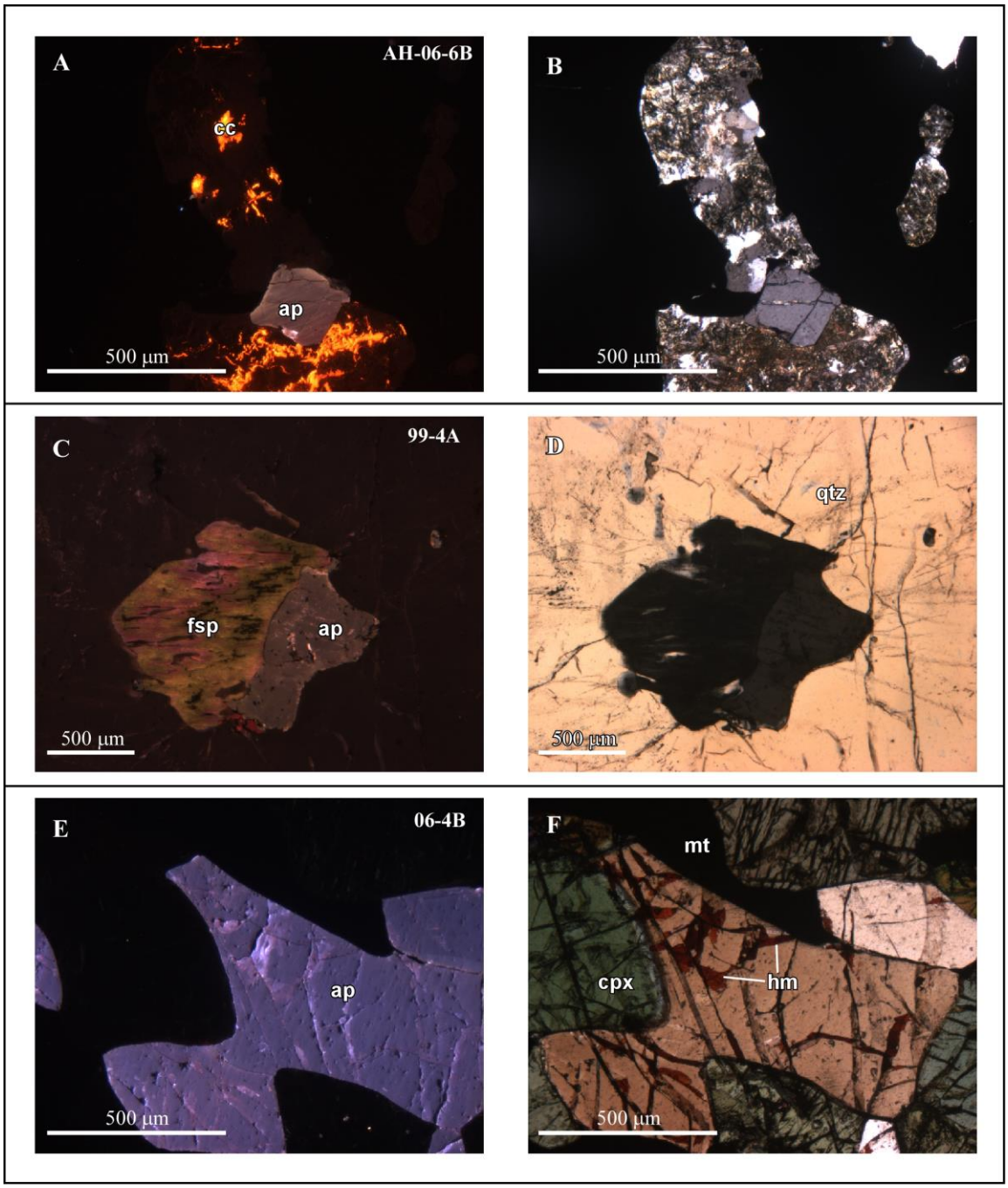

Figure 1-5**:** Cathodoluminescence photomicrographs of in situ apatite from LMG ore samples with corresponding photomicrographs in cross-polarized light (xpl). A) Apatite from ore sample AH-06-6B. B) Same as in A, in xpl. C) In situ apatite grain from ore sample 99-4A. D) Same as in

C, in xpl. E) In situ massive apatite from ore sample 06-4B with hematite occurring along fractures. F) Same as in E, in xpl.

The ore bodies are generally located parallel to the foliation of the granite host rock, with some exceptions where they cross-cut at high angles (Valley et al., 2010). The ore generally forms tubular or tabular bodies along contacts, fold hinges, fold limbs or associated with faults (Postel, 1952). Ores consist predominantly of magnetite with rare martite. All ores with the exception of 99-4A (which has been both K- and Na-altered) have been albitized and which have produced halos within their host granite that lack any Fe-bearing minerals and can range from meters to 10s of meters (Valley et al., 2011) away from the ore-host rock contact. 99-4A shows evidence of K-alteration overprinted by albitization (Valley et al., 2010).

Two types of Fe mineralization occur in the LMG: clinopyroxene-magnetite "skarn-like" type, and mineralization associated with hydrothermal Na-alteration (Valley et al., 2009). The clinopyroxene-magnetite type, represented by sample 06-4B, is thought to be an example of "primary Fe mineralization" (i.e. "skarn-like") associated with the original emplacement of the LMG, whereas the ore associated with Na-alteration (all other ore samples in this investigation) are thought to be "secondary Fe mineralization" resulting from later hydrothermal mobilization of the original "skarn-like" bodies and host granites by Na-bearing aqueous fluids (Valley et al., 2009; 2010) and are commonly associated with the formation of albite, quartz and zircon.

00-01: Skiff Mountain mine ore dated at ~1001 Ma (Valley et al., 2009), with εHf (*t*) ranging from +19.8 to +34 (Valley et al., 2010). This ore occurs near the contacts

of the LMG with the country rock units. Mineralogy consists of massive magnetite with interstitial quartz and apatite, plus rare biotite and zircon. Zircon is present in thin sections in this sample, occurring at grain boundaries with magnetite. Apatite in this sample exhibits multiple generations and is orange-purple to purple in CL (Fig. 1-4c).

99-4A: Palmer Hill mine ore dated at ~1039 Ma (Valley et al., 2009) with εHf (*t*) values ranging from +2.5 to +6.2 (Valley et al., 2010), consists of quartz, albite, magnetite, trace microcline (some replaced by albite), minor biotite and accessory fluorite, apatite and zircon. Apatite occurs in altered areas, commonly with fluorite and is purple in CL (Fig. 1-4e, Fig. 1-5c-d).

06-4B: Rutgers mine ore is composed of massive apatite, magnetite and clinopyroxene (aegerine-augite) with accessory quartz. This sample contains no zircon and therefore no U-Pb zircon dates or Lu-Hf isotopes were measured for this ore. Apatite contains needles of hematite along fractures and cracks. Clinopyroxene is partially altered to magnetite and amphibole. At the outcrop scale, enclaves of this ore appear to be partially resorbed within the perthite granite. Apatite is coarse grained and associated with clinopyroxene and magnetite, or as inclusions in amphibole, and is purple in CL (Fig. 1-4f, Fig. 1-5e-f).

OBO: Old Bed ore (OBO) dated at ~1020 Ma (Valley et al., 2009) with εHf (*t*) values ranging from +19.2 to +20.3 (Valley et al., 2010). This sample is made up of very coarse magnetite and quartz, apatite, minor clinopyroxene and accessory zircon, which in

some cases are up to 1 cm in length. In thin section, zircon occurs enclosed by coarse magnetite crystals. Apatite is associated with magnetite and is purple in CL (Fig. 1-4b).

AH-06-6B: Arnold Hill ore dated at ~1016 Ma (Valley et al., 2009) with highly radiogenic εHf (*t*) values ranging from +13.6 to +40.1 (Valley et al., 2010). This sample consists of quartz, hematite (martite), minor amphibole, clinopyroxene, chlorite and calcite, and accessory apatite and zircon. Apatite in this sample occurs in altered areas with calcite and quartz and is purple in CL (Fig. 1-4d, Fig. 1-5a-b).

Chapter 2. Methods

2.1 Sample Preparation

The accessory minerals in the analyzed LMG host and other related granites and IOA ores consist of zircon, apatite, and three host rock samples (99-2B, 99-5A, 99-6C) contain titanite, and minor sulphides. The sample preparation involved sawing into slices to remove weathered material and to prepare the material for further processing, followed by crushing in a jaw crusher to make "pea" sized fragments. Samples were then ground in a disk mill until most material was between 63-500 µm in diameter. Apatite, titanite and zircon grains were separated from the crushed rock using conventional density and magnetic methods with final hand-picking under a stereoscopic microscope. The crystals were then mounted in epoxy and polished to reveal the crystal centers. Polished 30 µm thin sections of LMG ore and host rock were also prepared for in situ microanalysis, from the same samples that were used for whole-rock and mineral-scale microanalysis.

2.2 Cathodoluminescence and Back-Scattered Electron Imaging

Cathodoluminescence microscopy was undertaken on grain mounts and thin sections using a PATCO ELM-3 Cathodoluminoscope at Memorial University of Newfoundland. Operating conditions were 12 kV, 0.7mA, a vacuum of ~7 Pa, using an unfocused beam. Images were acquired using a KAPPA DX-30C Peltier cooled charge-coupled device (CCD) camera and KAPPA Image software. All CL images were acquired

using the same red-green-blue (RGB) settings so that CL colors could be directly compared between samples.

Back-scattered electron (BSE) imaging was also used to identify fractures and inclusions within the grains and to identify analytical spot locations. The BSE imaging was done at Memorial University of Newfoundland using a FEI Quanta 400 environmental scanning electron microscope (SEM). A 20 kV accelerating voltage and 50 nA beam current were used for BSE imaging.

2.3 Electron Microprobe Analyses

At University of Maryland-College Park and University of Wisconsin-Madison the polished epoxy mounts and thin sections were subsequently coated with a 20 nm (200 Å) evaporated carbon film to prevent charge build up during imaging and microanalysis in the scanning electron microscope (SEM) and electron probe microanalyzer (EPMA). The areas analysed by EPMA on the respective minerals were precisely marked on BSE and/or CL photomicrographs, so that the analysis locations could be easily located subsequently for in situ LA-ICPMS trace-element and LA- multi collector (MC) ICP-MS analyses, and in some cases extracted from the mounts for single grain apatite or titanite U-Pb geochronology by isotope dilution thermal ionization mass spectrometry (ID-TIMS).

Rock-forming minerals in polished thin sections, in addition to zircon, apatite, and titanite samples mounted in the epoxy mounts, were analyzed for their major- and minor-element compositions at the University of Maryland, College Park, using a JEOL JXA-8900 EPMA equipped with five tuneable wavelength-dispersive X-ray spectrometers (WDS). Samples underwent initial wavelength scans and energy dispersive spectroscopy (EDS) to ensure that the proper elements were selected and measured and to identify appropriate background positions in addition to potential interferences. Two or more analyses were done per mineral grain depending on textures and relationships of the grains as guided by the BSE and/or CL images. Feldspars were analyzed for Si, Al, Fe, Mg, Mn, Ca, Na, K, Ti, Sr and Ba. Clinopyroxene and olivine were analyzed for the same elements as the feldspar except Ni and Cr instead of Sr and Ba. For zircon, Zr, Si, and Hf were measured and in some samples U and Y were also measured. For apatite, Fe, Si, Cl, F, Mn, Na, Ca, As, S, Mg, Ti, Al and P were analyzed. For titanite, the same elements as apatite minus P were measured. For fluorite, F, Fe, Si, Ca, Mn, Na, Ti, Mg and Al were analyzed. The operating conditions were an accelerating voltage of 15 kV, a Faraday cup current of 20 nA, and a beam diameter of up to 20 microns. Twenty-second count-times on peak and background were used for all the elements that were measured. Natural mineral standards were used, and the matrix correction algorithm of Armstrong/Love Scott phi-rho-z (Armstrong, 1988) was used for all analyzes. Oxygen equivalent from halogens (F/Cl/Br/I) was subtracted in the matrix correction. The standards used were natural Johnstown meteorite hypersthene (NMNH 746), Kakanui (New Zealand) hornblende (NMNH 143965), Engel's amphibole (USGS AMEN), Kakanui (New Zealand) augite (NMNH 122142), Natural Bridge (New York) diopside (NMNH

117733), Broken Hill (Australia) rhodonite (USGS PXBH), San Carlos (Arizona) forsterite (NMNH 111312/444), Rockport (Massachusetts) fayalite (NMNH 85276), Brazilian scapolite (NMNH R-6600-1(4)), Tiburon Peninsula albite (USGS FSTA), Durango (Mexico) apatite (NMNH 104021(3)), Hemet Quad (California) sphene (USGS SPHC), Astimex fluorite, microcline (unknown locality) (NMNH 143966), Lake County (Oregon) plagioclase (NMNH 115900), strontianite (Austria) (R-10065), and barium glass (Geophysical Lab).

Additional grains of apatite and titanite were also mounted in 25 mm diameter epoxy mounts and analyzed with wavelength dispersive spectrometry (WDS) using a five spectrometer tuneable Cameca SX50/51 EPMA, with Probe for EPMA software, at the University Wisconsin-Madison Department of Geoscience. Either a focused (titanite), or a 20 micrometer diameter (apatite), beam was used, with an accelerating voltage of 15 kV with a Faraday cup current of 20 nA was used. The standards used for titanite EPMA were: Renfrew titanite, jadeite, Kilbourne olivine, Hanchar synthetic hafnon, synthetic tephroite, hematite, F-topaz, CePO4 (USNM 168484 (and YPO4 (USNM 168499). The standards used for the apatite EPMA were: garnet (Rota, Hungary), Durango, Mexico, fluorapatite (Wards 104021), $CePO_4$ (USNM 168484), $DyPO_4$ (USNM 168485), $ErPO_4$ (USNM 168486), $GdPO_4$ (USNM 168488), $LaPO_4$ (USNM 168490), $NdPO_4$ (USNM 168492) $PrPO_4$ (USNM 168493), $SmPO_4$ (USNM 168494), and YPO_4 (USNM 168499). A counting time of 10 seconds was used for each analysis, with a 10 second off-peak interval to collect the background. The off peak correction method was linear for P K-α, Si K-α, F K-α, Ce L-α, Ca K-α, Y L-α, Pr L-α, Nd L-α, Sm L-α, Dy L-α, and Er L-α, and

average method was used for Fe K-α, La L-α, Gd L-α. Unknown and standard intensities were corrected for dead time.

Standard intensities were corrected for drift over time. Interference corrections were applied to Si for interference by Y, to La for interference by Nd, to Pr for interference by La, to Sm for interference by Ce and Pr, to Gd for interference by La, Ce, Nd, to Fe for interference by Dy, Nd, to Dy for interference by Ce, to Er for interference by Sm, and to F for interference by Ce. These interferences were more significant in these samples than in more typical apatite, because of their high REE contents (see Results section below).

In complicated multi-peak wavelength ranges (i.e., at ranges where multiple element peaks are clustered or overlapping), this requires precise mathematical curve fitting. For example, in some of the LMG apatite samples, the concentrations of Ce were high enough to cause a significant interference from Ce M_z on F K_α. This complication was addressed by determining the proper Ce overlap correction for F, in order to calculate accurate fluorine concentrations.

Oxygen was calculated by cation stoichiometry and included in the matrix correction. Oxygen equivalent from halogens (F/Cl/Br/I) was subtracted in the matrix correction. The matrix correction method was Armstrong/Love Scott phi-rho-z (Armstrong, 1988) and the mass absorption coefficients dataset was LINEMU Henke et al. (1982) < 10KeV / CITZMU > 10KeV.

2.4 Laser Ablation Inductively Coupled Plasma Mass Spectrometry

Subsequent to the EPMA analyses, minor- and trace-element concentrations were determined using LA-ICPMS. The 25 mm diameter polished epoxy mounts containing zircon, apatite, and titanite, and polished thin sections from the LMG host rock and ore that were used for the EPMA analyses were analyzed at the Mineral Analyses Facility – Bruneau Innovation Centre (MAF-IIC) at Memorial University of Newfoundland. The analyses were done using a Thermo-Finnigan ELEMENT XR, a high-resolution double focusing magnetic sector inductively coupled plasma mass spectrometer (HR-ICP-MS) coupled to a GEOLAS 193 nm Excimer laser ablation system. The ablated material was transported to the ICP-MS using He gas with a flow rate of 1.25 l/min, with additional Ar make-up gas added after the ablation cell prior to introduction into the ICP-MS. A laser spot size of 40 um was used with energy density of approximately 3 J/cm^2 with a laser repetition rate of 8-10 Hz. Time-resolved intensity data were acquired by peak-jumping in a combination of pulse-counting and analogue modes, depending on signal strength, with one point measured per peak.

The LA-ICPMS data were acquired and viewed graphically as counts per second (CPS) vs. time. As the data were collected, the plot was refreshed at rapid time intervals to approximate a real-time view of the data acquisition. The ICP-MS was run for about 40 seconds before the laser aperture was opened, to collect adequate background readings. Since the laser ablates into the sample over time, the x-axis time on the data acquisition plot is a proxy for depth as well as time. Thus, if an analyzed grain contained an inclusion within the analytical volume, the inclusion was detected as spike in the

monitored constituent isotopes. In this case, the time interval integrated was selected so as to avoid the "contamination" effect of the inclusion, and thus obtain the real signal of the mineral grain of interest.

The CaO concentrations determined by the EPMA for clinopyroxene, apatite and titanite, SiO_2 for olivine, K-feldspar, and plagioclase, and Hf for zircon, were used as internal standards to normalize counts to concentrations for the trace-element LA-ICPMS analyses. Elements in high abundance (e.g., some REEs in the apatite samples, Hf in zircon) were analyzed in analogue mode to avoid tripping the detector, whereas the true trace-elements were analyzed using digital counting mode. For calibration, National Institute of Standards in Technology (NIST) 610 glass and 612 glasses (Pearce et al., 1997) were used. External reference materials (i.e., secondary standards) used to assess the precision and accuracy of the LA-ICPMS analyses included, "MUN Sludyanka", Siberia apatite (Dempster et al., 2003), 91500 zircon (Wiedenbeck et al., 1995; 2004), and BCR-2G (Pearce et al., 1997; Jochum et al., 2005).

The data acquisition methodology used an analytical sequence of two analyses of the NIST 600 series glasses, one of the external reference materials, followed by analyses of 14 unknowns, closing the sequence with a repetition of the external reference materials, followed by two analyses of the NIST 600 series glasses.

The MUN Sludyanka apatite, 91500 zircon, and BCR-2G glass, were analysed as noted above, and are part of a long-term monitoring of the trace-element geochemistry of these materials done over the past 15 years in the LA-ICPMS facility at Memorial

University (Table A-1 and A-2, Fig. A-2a and b). The error when measuring homogeneous materials is estimated to be ~2-3 % relative standard deviation, based on the reproducibility of results for the above mentioned materials measured periodically over the past 15 years by J.M. Hanchar at the LA-ICPMS facility at Memorial University.

The LA-ICPMS data were reduced using the in-house developed CONVERT and LAMTRACE spreadsheet programs, which employ procedures described by van Achterbergh et al. (2001). LAMTRACE allows selection of representative signal intervals, background subtraction, and internal standard correction for ablation yield differences, instrument sensitivity drift during the analytical session, and perform calculations converting count rates into concentrations by reference to the standards.

There are inherent limitations in the data quality of the analyses done using the methods described above. The EPMA results are generally very accurate with high spatial resolution, but of lower precision than LA-ICPMS, whereas the LA-ICPMS data are high precision, and depending on the element analyzed, also of high accuracy but with poorer spatial resolution due to the relatively large crater (e.g., 40 μm diameter and ~45 μm depth) made by the laser during analysis. Because the CaO values determined by EPMA were used to normalize counts to concentration for the LA-ICP-MS apatite analyses, for example, it was necessary to ensure that the most precise and accurate CaO values are chosen. Any inaccuracy in the CaO values from the EPMA would be propagated through the ICP-MS data reduction. However, the variations in CaO, typically much less than 1% (e.g., 46.90 versus 47.02 % CaO, a difference of 0.3 % relative), has a small effect on the normalized LA-ICPMS trace-element concentrations.

2.5 LA-MC-ICPMS Sm-Nd Isotopic Analyses

Apatite and titanite Sm-Nd isotopic analyses were done on individual grains using the methodology discussed by Fisher et al. (2011) at the MAF-IIC facility at Memorial University of Newfoundland using a Thermo-Finnigan NEPTUNE double focusing MC-ICPMS. The NEPTUNE was operated in static mode using 65 cycles with an integration time of 2 s per cycle. The nine Faraday cup configuration of this instrument allows the simultaneous collection of isotopes of Nd, Sm, Eu, and Gd. Thus, both Sm-Nd isotopic data as well as the relative Eu/Eu* can be determined from each analysis. Samples were ablated for 60 s using the same GEOLAS 193 nm Excimer laser ablation system mentioned above, with the remainder of the cycles used to measure the gas background. The ablated material was transported to the MC-ICPMS using He as a carrier gas (1.25 l/min), with Ar added just prior to introduction into the MC-ICPMS. The mean background intensity of each mass was subtracted from the intensity of the same mass measured for each measurement cycle. The beam was held stationary on the sample surface and ablation was done at a frequency of 4-6 Hz with an energy density of ~5 J/cm^2 and a beam diameter of 20-150 μm depending on the Nd content of the target material and the availability of suitable regions free of inclusions, cracks, etc., in the crystals for the in situ analyses.

The Sm-Nd data were reduced using a custom data-reduction scheme written in Iolite (available upon request from D.J. Goudie [d.goudie@mun.ca] or J.M. Hanchar

[jhanchar@mun.ca; jmhanchar@gmail.com]). Details of the data reduction scheme are described in Fisher et al. (2011).

2.6 U-Pb Geochronology

2.6.1 ID-TIMS

U-Pb geochronology was done using isotope dilution thermal ionization mass spectrometry (ID-TIMS) at Boise State University with single grains and fragments of titanite and apatite from the LMG ore and host rocks. Titanite grains and fragments were put in 3 ml Teflon PFA beakers, ultrasonically cleaned for an hour in ultrapure H_2O, immersed in 3.5 M HNO_3 and fluxed on a hotplate at 80°C for 15 minutes. The HNO_3 was removed; the grains and fragments were rinsed twice in ultrapure H_2O, loaded into 300 µl Teflon PFA microcapsules, and spiked with the mixed Boise State ^{233}U-^{235}U-^{205}Pb tracer solution. Grains and fragments were dissolved in Parr vessels in 120 µl of 29 M HF with a trace of 3.5 M HNO_3 at 220°C for 48 hours, dried to fluorides, and then re-dissolved in 6 M HCl at 180°C overnight. U and Pb were separated from the titanite matrix using an HCl- and HBr-based anion-exchange chromatographic procedure (Krogh, 1973), eluted separately, and dried with 2 µl of 0.05 N H_3PO_4.

Apatite grains and fragments of grains were put in 3 ml Teflon PFA beakers, ultrasonically cleaned for an hour in ultrapure H_2O, rinsed twice in ultrapure H_2O, loaded into 300 µl Teflon PFA microcapsules, and spiked with the mixed Boise State ^{233}U-^{235}U-

^{205}Pb tracer solution. Grains and fragments were dissolved in 120 µl of 6 M HCl at 180°C for 48 hours, dried to fluorides, and then re-dissolved in 6 M HCl at 180°C overnight. U and Pb were separated from the apatite matrix using an HCl- and HBr-based anion-exchange chromatographic procedure (Krogh, 1973), eluted separately, and dried with 2 µl of 0.05 N H_3PO_4. Pb and U were loaded on a single outgassed Re filament in 2 µl of a silica-gel/phosphoric acid mixture (Gerstenberger and Haase, 1997), and U and Pb isotopic measurements made on a GV Isoprobe-T multicollector thermal ionization mass spectrometer equipped with an ion-counting Daly detector. Pb isotopes in analyses with smaller amounts of radiogenic Pb were measured by peak-jumping all isotopes on the Daly detector for 100 to 150 cycles, and corrected for 0.15 ± 0.03%/ a.m.u. (1σ) mass fractionation. Pb isotopes in analyses with larger amounts of radiogenic Pb were measured by a Faraday-Daly routine that cycles 150-200 times between placing mass 204 in the axial Daly collector and masses 205-208 on the H1-H4 Faraday detectors to placing mass 205 in the axial Daly and masses 206-208 in the H1-H3 Faradays, providing real-time Daly gain correction. These results were corrected for 0.10 ± 0.02%/a.m.u. (1σ) mass fractionation. Transitory isobaric interferences due to high-molecular weight organics, particularly on masses ^{204}Pb and ^{207}Pb, disappeared within approximately 30 cycles, while ionization efficiency averaged 10^4 cps/pg of each Pb isotope. Linearity (to ≥1.4 x 10^6 cps) and the associated deadtime correction of the Daly detector were monitored by repeated analyses of NBS982, and have been constant since installation. Uranium was analyzed as UO_2^+ ions in static Faraday mode on 10^{11} ohm resistors for 150 to 200 cycles, and corrected for isobaric interference of $^{233}U^{18}O^{16}O$ on $^{235}U^{16}O^{16}O$ with an

$^{18}O/^{16}O$ of 0.00206. Ionization efficiency averaged 20 mV/ng of each U isotope. U mass fractionation was corrected using the known $^{233}U/^{235}U$ ratio of the tracer solution.

The U-Pb dates and uncertainties were calculated using the algorithms of Schmitz and Schoene (2007), a $^{235}U/^{205}Pb$ ratio for the Boise State tracer solution of 77.93, and the U decay constants recommended by Jaffey et al. (1971). $^{206}Pb/^{238}U$ ratios and dates were corrected for initial ^{230}Th disequilibrium using a Th/U[magma] of three using the algorithms of Crowley et al. (2007), resulting in an increase in the $^{206}Pb/^{238}U$ dates of 0.08 Ma. All common Pb in the analyses was assigned to the titanite and apatite with a composition determined by Stacey and Kramers (1975), except for 0.6 pg that was assigned to laboratory blank and subtracted based on the measured laboratory Pb isotopic composition and associated uncertainty. Uranium blanks are difficult to precisely measure, but are assumed to be 0.07 pg.

2.6.2 LA-ICPMS U-Pb analyses

The U-Pb ages on selected zircon crystals were determined at the MAF-IIC facility at Memorial University of Newfoundland. U-Pb and Pb isotopic ratios were measured using a Finnigan ELEMENT XR double focusing magnetic sector field ICP-MS coupled to GeoLas 193 nm ArF Excimer laser. Two different methods were applied to these samples over the course of this study. In the first method, described in detail in Souders et al. (2013), a 10 μm laser beam was rastered over the sample surface at a velocity of 10 μm/s to create a 40 x 40 μm^2 ablation surface (and area of 1600 μm^2), in order to reduce U-Pb fractionation and reduce the depth of the laser pit. Data were

calibrated using a mixed U-Ti-Bi spike solution, which is aspirated during analysis and mixed with the ablated sample prior to introduction to the plasma source. A second method described by Goudie et al. (2014) was employed where a 30 μm laser spot is held stationary over the sample during analyses, which minimized the surface area sampled (~700 μm^2), allowing small features identified in BSE imaging to be analyzed, provided these features are ~30um thick. These analyses were done using an in-house developed reduced-volume laser ablation cell insert which helped reduce bias due to sampling position and greatly reduces the "washout" times between analyses. Analyses consisted of 30 seconds of background followed by 60 seconds of ablation. Helium was used as a carrier gas (1.25 l/min) to transport the ablated material toward the ICP-MS instrument. U-Pb data were calibrated by analyses of the Plesovice zircon standard (337 Ma) collected throughout the analytical session. Data were reduced using Iolite v. 2.15 and used the Iolite data-reduction scheme "U_Pb_Geochronology2," with a smoothed-cubic spline down-hole correction model (Paton et al., 2010). Isoplot v. 2.06 (Ludwig, 2003), was used to produce Concordia and weighted mean plots and to calculate Concordia and weighted mean ages and their uncertainties. Uncertainties of individual analyses are reported with 2σ errors; weighted average ages are calculated at the 2σ 95% confidence level.

During data reduction, each analysis was checked for any abnormal spikes which indicate ablation of inclusions or other problems such as common Pb (monitored by measuring mass 204). Contamination by common Pb is generally associated with ablating areas containing cracks, inclusions, or other imperfections in the mineral. No common Pb

correction was applied to the data; however, elevated (background corrected) signal intensity at mass 204 was monitored as a direct assessment of the common Pb concentrations and variations in concentration. All U-Pb analyses were checked and verified for the quality of the ablation signal. Only the analyses with coherent signals were retained. Th and U concentrations for the unknown zircon crystals were calibrated against analyses of zircon sample 91500.

Chapter 3. Results

3.1 Whole-rock Major-, Minor-, and Trace-Element Geochemistry

Whole-rock major-, minor-, and trace-element data from Valley et al. (2011) for the LMG host rock samples (Table 3-1) are consistent with earlier published whole-rock data for the samples that were collected at the same localities (e.g., Whitney and Olmsted, 1988; McLelland at al., 2002). The LMG consist of several rock types, metasomatic alteration styles, and Fe mineralization. Thus, there is a wide range of major- and trace-element compositions (Table 3-1). As a result of metasomatic alteration and mineralization, it is unlikely that the whole-rock data for most of the LMG samples represent the original igneous protolith compositions. However, immobile trace-element concentrations likely reflect the original elemental and/or isotopic ratios of the protolith in some samples.

Table 3-1. LMG whole-rock data, modified from Valley et al. (2011)

Sample	99-1A	99-6C	99-2B	99-5A	99-3A	99-6B	AH-06-6B	99-4A	00-01	06-4B	H-06-1C
Rock type	perthite granite	microcline granite	albite granite	mixed	fayalite granite	pegmatite	hem	mt + apt	mt + apt	cpx + mt	Hawkeye granite
Location	Clintonville	Dannemora	Dry Bridge	Arnold Hil	Ausable Forks	Dannemora	Arnold Hil	Palmer Hill	Skiff Mountain	Rutgers	Hawkeye
(wt. %)											
SiO2	71.52	68.98	71.38	68.06	70.62	64.55	11.91	18.14	10.06	20.52	71.52
Al2O3	12.27	12.73	13.34	12.70	12.32	12.33	0.97	1.42	0.72	1.21	13.15
10000*Ga/Al	3.54	3.35	4.70	4.78	5.75	4.10	42.85	20.72	106.11	46.85	3.16
Fe2O3	4.69	6.03	3.38	10.32	6.07	11.03	73.92	75.48	87.79	52.89	3.15
FeO	4.22	5.43	3.04	9.29	5.46	9.92	66.51	67.92	78.99	47.59	2.83
Fe index	0.96	0.99	0.92	0.99	1.00	0.99	0.99	1.00	1.00	0.96	0.97
MnO	0.02	0.01	0.03	0.01	0.11	0.02	0.05	0.17	0.04	0.11	0.05
MgO	0.36	0.14	0.51	0.17	0.03	0.20	1.67	0.16	0.11	4.41	0.15
CaO	1.15	0.39	3.12	0.42	1.42	0.60	1.93	0.47	1.44	14.22	1.28
Na2O	3.35	1.27	7.61	5.34	4.14	1.12	0.05	0.13	0.00	1.00	2.85
K2O	5.75	9.30	0.10	2.84	5.12	8.71	0.00	0.60	0.01	0.11	5.79
K2O/Na2O	1.72	7.32	0.01	0.53	1.24	7.78	0.00	4.62	-	0.11	2.03
TiO2	0.54	0.47	0.41	0.44	0.43	0.61	0.19	4.44	0.45	0.41	0.33
P2O5	0.14	0.10	0.07	0.04	0.05	0.16	0.66	0.33	0.92	5.48	0.07

Sample	99-1A	99-6C	99-2B	99-5A	99-3A	99-6B	AH-06-6B	99-4A	00-01	06-4B	H-06-1C
Rock type	perthite granite	microcline granite	albite granite	mixed	fayalite granite	pegmatite	hem	mt + apt	mt + apt	cpx + mt	Hawkeye granite
Location	Clintonville	Dannemora	Dry Bridge	Arnold Hil	Ausable Forks	Dannemora	Arnold Hil	Palmer Hill	Skiff Mountain	Rutgers	Hawkeye
(ppm)											
Sc	5.00	5.00	6.00	2.00	2.00	3.00	4.00	9.00	2.00	25.00	4.00
Be	2.00	0.50	6.00	2.00	5.00	0.50	7.00	0.50	0.50	23.00	1.00
V	20.00	18.00	7.00	15.52	8.00	25.72	175.00	42.00	53.92	234.00	6.00
Cr	10.00	10.00	10.00	10.00	10.00	10.00	0.00	10.00	10.00	10.00	10.00
Co	1.08	5.04	0.50	6.13	0.50	7.47	117.00	20.93	9.83	56.00	269.00
Ni	10.00	10.00	10.00	22.75	10.00	10.00	50.00	70.83	132.18	70.00	10.00
Cu	75.00	73.79	5.00	68.14	5.00	87.12	0.00	36.34	13.14	5.00	5.00
Zn	15.00	15.00	15.00	15.00	137.03	15.00	40.00	102.82	70.38	40.00	50.00
Ga	22.96	22.54	33.21	32.14	37.52	26.73	22.00	15.57	40.43	30.00	22.00
Ge	1.75	2.98	4.18	1.81	2.72	2.63	2.70	2.68	9.20	4.60	1.50
As	2.00	2.00	2.00	2.00	2.00	2.00	41.00	7.10	33.72	361.00	2.00
Mo	1.00	1.00	1.00	1.00	1.00	2.99	0.00	4.45	1.00	1.00	1.00
Ag	1.15	0.81	1.89	1.85	3.45	2.23	0.00	0.20	0.20	0.20	0.20
In	0.00	0.00	0.34	0.00	0.14	0.00	0.20	1.00	0.30	0.40	0.00
Sn	7.29	16.01	19.81	11.19	3.09	23.15	7.00	326.78	91.03	11.00	0.50
Sb	0.10	0.10	0.29	0.10	0.10	0.28	3.80	10.92	0.10	0.10	0.10
Ta	1.37	1.82	2.86	2.45	1.72	1.53	0.52	9.09	20.02	0.28	3.04
W	0.25	0.78	0.69	0.25	0.25	3.36	333.00	0.25	1.21	109.00	896.00
Tl	0.43	0.94	0.03	0.10	0.42	0.85	0.00	0.08	0.03	0.07	1.07
Bi	0.05	0.68	0.05	0.19	0.05	0.05	0.10	0.05	0.05	0.10	0.05
Pb	2.50	2.50	7.94	2.50	2.50	2.50	11.00	2.50	9.44	11.00	15.00
U	1.30	4.80	8.19	4.90	1.79	3.79	13.60	1.55	7.88	8.72	1.34
Rb	116.16	314.61	1.99	45.87	198.80	305.28	2.00	17.69	1.50	2.00	142.00
Sr	72.65	81.14	33.49	43.67	28.65	62.61	25.00	6.56	20.11	31.00	138.00
Cs	0.15	0.65	0.05	0.13	0.13	0.67	0.10	0.05	0.05	0.05	0.80
Ba	548.45	3510.00	8.11	194.34	199.83	2510.00	10.00	51.28	7.29	18.00	715.00
Y	71.53	71.48	112.52	70.56	130.51	98.64	344.00	34.08	804.20	427.00	50.40
Zr	524.71	500.34	1010.00	1060.00	1370.00	1050.00	30.00	139.57	59.01	58.00	389.00
Nb	20.57	23.46	39.49	33.83	32.48	21.26	6.80	267.59	12.20	9.00	11.50
Hf	14.69	14.02	25.16	26.55	36.10	27.06	2.50	4.42	4.54	2.40	10.90
Th	9.75	13.03	19.71	7.64	1.86	13.36	101.00	5.13	58.70	109.00	1.97
La	51.91	36.99	111.12	14.36	48.51	62.15	620.00	32.21	2300.00	298.00	27.20
Ce	112.95	80.02	204.76	50.49	132.63	110.78	1490.00	69.35	3390.00	667.00	66.00
Pr	15.61	11.29	25.64	5.97	20.92	13.93	159.00	8.81	311.40	85.50	9.61
Nd	62.91	44.87	97.26	26.10	92.26	52.92	575.00	33.65	993.36	339.00	41.80
Sm	13.39	10.20	18.78	8.53	22.69	11.64	87.90	6.32	175.67	67.50	10.20
Eu	2.49	2.07	3.08	1.91	2.92	2.37	8.40	0.77	19.49	9.17	2.58
Gd	14.13	10.76	19.60	9.77	25.51	12.82	77.50	6.70	168.23	68.50	9.75
Tb	2.30	2.01	3.30	2.12	4.37	2.35	11.40	1.06	28.28	10.70	1.75
Dy	13.09	12.00	19.20	13.05	25.74	14.66	64.50	6.05	153.30	61.60	10.10
Ho	2.67	2.50	3.92	2.73	5.22	3.12	12.20	1.25	30.67	12.50	1.93
Er	7.60	7.61	11.66	7.97	14.66	9.49	38.00	3.66	86.26	37.60	5.54
Tm	1.19	1.27	1.97	1.39	2.29	1.58	5.54	0.56	12.52	5.58	0.78
Yb	7.10	7.88	11.89	8.49	14.05	9.79	33.80	3.34	66.22	34.80	4.78
Lu	1.00	1.15	1.81	1.23	2.16	1.48	5.21	0.51	8.13	5.54	0.68

Note: A dash where a value is missing means that for that element the concentration is below the minimum detection limit.

The LMG ranges from peralkaline to peraluminous, with SiO_2 contents from 65.8-73.5 wt. %. The total alkalis range from 6.0-10.6 wt. %, with K_2O/Na_2O ratios ranging from 0.01-7.8 in the host granite and related samples. This wide range in K_2O/Na_2O may reflect Na- or K-metasomatism rather than the igneous protolith composition (Valley et al., 2011). The LMG host rocks have high Fe-index values (i.e.,

[$FeO+0.9Fe_2O_3$]/[$FeO+0.9Fe_2O_3+MgO$]; mass units) ranging from 0.92-0.99. However, LMG samples adjacent to ore bodies are depleted in Fe and contain essentially no ferromagnesian minerals within a few meters adjacent to the ore. The primarily K-altered samples (e.g., 99-6B and 99-6C) contain higher concentrations of large ion lithophile elements (LILE) such as Rb, Cs and Ba, compared to the least altered sample 99-1A, whereas Na-altered samples (e.g., 99-2B) are depleted in LILE (Table 3-1). Most of the Na-altered samples are enriched in HFSE (except Th) and have the highest whole-rock REE concentrations (Table 3-1). Both the least altered 99-1A and K-altered samples have similar REE concentrations and the ores have variable REE concentrations, depending primarily on the abundance of apatite in the ore.

The LMG host rocks are classified as A-type granites, based on the trace-element discrimination diagram for the tectonic classification of granitic rocks by Whalen et al. (1987) (Fig 3-1a). The Hawkeye granite is included as a reference point on this diagram because it crops out in the vicinity of the LMG (Fig. 1-1b) but is not considered to be LMG (locally, the Hawkeye is crosscut by the LMG; Postel, 1952). The Hawkeye granite is unaltered and has similar major- and trace-element concentrations to the LMG protolith based on whole-rock major-, minor- and trace-elements from Valley et al. (2011) and is similar isotopically (Lu-Hf) based on Valley et al. (2010). All of the LMG host rocks and the Hawkeye granite plot in the A-type granite field; however, in the LMG granite system many of the "immobile" elements appear to be mobile and this diagram may not reliably differentiate the granite types.

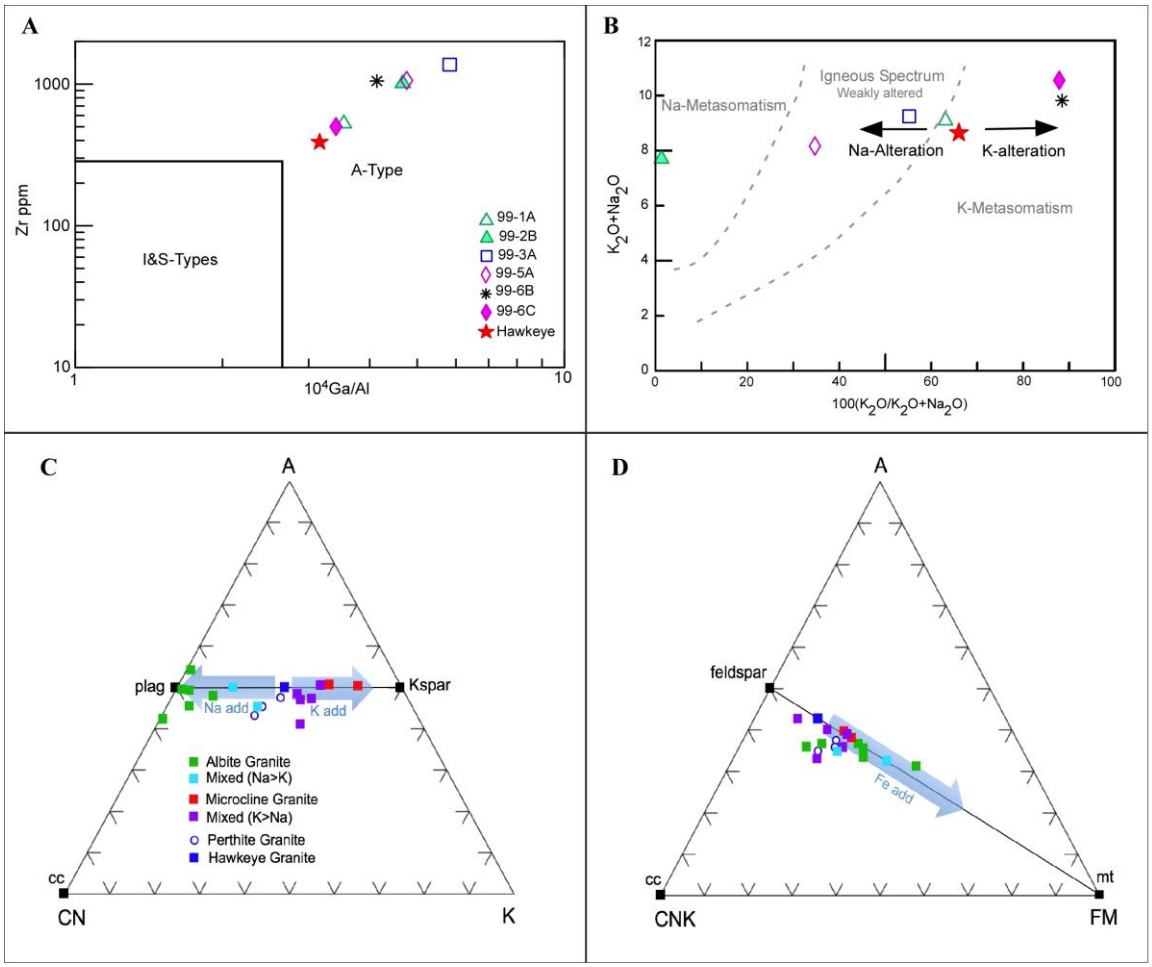

Figure 3-1: Whole-rock geochemistry plots. A) Granite classification diagram from Whalen et al. (1987). The LMG and Hawkeye granite samples fall in the "A-type granite" field. B) Modified from Hughes (1973) metasomatism discrimination diagram, demonstrating the K and Na metasomatism trends within the LMG and Hawkeye samples. C) A-CN-K (Al_2O_3-CaO*+Na_2O-K_2O) projection (Nesbitt and Young, 1989; Fedo et al., 1995) of LMG, Hawkeye Granite, and associated rocks demonstrating the effects of Na and K addition. Hawkeye Granite is used as a reference for the least altered composition. The blue left-pointing arrow shows the direction of Na addition and K subtraction, whereas the right-pointing arrow shows the direction for K addition and Na subtraction. D) A-CNK-FM (Al_2O_3-CaO*+Na_2O+K_2O-FeO+MgO) projection. Samples all lie on a mixing line between the Hawkeye Granite and magnetite at the FM apex. On average the Na-enriched samples show greater Fe addition relative to those dominated by K addition.

The LMG samples have been variably Na- and K-altered and Figure 3-1b demonstrates these alteration types found in the LMG host rocks (Hawkeye granite as a

reference point). Samples 99-3A (fayalite granite) and 99-5A plot within the igneous "weakly altered" field, whereas 99-1A (perthite granite) and the Hawkeye granite plot along the boundary between weakly altered and K-metasomatised. Sample 99-2B plots in the Na-metasomatised field, while samples 99-6B and 99-6C plot in the K-metasomatised field. The Hughes (1973) diagram in Figure 3-1b provides a useful first-order assessment of the types and degrees of metasomatism experienced by the host rocks. The Hughes diagram results are justified by field relations, petrography, and mineralogy (Valley et al., 2011) and independently reveal that sample 99-5A has experienced varying degrees of Na-alteration and possibly weak K-alteration, sample 99-3A is weakly Na-altered, while sample 99-1A represents the least altered LMG rock investigated. Additionally, feldspar in sample 99-2B is almost entirely converted to albite (Na altered), whereas feldspars in samples 99-6B and 99-6C are almost entirely microcline (K-altered).

Chemical index of alteration Al_2O_3-CaO*+Na_2O-K_2O (A-CN-K) ternary diagrams (Nesbitt and Young 1984, 1989) were originally developed to document the compositional changes in weathering profiles in response to hydrolysis reactions. Fedo et al. (1995) used these diagrams to characterize metasomatic compositional modifications in sedimentary rocks and paleosols, but the principles may be applied to igneous and metamorphic rocks. Here this approach is used to characterize the K- and Na-metasomatism of the LMG host rock samples (Fig. 3-1c-d), using whole-rock data from the present study as well as Valley (2011) (Table B-7).

The effects of the replacement of K by Na or vice versa (Nesbitt and Young, 1989; Fedo et al., 1995) are demonstrated in Figure 3-1c. The Hawkeye Granite, thought to be

the unaltered, plots approximately midway along the feldspar join (i.e., the line connecting plagioclase and K-feldspar and members), consistent with unaltered rocks of average granite composition (Fedo et al., 1995). The perthite granite, which contains some of the least altered LMG samples, also plots in this compositional space. The LMG samples scatter across the feldspar join, with compositional ratios similar to other fresh plutonic rocks, but of varied compositions (i.e., tonalite to ultrapotassic granite). The left-pointing light blue arrow shows the direction of Na addition coupled with K subtraction, i.e., albitization of the original feldspars, whereas the right-pointing arrow shows the direction for K addition and Na subtraction, by K-feldspar replacement of original feldspar. A replacement process is inferred for the compositional changes because samples that lie along the feldspar join in this projection vary only in their proportion of plagioclase and K-feldspar. If the variation in Na/K ratios reflected varied protolith compositions, then the rocks would be expected to show trace-element (including REE) ratios reflecting compositions ranging from tonalite to ultrapotassic granite. This is not the case for the LMG rocks, because the bulk-rock REE patterns for both Na- and K-altered samples share key features including fractionated LREE, a negative Eu anomaly, and relatively flat HREE (Valley et al., 2011). Assuming that the Hawkeye Granite is a reasonable approximation for unaltered LMG, the A-CN-K diagram indicates that both the Na- and K-altered rocks have experienced substantial alteration, particularly in the case of Na-altered rocks.

In Al_2O_3-CaO*+Na_2O+K_2O-FeO+MgO (A-CNK-FM) compositional space, (Fig. 3-1d; Nesbitt and Young, 1989), the LMG host rock samples lie on a mixing line between

the Hawkeye Granite and the composition of magnetite at the FM apex. In general, the Na-enriched samples, which showed a higher degree of alkali replacement, also show greater Fe addition relative to those dominated by K addition.

3.2 Zircon EPMA and LA-ICPMS Major-, Minor-, and Trace-Element Analyses

3.2.1 Host rock zircon

In transmitted light the host rock zircon grains are generally elongate and euhedral, 100-300 μm in length, colorless to brown or pink, and commonly containing fractured cores. Back-scattered electron images of the LMG host rock zircon grains show differences between the cores and rims. In some grains there is extensive radiation damage in the outer core regions adjacent to the rims (Fig. 3-2a-f), which are thought to be caused by high U concentrations in the zircon rims damaging the adjacent low-U outer cores (Nasdala et al., 2002; Nasdala et al., 2005; and Nasdala et al., 2006). The rims of the zircon grains are generally unzoned, with only rare fine scale, discontinuous growth zoning visible. The rims contain few inclusions of any type (e.g., fluid, melt, or mineral). The rims also do not show evidence of radiation damage, although many of the rims are high in U, but rarely discordant (see zircon U-Pb results below and Valley et al., 2009, and Valley et al., 2011). The cores are dark in BSE, bright in CL and are overall more fractured than the rims, but generally yield concordant U-Pb results. The cores of host-rock zircons typically show fine-scale growth zoning indicative of igneous growth (Corfu et al., 2003) and commonly contain inclusions of apatite, fluid, melt, Fe-oxides, quartz, and feldspar. In select samples, e.g. 99-2B, some zircon exhibit extensive alteration that

cross cuts the zircon grains (see Fig. 3-12f). If inclusions are present, they tend to be located in the cores of the zircon and consist of apatite, quartz, feldspar, Fe-oxide and rarely titanite or clinopyroxene. The zircon cores commonly exhibit embayments that are revealed by the brighter areas in BSE imaging embaying in the darker BSE areas of the core.

The host rock zircon rims and cores are plotted on chondrite normalized REE diagrams in Figure 3-2a-f. The REE patterns for the host zircon cores and rims are typical for igneous zircon, with overall positive slopes from La to Lu, a moderately to well-developed positive Ce anomaly, and a weak to moderately developed negative Eu anomaly (Hoskin and Schaltegger, 2003). The rims of zircon from 99-1A (Fig, 3-2a) are slightly enriched in Ce and Er to Lu, compared to the cores of these zircons. In sample 99-3A (Fig. 3-2c), two of the zircon rims are enriched in Nd to Tm compared to the cores. In all the other host-rock samples (99-2B, 99-5A, 99-6B and 99-6C) the rims are depleted in all REE except Ce, compared to the cores, the most prominent being the Na-altered samples 99-2B and 99-5A (Figs. 3-2b and 3-2d).

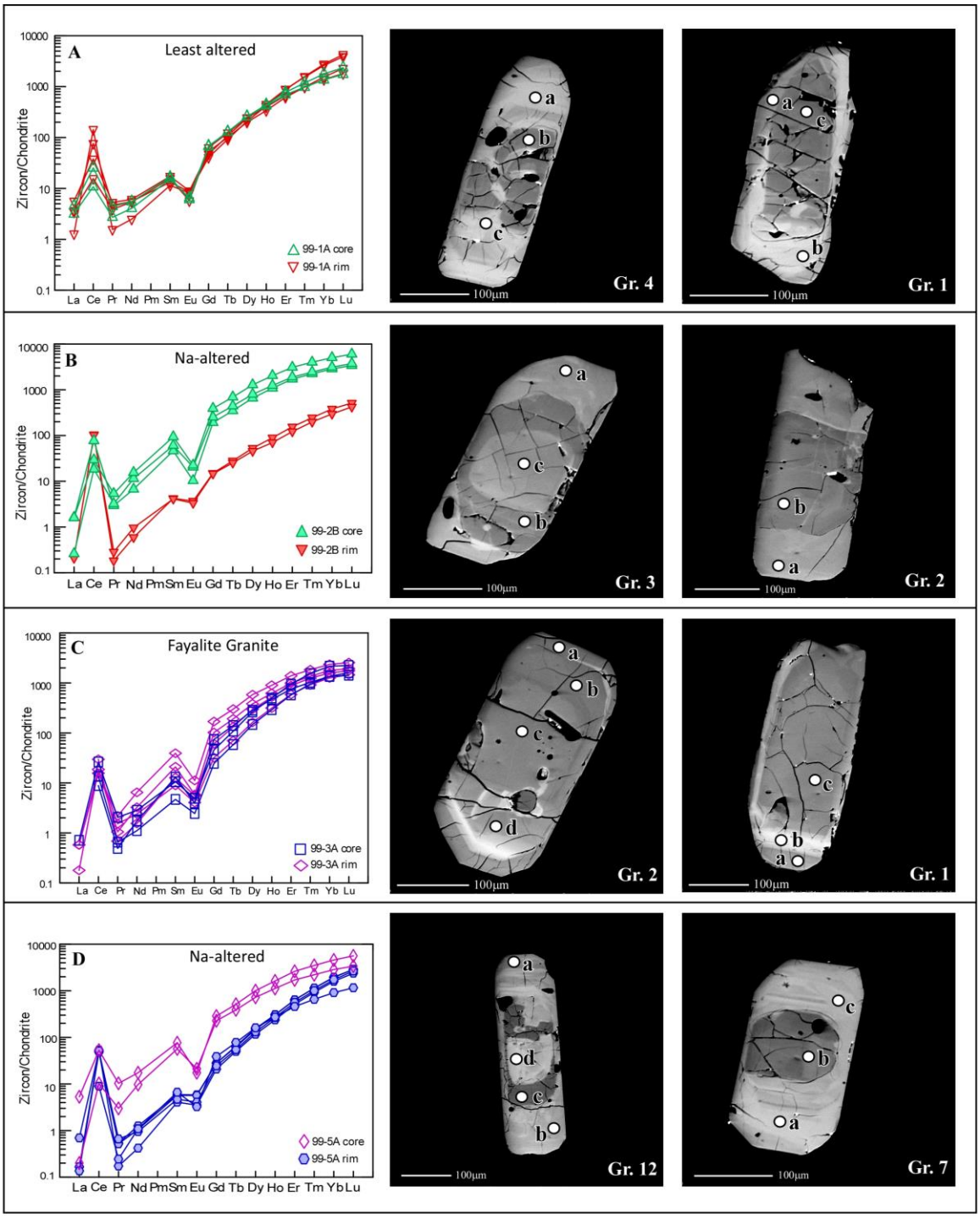
A
Least altered
Zircon/Chondrite
99-1A core
99-1A rim
Gr. 4
Gr. 1
B
Na-altered
99-2B core
99-2B rim
Gr. 3
Gr. 2
C
Fayalite Granite
99-3A core
99-3A rim
Gr. 2
Gr. 1
D
Na-altered
99-5A core
99-5A rim
Gr. 12
Gr. 7
La Ce Pr Nd Pm Sm Eu Gd Tb Dy Ho Er Tm Yb Lu
100µm

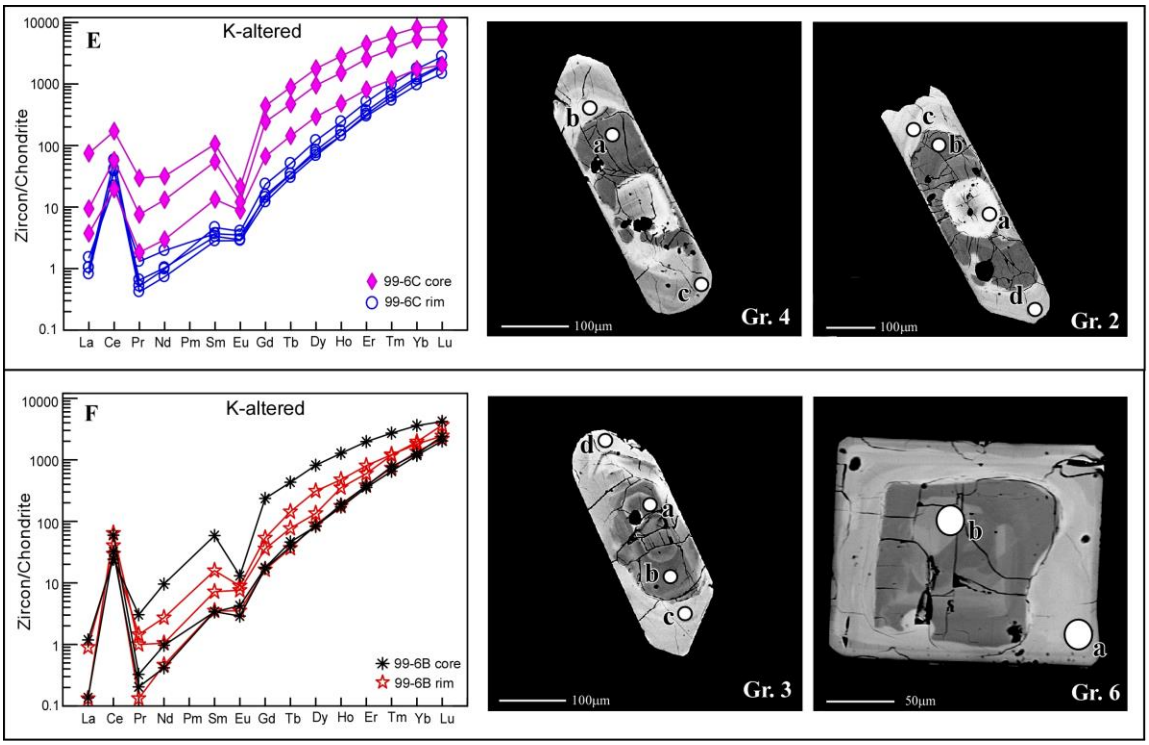

Figure 3-2: BSE images including in situ spot LA-ICPMS trace-element analyses of host rock zircon rims and cores with corresponding Anders and Grevesse (1989) chondrite normalized REE plots. A) 99-1A. B) 99-2B. C) 99-3A. D) 99-5A. E) 99-6C. F) 99-6B, zircon image Gr.6 is a cross section through 99-6B, i.e., perpendicular to the crystallographic c-axis.

Yttrium behaves similarly to the heavy REE (HREE) and is enriched in the cores but less so in the rims. Overall, Y is elevated in the LMG zircons relative to typical crustal zircon (Hoskin and Schaltegger, 2003), with core and rim values ranging from 120 to 1710 ppm Y (Table 3-2). Samples 99-1A, 99-2B and 99-3A are mostly similar in both rim and core, with generally <1000 ppm Y (with the exception of a few cores from 99-2B and 99-3A). Zircons from 99-5A, 99-6B, and 99-6C have an increase in Y in the cores and a decrease in the rims, generally with concentrations of Y <1000 ppm.

Uranium is similar in concentration between rims and cores, but U exhibits the opposite behaviour with respect to Y within individual grains, with lower U in cores and higher U concentrations in the rims. Rims overall range from 27-2802 ppm, and the cores range from 23-2559 ppm. Samples 99-2B and 99-3B show a more homogeneous U content between rims and cores (Table 3-2). The most prominent U enrichment occurs in the zircon rims in samples 99-1A, 99-5A, 99-6B, and 99-6C. These samples exhibit relatively U poor cores and U rich rims (Table 3-2). Hf in the zircon cores ranges from 546-11,757 ppm with the highest concentrations from 99-6B and 367-13,392 ppm in the rims, with the highest concentrations from 99-3A.

Table 3-2. Representative LA-ICPMS minor- and trace-element analyses of LMG host rock zircon

Sample	99-1A (Least altered)												99-2B (Na-altered)							
Grain	Gr. 1a	Gr. 1b	Gr. 1c	Gr. 2a	Gr. 2b	Gr. 2c	Gr. 4c	Gr. 4c	Gr. 4b	Gr. 6a	Gr. 6b	Gr. 6c	Gr. 1a	Gr. 2c	Gr. 3a	Gr. 3b	Gr. 3c	Gr. 5a	Gr. 5b	Gr. 6a
Zone	Rim	Rim	Core	Rim	Rim	Core	Rim	Rim	Rim	Rim	Rim	Core	Rim	Core	Rim	Rim	Core	Rim	Core	Rim
ppm																				
Fe	280	1127	925	202	-	7400	39	917	964	39	5915	39	23	-	-	-	39	70	23	31
Mn	-	77.45	7.75	-	-	7.75	-	7.75	46.47	-	15.49	-	-	-	-	-	-	-	-	-
Sc	1248	1110	1035	1005	1395	981	1157	1198	1063	1199	1440	1111	1191	1105	1112	1059	1209	1253	1117	1162
V	0.35	0.43	0.88	0.32	0.40	2.21	0.33	0.41	2.02	0.27	2.72	0.53	-	0.11	-	1.78	0.19	0.19	-	-
Ni	-	-	-	-	-	-	-	-	-	-	-	-	-	-	-	-	-	-	-	-
Sr	0.44	2.03	0.77	0.49	0.53	1.51	0.65	0.56	1.38	1.01	1.71	0.65	0.14	0.65	-	0.40	1.02	0.18	0.13	0.23
Y	665	762	762	606	1397	450	802	560	864	535	1021	701	173	1212	149	1711	248	223	114	275
Nb	2.51	16.7	4.68	12.8	2.59	4.38	16.5	7.00	16.5	8.90	11.6	20.7	0.84	3.42	0.21	15.9	8.12	0.96	0.64	1.53
Ba	0.90	0.78	1.66	0.52	-	8.79	0.22	2.05	3.69	0.16	4.56	0.62	-	-	-	-	0.07	-	-	-
La	0.86	0.81	1.06	0.48	0.07	3.70	0.30	1.32	5.28	0.23	3.97	0.36	-	0.06	0.05	0.38	0.37	0.05	-	0.02
Ce	9.44	46.1	15.2	64.8	9.39	14.0	86.7	22.8	52.4	72.7	34.5	42.7	63.2	11.1	61.7	46.3	17.6	74.9	56.1	85.4
Pr	0.38	0.46	0.43	0.19	0.22	1.38	0.15	0.52	2.81	0.11	1.45	0.34	0.02	0.32	0.03	0.29	0.53	0.05	0.02	0.03
Nd	2.52	2.60	2.56	1.09	3.43	6.67	1.16	2.85	13.9	0.82	7.89	2.26	0.28	5.33	0.45	3.13	7.24	0.52	0.22	0.41
Sm	2.31	1.96	2.43	1.18	6.40	3.98	1.69	2.54	9.50	0.99	5.14	2.20	0.62	8.90	0.61	6.78	13.76	0.85	0.51	0.86
Eu	0.32	0.48	0.34	0.33	0.29	0.63	0.46	0.50	1.74	0.46	0.92	0.45	0.21	1.14	0.19	0.58	1.25	0.32	0.17	0.33
Gd	12.45	7.98	13.1	6.73	33.0	10.3	9.26	10.4	20.1	5.56	20.98	9.07	2.95	49.6	2.87	37.6	76.8	4.32	2.13	4.49
Tb	4.48	3.35	4.71	2.81	10.9	3.35	3.92	3.66	6.49	2.11	6.91	3.47	1.02	16.1	0.92	12.6	25.2	1.30	0.67	1.51
Dy	59.4	50.8	62.6	41.8	131	42.0	57.9	48.5	77.9	32.8	87.3	50.6	12.9	193	11.1	159	311	17.0	8.63	20.2
Ho	22.1	23.2	24.5	18.7	47.9	15.4	25.0	18.8	28.3	15.1	34.6	21.7	4.97	69.1	3.91	60.3	113	6.26	3.14	7.85
Er	106	138	123	107	213	75.6	141	97.8	153	92.3	168	122	24.7	301	19.4	271	491	31.2	15.8	39.9
Tm	23.6	38.2	28.7	28.1	43.6	17.5	37.2	23.7	39.5	25.2	36.7	31.5	5.9	59.1	4.79	54.1	96.9	7.40	3.82	9.51
Yb	224	449	289	320	385	180	423	251	440	304	369	352	61.9	507	48.0	465	817	76.5	40.8	99.6
Lu	43.9	104	57.1	74.5	73.4	40.9	94.4	55.5	96.6	79.8	79.4	78.6	12.5	91.0	10.3	82.3	146	16.3	8.81	19.7
Hf	10456	6349	7917	7626	11415	8826	4235	11279	11317	3756	12169	11586	5388	4405	9597	7820	5305	5107	4517	3500
Ta	1.03	9.44	2.25	7.11	1.28	1.43	8.57	4.26	9.24	2.70	2.46	13.38	0.29	1.45	0.25	5.00	2.82	0.30	0.22	0.36
Pb	6.04	16.20	6.21	22.96	8.99	5.43	30.7	7.71	17.97	24.90	14.36	12.37	5.93	9.63	6.10	29.8	19.6	7.16	3.98	9.62
Th	59.6	157	55.9	208	78.8	43.2	294	63.7	130	227	117	109	55.1	88.9	51.5	250	173	68.1	38.3	92.9
U	143	2036	410	958	189	342	1168	555	1720	1084	373	641	396	168	417	397	354	531	357	515
Th/U	0.418	0.077	0.136	0.217	0.417	0.126	0.252	0.115	0.076	0.210	0.313	0.171	0.139	0.528	0.124	0.629	0.489	0.128	0.107	0.180

Note: A dash where a value is missing means that for that element the concentration is below the minimum detection limit.

Sample	99-2B	99-3A (Fayalite granite)																		
Grain	Gr. 6b	Gr. 4a	Gr.4b	Gr. 4c	Gr. 4d	Gr. 3a	Gr. 3b	Gr. 3c	Gr. 1a	Gr. 1b	Gr. 1c	Gr. 2a	Gr. 2b	Gr. 3c	Gr. 2d	Gr. 3a	Gr. 3b	Gr. 2a	Gr. 2b	Gr. 2c
Zone	Core	Rim	Core	Rim	Rim	Core	Rim	Rim	Rim	Core	Rim	Core	Core	Rim	Rim	Rim	Core	Rim	Rim	Core
ppm																				
Fe	847	179	86	187	358	894	3148	-	-	257	54	1073	93	995	109	365	47	101	482	-
Mn	46.47	-	-	7.75	15.49	23.24	240	15.49	-	7.75	-	30.98	-	38.73	-	15.49	7.75	-	7.75	-
Sc	1218	1354	1404	1181	1222	1286	1324	1336	1339	1279	1309	1221	947	1403	1260	917	1243	1268	1211	1132
V	-	-	-	-	-	-	-	-	-	-	-	-	-	-	-	-	-	-	-	-
Ni	-	-	-	-	-	-	-	-	-	-	-	-	-	-	-	-	-	-	-	-
Sr	3.13	0.37	0.47	0.60	0.77	0.84	4.23	0.74	0.47	0.75	0.48	0.59	0.40	1.08	0.45	0.73	0.64	0.56	0.43	0.19
Y	1907	518	495	440	590	1164	907	659	1435	891	889	865	530	737	787	772	1639	991	1122	759
Nb	55.3	4.18	34.6	26.7	18.7	8.95	54.2	25.0	5.52	42.0	22.3	3.96	26.4	24.6	26.3	21.2	8.13	12.4	5.22	3.73
Ba	1.79	-	-	0.25	-	0.29	1.22	0.28	-	0.22	-	0.58	-	-	-	0.22	-	-	-	-
La	2.98	0.10	0.05	0.17	0.07	0.13	0.22	0.05	0.14	0.17	0.01	10.0	-	0.08	-	0.12	0.08	0.04	0.04	-
Ce	84.0	5.48	7.10	6.44	11.6	12.2	10.4	16.0	9.43	15.8	16.9	40.8	8.17	18.1	17.9	11.9	12.2	11.2	8.54	5.33
Pr	1.28	0.05	0.05	0.18	0.09	0.15	0.22	0.09	0.21	0.20	0.05	4.14	0.06	0.10	0.07	0.15	0.13	0.10	0.11	0.05
Nd	9.81	0.55	0.44	1.14	0.85	1.94	1.54	0.78	3.02	1.32	0.82	16.4	0.52	1.09	0.72	1.22	2.30	1.52	1.88	0.81
Sm	8.43	1.33	0.47	0.94	1.26	4.35	1.00	1.61	5.77	1.55	2.11	6.19	0.69	2.06	1.87	1.44	5.49	3.09	3.85	1.91
Eu	1.58	0.17	0.14	0.15	0.26	0.46	0.79	0.34	0.63	0.28	0.38	0.57	0.14	0.31	0.31	0.28	0.67	0.33	0.41	0.22
Gd	37.3	9.03	3.60	3.94	7.42	25.3	5.49	9.97	33.2	9.00	14.2	20.6	4.83	11.1	11.9	7.82	32.2	20.0	23.8	14.6
Tb	13.3	3.31	1.70	1.75	3.11	8.60	2.56	4.14	10.9	3.93	5.72	6.22	2.12	4.50	4.79	3.38	12.0	6.93	7.94	5.10
Dy	175	47.4	31.5	28.8	49.2	116	49.4	61.1	141	63.8	85.0	81.3	35.7	67.9	71.9	55.7	164	92.6	107	69.4
Ho	60.1	18.1	14.8	13.1	20.5	41.3	24.3	23.9	49.9	27.7	33.5	30.0	16.2	27.3	28.8	24.4	61.8	34.5	39.1	25.9
Er	267	84.3	87.9	77.1	105	184	152	118	221	151	163	132	91.6	133	140	130	287	157	175	120
Tm	55.9	18.4	23.1	20.0	24.9	38.0	40.7	25.7	44.4	37.3	35.2	27.1	23.1	29.3	30.2	30.0	59.5	32.9	35.9	24.9
Yb	457	168	226	197	229	329	380	230	384	352	301	235	219	252	256	264	509	290	308	220
Lu	74.7	27.2	35.4	30.6	34.4	52.4	52.8	36.0	61.9	54.2	47.2	43.8	34.6	41.9	42.8	40.8	81.0	47.0	55.5	39.2
Hf	10738	4402	5223	4039	619	7141	672	5847	7175	5726	5523	8751	3372	13392	9940	3796	5329	2715	8828	8152
Ta	25.0	2.45	34.7	32.7	17.1	3.74	102	13.3	2.39	37.1	13.6	1.84	27.2	13.4	14.5	14.8	3.76	8.50	2.37	1.79
Pb	47.9	2.00	6.87	6.05	5.76	7.28	14.9	2.41	7.66	14.7	3.05	6.01	8.01	3.29	3.18	11.7	9.98	6.20	6.02	2.94
Th	577	18.5	67.9	57.5	38.8	62.6	136	23.1	70.7	133	29.9	44.1	77.2	26.9	28.5	102	87.3	57.2	50.9	24.8
U	1089	84.0	1309	1312	475	182	2802	235	163	1554	237	114	1099	218	244	668	285	353	146	76
Th/U	0.530	0.220	0.052	0.044	0.082	0.343	0.048	0.099	0.435	0.086	0.126	0.386	0.070	0.123	0.117	0.153	0.307	0.162	0.349	0.326

Sample	99-3A (Fayalite granite)													99-5A (Na-altered)						
Grain	Gr. 2d	Gr.1a	Gr. 1b	Gr. 1c	Gr. 4a	Gr. 4b	Gr. 4c	Gr. 4d	Gr. 3a	Gr. 3b	Gr. 3c	Gr. 1a	Gr. 1b	Gr. 1a	Gr. 1b	Gr. 7a	Gr. 7c	Gr. 7b	Gr. 9a	Gr. 9c
Zone	Rim	Rim	Rim	Core	-	-	-	-	-	-	-	-	-	Rim	Core	Rim	Core	Rim	Rim	Core
ppm																				
Fe	754	808	482	62	39	39	16	-	-	-	-	-	-	645	326	54	-	70	31	1003
Mn	30.98	15.49	15.49	7.75	-	-	-	-	-	-	-	-	-	7.75	-	-	-	-	-	-
Sc	1213	1065	1352	1219	1210	1191	1205	1182	1188	1163	1208	1155	1139	1118	1106	1164	1151	1157	1117	975
V	-	-	-	-	1.03	0.69	0.55	0.61	0.36	0.54	1.27	0.65	1.02	0.83	0.50	-	0.46	-	0.12	0.37
Ni	-	-	-	-	-	-	5.52	-	-	-	-	-	-	-	-	-	-	-	-	-
Sr	1.11	0.68	0.74	0.68	0.60	0.53	0.32	0.21	0.19	0.20	0.52	0.16	0.46	0.65	0.77	0.38	0.55	0.37	0.36	0.32
Y	617	550	1228	1709	760	784	243	212	185	247	567	283	610	971	1063	560	1809	562	502	1039
Nb	13.1	25.0	20.4	5.04	16.6	15.0	7.53	1.14	1.65	0.94	1.00	1.10	1.21	21.1	17.8	15.6	2.05	15.9	26.8	5.44
Ba	0.47	0.19	-	-	0.44	-	-	-	-	-	-	-	-	2.30	2.76	0.15	-	0.14	0.14	0.72
La	0.26	0.14	0.29	0.05	0.17	-	0.02	0.01	-	-	0.04	0.05	0.09	0.63	0.32	0.04	0.05	0.03	0.12	0.26
Ce	10.1	11.3	16.7	7.36	118	118	40.4	82.8	78.3	99.9	111	111	119	31.5	28.2	31.1	6.18	29.2	35.4	9.60
Pr	0.22	0.15	0.25	0.26	0.05	0.04	0.01	0.03	0.03	0.03	0.04	0.02	0.03	0.71	0.43	0.05	0.29	0.05	0.12	0.18
Nd	1.42	1.12	1.91	4.75	0.64	0.64	0.25	0.38	0.36	0.45	0.58	0.34	0.61	4.82	2.86	0.59	4.55	0.49	0.75	2.01
Sm	1.41	1.31	2.83	10.0	1.51	1.56	0.50	0.86	0.82	1.03	1.60	0.87	1.60	4.92	3.20	0.87	8.30	0.84	0.96	3.84
Eu	0.20	0.23	0.45	0.89	0.44	0.42	0.24	0.43	0.34	0.46	0.78	0.37	0.68	1.16	0.94	0.33	1.18	0.32	0.30	0.34
Gd	7.42	6.29	17.6	53.4	9.02	9.48	3.35	4.18	4.09	5.16	10.5	4.90	9.56	16.5	13.7	5.50	44.6	5.52	5.35	21.8
Tb	3.17	2.53	7.12	16.9	3.78	3.97	1.41	1.50	1.36	1.74	3.94	1.73	3.76	5.76	5.66	2.36	14.13	2.26	2.21	7.41
Dy	48.2	39.5	102.5	206.1	57.9	61.1	22.1	19.9	18.4	24.1	55.2	24.6	55.6	77.5	81.1	37.6	175.8	36.0	34.3	96.1
Ho	20.3	17.5	41.4	72.5	25.9	26.2	9.66	7.54	7.15	9.52	22.9	10.2	23.1	30.6	34.1	17.1	62.3	16.9	15.4	35.2
Er	105	93	201	305	146	151	57.7	38.7	39.0	50.3	127	53.7	125	163	188	102	272	101	92.3	162
Tm	24.5	22.1	43.1	59.0	39.3	39.9	16.5	9.69	10.5	13.2	33.7	13.3	32.6	39.4	47.8	27.4	53.4	27.7	25.2	32.9
Yb	222	204	370	497	435	444	197	103	118	146	385	144	359	434	533	316	464	319	292	295
Lu	35.6	35.3	63.3	84.3	90.1	93.5	41.7	20.3	23.1	30.2	82.4	31.0	76.1	99.7	124	69.8	82.1	70.4	68.6	53.7
Hf	562	9657	12997	4911	630	4241	1472	1725	3585	4794	4008	5710	2576	10946	10610	4605	6316	4607	4748	6816
Ta	6.48	20.3	12.0	1.94	5.87	5.17	1.89	0.37	0.58	0.36	0.32	0.41	0.35	5.39	4.51	4.08	1.07	4.18	6.81	1.73
Pb	4.49	7.39	13.8	7.16	29.4	32.4	3.72	2.74	2.68	4.38	10.4	4.15	8.71	22.5	25.5	24.4	7.68	23.3	15.4	8.03
Th	40.6	66.4	111	66.3	298	315	36.0	26.6	27.1	42.4	101	39.8	87.6	214	245	231	67.8	222	143	73.4
U	240	754	550	153	471	498	53	61	37	83	180	97	170	1341	1540	1199	131	1189	852	174
Th/U	0.169	0.088	0.201	0.434	0.633	0.633	0.674	0.436	0.724	0.512	0.562	0.409	0.516	0.159	0.159	0.192	0.516	0.186	0.168	0.422

Sample	99-5A (Na-altered)						99-6B (K-altered)													
Grain	Gr. 9d	Gr. 12a	Gr. 12b	Gr. 12c	Gr. 12d	Gr. 7b	Gr. 1a	Gr. 1b	Gr. 1a	Gr. 1d	Gr. 2a	Gr. 2b	Gr.2d	Gr. 3a	Gr. 3b	Gr. 3c	Gr. 3d	Gr. 4	Gr. 4	Gr. 4a
Zone	Core	Rim	Rim	Rim	Core	-	Rim	Core	Core	Rim	Core	Rim	Rim	Core	Core	Rim	Rim	Core	Rim	Rim
ppm																				
Fe	2658	23	39	-	2363	-	-	839	31	23	257	31	-	358	140	31	249	-	54	23
Mn	7.75	-	-	-	7.75	-	-	-	-	-	7.75	-	-	-	-	-	-	-	-	-
Sc	1041	1192	1191	1151	1319	1411	1217	1123	1160	1379	1244	1387	1324	1258	1166	1329	1329	277	368	1110
V	1.01	-	0.10	0.09	1.09	-	0.11	1.57	0.10	0.13	0.55	-	0.11	0.72	-	0.13	-	0.03	-	-
Ni	-	-	-	-	-	-	-	-	-	-	-	-	-	-	-	-	-	-	-	-
Sr	0.41	0.28	0.29	0.23	0.86	-	0.44	0.24	0.22	0.65	1.77	0.35	0.42	0.93	0.30	0.43	1.48	-	-	0.41
Y	1975	436	476	458	2724	152	474	1100	231	418	783	381	366	2031	324	342	714	598	361	305
Nb	5.43	25.71	20.35	2.32	19.91	0.71	5.54	1.14	1.94	5.54	4.27	5.24	5.16	3.63	1.85	4.58	5.02	5.57	5.30	3.44
Ba	2.19	-	-	-	1.35	-	-	0.23	-	0.12	6.49	-	-	0.88	0.35	-	6.04	-	-	0.04
La	1.29	-	0.16	-	1.25	-	-	0.03	-	0.02	6.67	0.13	0.02	0.28	0.03	-	0.21	0.03	-	-
Ce	13.8	32.3	30.8	5.39	32.0	2.89	31.4	5.24	15.5	26.3	21.7	25.2	29.1	14.6	19.4	24.4	17.8	38.6	35.9	18.1
Pr	0.83	0.02	0.07	0.02	1.01	0.01	0.02	0.06	0.01	0.02	2.23	0.04	0.01	0.30	0.02	0.01	0.14	0.10	0.03	0.01
Nd	7.11	0.20	0.45	0.51	8.13	0.19	0.28	0.94	0.12	0.24	9.80	0.26	0.27	4.47	0.20	0.22	1.27	0.49	0.45	0.15
Sm	9.75	0.60	0.69	0.98	11.3	0.42	0.73	3.04	0.30	0.64	5.67	0.70	0.51	8.63	0.50	0.52	2.33	1.06	0.50	0.43
Eu	1.74	0.20	0.23	0.18	0.98	0.24	0.25	0.95	0.13	0.20	1.48	0.18	0.19	0.73	0.16	0.20	0.50	0.43	0.24	0.12
Gd	44.9	4.10	4.82	7.61	56.4	2.41	4.63	20.8	2.06	4.00	15.3	3.76	3.54	46.2	3.37	3.21	10.5	7.02	3.48	2.88
Tb	14.7	1.82	1.99	2.82	18.6	0.86	1.88	7.47	0.94	1.75	6.46	1.56	1.43	15.6	1.41	1.33	5.20	2.79	1.68	1.13
Dy	184	28.4	31.8	38.9	244	12.2	29.2	96.3	14.7	27.3	85.5	24.9	22.6	198	20.4	21.6	75.3	32.5	20.1	17.7
Ho	63.9	13.3	14.8	15.1	90.4	5.00	13.5	32.7	6.80	12.3	29.4	11.1	10.6	70.8	9.49	9.83	26.4	19.6	10.5	8.55
Er	276	81.2	89.4	73.0	416	27.6	82.1	143	41.3	75.4	141	66.8	64.1	313	56.1	60.6	127	94.7	60.0	53.3
Tm	53.1	22.3	24.4	15.9	84.8	6.95	23.1	28.4	11.9	22.1	34.1	19.5	18.8	65.6	15.7	17.8	29.3	28.6	18.8	15.4
Yb	451	259	282	148	744	73	285	258	144	270	343	239	228	584	192	220	293	318	204	192
Lu	80.1	57.9	64.6	28.2	136	14.7	72.9	48.1	35.6	63.2	69.0	58.5	53.9	102	49.2	52.9	59.5	88.9	58.5	49.2
Hf	7515	5049	5090	7472	11210	6239	4916	8774	6921	367	10905	6075	4010	9306	10455	4137	12087	11757	12888	858
Ta	1.29	6.65	5.02	0.96	7.34	0.53	1.64	0.67	0.75	1.86	1.77	1.90	1.66	1.61	0.87	1.43	1.67	1.05	1.21	1.05
Pb	9.60	14.0	14.5	2.47	42.2	3.33	22.6	3.22	12.7	21.4	14.1	20.4	18.6	16.4	14.5	17.7	21.6	32.6	23.2	13.2
Th	91.5	132	136	21.4	347	31.8	220	27.1	112	221	160	191	176	162	131	169	186	317	215	133
U	175	702	769	63	826	91	816	68	753	993	772	833	770	294	655	782	1155	1163	1224	677
Th/U	0.522	0.188	0.178	0.342	0.420	0.348	0.270	0.398	0.149	0.222	0.208	0.229	0.229	0.550	0.200	0.216	0.161	0.273	0.176	0.197

Sample	99-6B (K-altered)				99-6C (K-altered)													
Grain	Gr. 4b	Gr. 7a	Gr. 7b	Gr. 7c	Gr. 2a	Gr. 2b	Gr. 2c	Gr. 2d	Gr. 3b	Gr. 4a	Gr. 4b	Gr. 4c	Gr. 4d	Gr. 1a	Gr. 1c	Gr. 1b	Gr. 7a	Gr. 7b
Zone	Rim	Rim	Rim	Core	Core	Core	Rim	Rim	Rim	Core	Core	Rim	Rim	Rim	Core	Core	Rim	Rim
ppm																		
Fe	47	16	16	342	684	86	23	218	23	109	350	54	23	39	-	-	-	54
Mn	-	-	-	-	7.75	-	-	-	-	23.24	30.98	-	-	-	-	-	-	7.75
Sc	1131	1109	1156	1121	1280	1266	1422	1339	1434	1174	1242	1405	1363	1237	1163	1161	1178	1292
V	0.09	-	0.16	4.12	1.70	0.21	-	0.10	0.20	1.22	0.60	0.17	0.16	-	0.44	0.36	-	0.12
Ni	-	-	-	-	-	-	-	-	-	-	-	-	-	-	-	-	-	-
Sr	0.32	0.28	0.37	0.41	2.84	0.78	0.47	0.42	0.57	1.00	3.07	0.47	0.36	0.24	0.43	0.52	0.16	0.63
Y	315	265	393	1237	117	845	470	291	506	1329	992	324	263	245	1310	1362	278	364
Nb	3.12	4.25	5.04	1.44	44.4	3.36	7.62	4.26	5.06	20.3	7.81	3.93	1.78	3.63	2.95	2.15	3.07	3.12
Ba	-	0.07	-	2.33	2.92	0.94	-	0.22	-	1.76	3.70	-	0.35	-	0.60	-	-	0.25
La	0.03	0.03	0.10	6.09	17.5	0.88	0.24	0.19	-	2.21	7.14	0.24	0.35	-	0.74	-	0.14	0.60
Ce	18.3	19.6	27.0	8.99	103	11.8	35.0	25.0	26.9	34.7	25.5	23.3	13.2	19.7	10.5	9.26	17.8	11.0
Pr	0.02	0.02	0.03	1.56	2.90	0.18	0.05	0.04	0.02	0.74	2.41	0.06	0.13	0.01	0.22	0.11	0.05	0.21
Nd	0.22	0.16	0.32	8.08	14.8	1.38	0.46	0.34	0.28	6.12	10.6	0.48	0.92	-	1.71	1.92	0.32	1.08
Sm	0.45	0.31	0.58	7.41	15.6	1.96	0.68	0.41	0.67	8.04	5.27	0.49	0.54	0.30	4.33	4.75	0.39	1.16
Eu	0.18	0.14	0.22	2.30	1.20	0.49	0.23	0.16	0.24	0.68	1.34	0.17	0.20	0.12	1.08	0.54	0.17	0.19
Gd	3.08	2.44	3.96	30.3	86.9	13.1	4.61	2.38	5.01	48.0	16.3	3.08	2.80	2.19	24.3	28.1	2.85	5.46
Tb	1.22	0.97	1.58	11.6	32.2	5.20	1.85	1.10	1.99	17.1	6.29	1.26	1.24	0.87	7.99	9.23	1.09	2.10
Dy	19.8	15.6	24.7	136	431	71.3	29.1	16.6	32.1	231	83.1	20.2	18.4	14.0	101	118	17.6	29.0
Ho	9.10	7.39	11.0	43.3	158	26.7	13.4	8.05	14.9	84.2	31.2	9.54	8.08	6.67	38.4	43.9	8.27	11.8
Er	55.5	46.2	68.3	176	710	129	81.2	51.2	90.9	406	154	57.9	47.8	42.9	178	205	49.0	61.3
Tm	15.6	13.2	19.2	34.0	150	28.5	23.7	15.1	25.9	88.8	37.0	17.1	13.1	12.4	37.2	41.5	13.4	14.9
Yb	193	165	235	298	1332	281	286	194	312	846	387	210	157	154	336	374	162	160
Lu	49.6	43.4	60.6	54.9	207	49.6	67.4	47.5	72.8	128	77.8	49.8	35.9	40.7	65.7	71.9	41.7	36.4
Hf	4197	4964	3803	8493	713	1025	5910	2487	782	3060	546	1236	1847	4372	9018	4030	10366	386
Ta	1.04	1.45	1.45	0.90	15.4	1.47	2.23	1.32	1.72	9.25	1.85	1.18	0.57	1.09	0.99	0.90	1.16	0.94
Pb	12.2	15.6	19.0	3.39	106	4.51	25.7	12.4	18.0	33.1	9.44	14.6	6.81	12.1	5.73	6.75	11.6	6.58
Th	122	155	194	27.8	949	44.4	236	123	174	310	126	143	68.6	119.5	53.9	62.3	102	69.0
U	585	776	775	86	1575	134	1015	942	1046	795	739	884	417	699	102	127	672	501
Th/U	0.209	0.199	0.250	0.324	0.603	0.332	0.232	0.131	0.167	0.390	0.170	0.162	0.164	0.171	0.528	0.489	0.152	0.138

3.2.2 Ore zircon

The ore zircon grains are distinctly different in size, shape, and BSE zoning compared to the host rock zircons (Fig. 3-3a-d). Ore zircons are more internally homogeneous and tend to be significantly larger than zircons from the host rock with some crystals up to 1 cm in length (e.g., OBO, Fig. 3-3b) showing "patchy" or little internal zoning. In transmitted light, the ore zircon grains are blocky in shape, and clear to dark brown in color (in some cases opaque). Zircon from the ore contains rare inclusions of apatite, Fe-oxide or quartz (Fig. 3-3a-d). In situ zircon was found in one ore sample 00-01 (Fig. 3-4a). This zircon is subhedral and shows weak growth zoning, has inclusions and is surrounded by magnetite. The zircon from the ore, unlike zircon from the adjacent host-rock, shows little variation in REE concentrations between the inner and outer regions and is overall chemically homogeneous. Hafnium also shows little variation between inner and outer regions (Table 3-3).

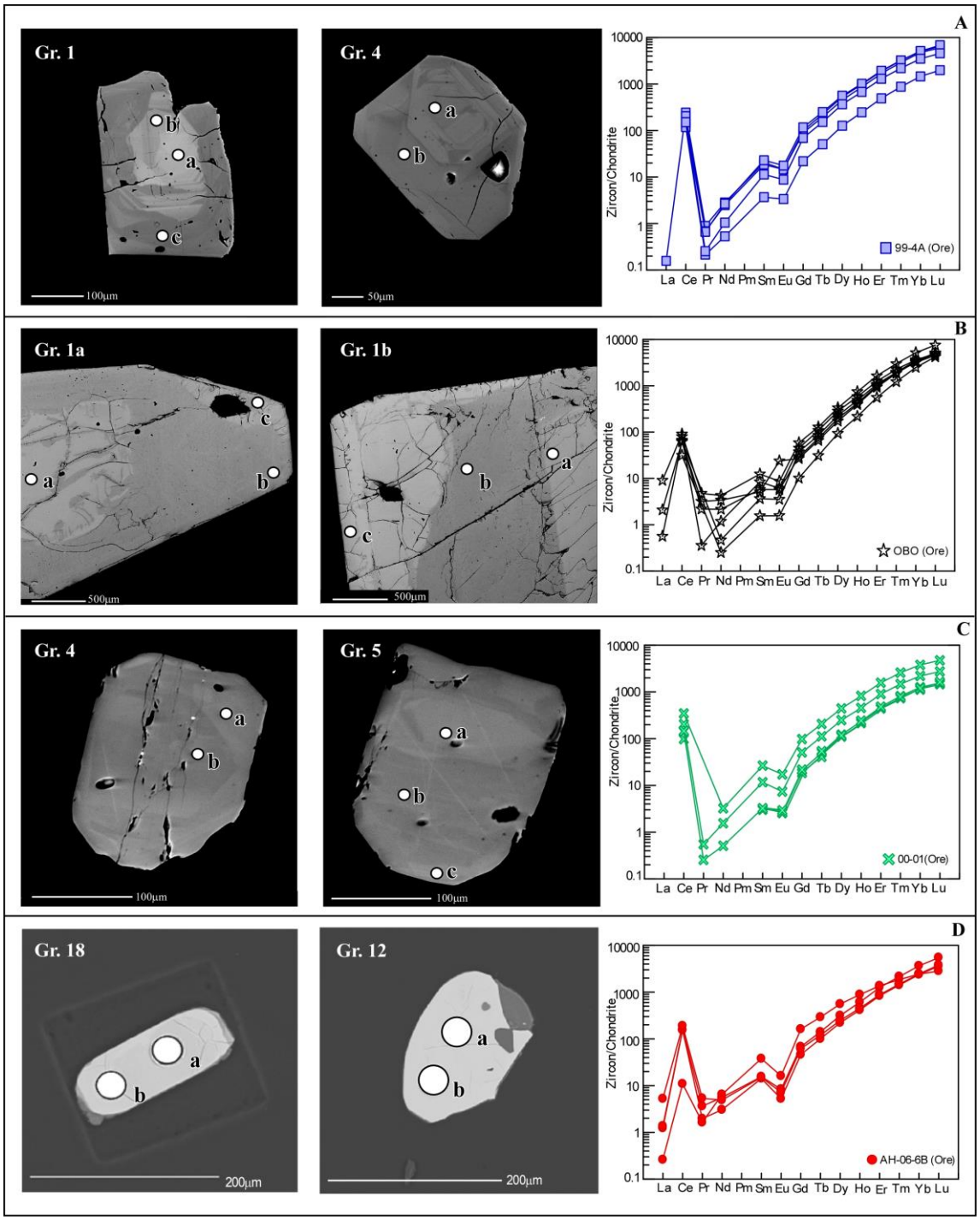

Figure 3-3: Back-scattered electron images and including in situ spot LA-ICPMS trace-element analyses of representative ore zircon with corresponding Anders and Grevesse (1989) chondrite normalized REE plots. A) 99-4A. B) OBO. C) 00-01. D) AH-06-6B.

Uranium is enriched in the ore zircon crystals relative to typical crustal zircon (Hoskin and Schaltegger, 2003) and ranges from 620 to 2760 ppm. Hf ranges from 398 to 17,048 ppm, with the highest from OBO zircon. Uranium and Y in the ore zircon, unlike the host rock zircon crystals, consistently show a trend of increasing U, Y and REE towards the outer regions. None of the ore zircon crystals have obvious inherited cores and no inherited cores were found in the U-Pb analyses described by Valley et al. (2009; 2011).

The ore zircon chondrite normalized REE plots have low La relative to igneous zircon (Hoskin and Schaltegger, 2003) and to the LMG host rock zircon described above (Table 3-2, Fig. 3-2). Ore zircon REEs show an overall positive slope towards Lu with prominent positive Ce and weak negative Eu anomalies; however, samples 99-4A and 00-01 show extremely low La in some zircons.

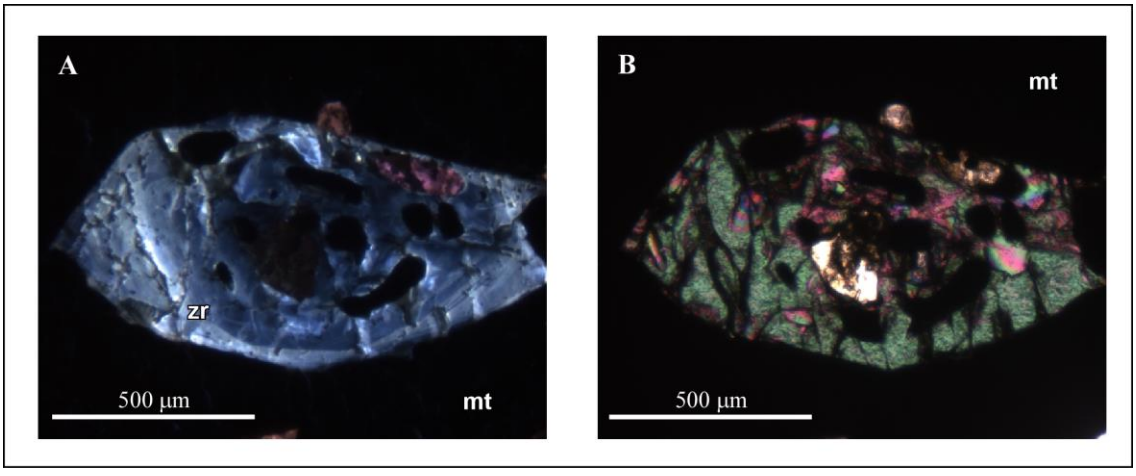

Figure 3-4: A) In situ zircon surrounded by magnetite from ore sample 00-01 in CL. B) Same as in A, in xpl.

Table 3-3. Representative LA-ICPMS minor- and trace-element analyses of LMG ore zircon

Sample	99-4A															
Grain	Gr. 1a	Gr. 1b	Gr. 1c	Gr. 4a	Gr. 4b	Gr. 4c	Gr. 5a	Gr. 5c	Gr. 2a	Gr. 2b	Gr. 1b	Gr. 1a	Gr. 3a	Gr. 3b	Gr. 3c	Gr. 4a
ppm																
Fe	31.1	23.3	-	31.1	85.5	62.2	-	-	-	-	-	15.5	77.7	23.3	-	5993
Mn	-	-	-	-	-	-	-	-	-	-	-	-	-	-	-	-
Sc	1336	1364	1252	1420	1283	1351	1336	1320	1325	1205	1176	1173	1089	1230	1125	1251
V	0.00	0.10	0.15	0.19	0.63	0.52	0.40	0.43	0.18	0.22	0.27	0.24	-	-	-	0.49
Co	-	-	-	-	-	-	-	-	-	16.7	-	-	-	-	15.2	-
Ni	-	-	-	-	-	-	-	-	-	-	-	-	-	-	-	-
Sr	1.01	0.96	0.42	0.60	1.04	0.59	0.88	0.67	0.61	0.71	0.49	0.51	0.56	0.65	0.15	0.35
Y	1529	1331	402	462	1494	737	1618	1075	716	911	673	747	886	1077	340	392
Nb	48.0	15.1	16.2	4.35	3.05	5.98	9.54	14.4	15.9	14.0	13.9	19.0	25.1	29.2	12.0	30.6
Ba	-	-	-	0.63	3.75	0.25	-	-	-	-	-	-	0.16	-	-	0.19
La	0.04	-	-	0.10	0.31	0.09	-	-	-	-	-	-	0.28	-	-	1.13
Ce	146	82.5	71.5	20.0	8.77	28.2	122.0	91.0	60.4	64.4	67.0	72.3	82.1	104	42.9	55.5
Pr	0.09	0.07	0.02	0.06	0.23	0.07	0.07	0.03	0.01	0.02	0.02	0.02	0.12	0.05	-	0.31
Nd	1.32	1.16	0.25	0.68	2.53	0.59	1.25	0.49	0.28	0.32	0.40	0.34	0.99	0.80	0.13	1.50
Sm	3.01	2.73	0.54	1.19	5.22	1.67	3.38	1.67	0.74	0.96	1.05	0.95	1.68	2.14	0.49	0.73
Eu	0.82	0.82	0.19	0.33	1.09	0.65	0.99	0.49	0.26	0.32	0.31	0.30	0.52	0.62	0.16	0.20
Gd	19.5	17.6	4.29	7.15	32.1	11.2	22.9	13.6	7.01	10.02	7.33	7.92	11.6	13.9	3.37	4.14
Tb	8.22	7.05	1.84	2.64	11.2	4.66	9.05	5.53	3.20	4.24	3.15	3.46	4.64	5.86	1.63	1.82
Dy	127	109	30.7	36.7	149	62.8	135.6	88.7	53.2	68.1	49.9	54.5	73.6	87.9	25.6	28.8
Ho	54.5	47.8	13.7	15.0	51.2	22.7	56.2	37.6	24.7	31.0	22.4	24.9	31.6	38.1	11.9	13.2
Er	298	266	78.1	79.6	225	111	305	206	142	176	126	142	175	209	68.7	76.6
Tm	77.0	70.2	21.1	21.8	48.0	29.7	77.8	52.8	37.6	44.7	32.5	36.3	44.5	53.6	18.4	20.3
Yb	815	770	236	248	431	339	829	567	420	487	357	401	481	580	207	233
Lu	157	145	48	53	72	67	165	111	89	105	78	92	102	119	46	51
Hf	6634	3941	6465	3567	7881	1619	9998	6011	5149	9073	4507	4247	9189	5289	9917	5565
Ta	11.02	5.29	5.10	1.56	1.07	1.74	3.80	5.05	5.35	4.35	3.96	5.28	6.65	7.65	4.00	5.62
Pb	55.0	25.5	8.51	14.3	6.02	21.4	34.3	15.3	14.1	16.2	9.27	15.1	30.0	36.7	7.96	6.15
Th	526	252	84	161	140	244	308	149	141	156	92	154	273	337	71	57
U	665	327	211	685	151	1009	344	298	390	402	244	432	365	445	133	218
Th/U	0.791	0.771	0.400	0.235	0.925	0.241	0.896	0.499	0.361	0.389	0.378	0.357	0.747	0.757	0.537	0.262

Note: A dash where a value is missing means that for that element the concentration is below the minimum detection limit.

Sample	99-4A								AH-06-6B							
Grain	Gr. 4b	Gr. 4c	Gr. 4d	Gr. 4c	Gr. 5a	Gr. 5c	Gr. 2a	Gr. 2b	Gr. 1	Gr. 7	Gr. 9	Gr. 12	Gr. 12	Gr. 18	Gr. 18	Gr. 20
ppm																
Fe	-	1275	-	-	46.6	-	-	62.2	-	-	-	-	-	-	-	-
Mn	-	15.5	-	-	-	-	-	-	-	-	-	-	-	-	-	-
Sc	1202	1250	1186	1204	1234	1198	1199	1179	1091	1208	1352	1305	1260	1334	1115	1425
V	0.13	-	-	0.44	0.49	0.74	0.22	2.31	-	-	-	-	-	-	-	-
Co	-	1.56	-	-	-	-	-	10.57	-	-	-	-	-	-	-	-
Ni	-	-	-	-	-	-	-	-	-	-	-	-	-	-	-	-
Sr	0.25	0.40	0.76	0.13	0.43	0.19	0.10	0.99	0.55	3.60	10.59	1.13	1.08	0.59	0.84	12.07
Y	344	294	1612	196	387	372	132	1343	702	1689	1791	667	988	1357	707	2713
Nb	12.2	9.82	40.5	0.85	9.85	0.98	0.90	6.27	10.4	53.0	79.8	10.9	7.79	2.83	11.5	83.5
Ba	-	0.83	-	-	-	-	-	-	-	7.13	14.36	0.78	0.83	-	0.98	9.53
La	-	0.67	0.11	-	-	0.02	-	0.04	0.05	8.10	18.29	0.29	0.32	0.06	1.23	25.9
Ce	60.1	48.3	132	91.3	64.1	96.2	73.0	115	75.0	64.5	92.6	93.1	94.0	6.57	115	162
Pr	-	0.14	0.09	0.02	0.02	0.03	0.02	0.03	0.07	1.69	7.28	0.19	0.36	0.16	0.52	11.1
Nd	0.18	0.68	1.44	0.35	0.24	0.47	0.32	0.66	0.51	9.34	30.04	1.42	2.61	3.02	2.29	53.6
Sm	0.46	0.52	2.78	0.77	0.47	1.09	0.69	1.91	1.00	6.36	12.12	2.09	2.29	5.55	2.22	22.7
Eu	0.16	0.15	0.91	0.32	0.13	0.53	0.30	0.69	0.35	0.83	1.69	0.29	0.47	0.90	0.40	3.17
Gd	3.51	3.33	22.9	3.97	4.03	7.06	3.29	15.06	7.93	29.2	34.7	9.04	13.4	31.8	12.1	65.7
Tb	1.60	1.38	9.17	1.32	1.73	2.44	1.04	6.62	3.37	10.0	12.6	3.64	5.11	10.6	4.35	20.8
Dy	25.1	23.2	137	17.3	28.9	33.4	13.4	104	51.6	135	168	53.7	76.5	135	60.2	253
Ho	11.5	10.5	58.6	6.76	13.1	13.1	4.85	46.8	23.6	54.1	63.2	23.1	33.9	49.3	25.2	94.1
Er	66.0	61.2	315	34.0	79.6	67.7	24.7	275	140	281	307	132	200	217	140	469
Tm	17.8	16.8	80.3	8.17	22.7	15.9	6.08	74.4	37.4	66.8	71.3	34.2	52.1	44.9	35.8	108
Yb	201	191	838	86	268	165	65	834	433	672	659	386	593	395	399	1044
Lu	43	38	171	18	58	35	13	174	102	130	116	87	133	69	92	194
Hf	5725	966	9286	4996	398	5575	5244	2967	10122	9813	11878	10363	10229	8937	8776	9492
Ta	4.12	2.90	10.80	0.39	3.27	0.37	0.42	2.51	6.12	28.35	39.69	7.78	4.62	1.61	6.34	43.5
Pb	5.65	6.59	52.41	2.68	11.39	4.01	1.82	46.1	21.7	33.3	40.8	19.8	22.3	6.00	15.8	59.3
Th	53	66	484	26	117	39	17	468	211	302	332	169	216	50	146	740
U	134	122	549	66	226	78	28	450	1454	1958	1291	1027	1305	136	617	2399
Th/U	0.392	0.544	0.881	0.394	0.517	0.503	0.622	1.041	0.145	0.154	0.258	0.164	0.165	0.364	0.237	0.308

Sample	AH-06-6B	OBO												
Grain	Gr. 19	-	-	-	-	-	-	-	-	Gr. 1a	Gr. 1b	Gr. 1c	Gr. 3a	Gr. 3b
ppm														
Fe	-	-	1516	-	-	-	-	-	-	-	2138	746	2309	3304
Mn	-	-	7.75	-	-	-	-	-	-	7.75	318	77.5	147	54.2
Sc	1173	1270	1252	1296	1291	1255	1316	1271	1370	1405	1235	1431	1363	2185
V	-	-	-	-	-	-	-	-	-	-	-	-	-	0.87
Co	-	-	-	-	-	-	-	-	-	-	-	-	-	25.7
Ni	-	-	-	-	-	-	-	-	-	-	-	-	-	-
Sr	17.53	1.12	0.64	1.19	0.59	1.16	0.59	1.06	0.99	0.69	12.99	4.77	2.52	0.80
Y	2606	1184	454	1248	393	1274	442	1010	1038	1072	796	761	1420	666
Nb	104	25.7	37.9	43.5	25.5	40.2	25.1	38.2	42.6	88.4	148	151	188	90.6
Ba	23.2	-	-	-	-	-	-	-	-	-	1.02	-	-	-
La	13.5	-	0.11	0.13	-	-	-	-	-	-	0.13	0.49	2.09	0.54
Ce	157	35.9	24.8	40.2	22.8	50.2	24.0	41.9	45.7	48.0	38.5	37.2	62.9	36.3
Pr	9.28	0.01	0.05	0.07	-	0.02	0.01	0.02	-	0.04	0.21	0.31	1.07	0.24
Nd	43.6	0.33	0.32	0.55	-	0.37	-	0.28	0.24	0.55	1.01	1.59	4.57	1.59
Sm	20.9	0.99	0.49	0.99	0.31	1.18	-	0.81	0.86	1.24	0.85	0.75	3.89	1.11
Eu	5.96	0.22	0.12	0.30	0.12	0.31	0.09	0.24	0.27	0.34	0.32	1.33	0.87	0.28
Gd	63.1	7.67	3.53	9.11	2.46	9.68	2.99	7.33	7.68	8.86	5.78	5.29	18.08	5.79
Tb	21.3	3.71	1.53	4.06	1.26	4.31	1.46	3.49	3.62	3.93	2.66	2.40	6.28	2.21
Dy	265	65.7	26.2	71.7	22.6	74.7	25.0	59.1	62.9	68.7	47.6	41.8	95.9	37.9
Ho	93.5	34.0	12.7	36.4	11.3	36.4	12.9	29.9	30.5	32.3	23.5	21.8	42.3	18.6
Er	441	219	83.6	229	72.0	226	82.2	187	191	198	158	148	245	119
Tm	93.7	61.9	23.4	63.1	20.7	62.4	23.4	52.6	53.8	54.7	47.4	44.7	65.0	35.0
Yb	874	696	268	694	241	697	265	602	613	588	562	534	678	403
Lu	153	151	58	149	51	147	57	124	127	120	124	119	141	89
Hf	10430	11181	10481	11437	10065	10847	11174	10178	12567	14071	16321	16216	14605	10195
Ta	38.5	13.8	23.2	20.3	18.6	17.3	17.9	19.1	21.1	28.3	51.6	62.3	34.4	48.1
Pb	69.7	24.0	10.3	25.6	8.36	26.6	9.56	21.7	25.3	31.9	16.9	11.3	36.0	13.1
Th	823	255	102	267	90	271	96	227	233	293	186	118	330	133
U	2226	1753	950	1826	816	1758	845	1646	1763	1811	1067	1985	2186	1843
Th/U	0.370	0.146	0.108	0.146	0.111	0.154	0.113	0.138	0.132	0.162	0.174	0.059	0.151	0.072

Sample	OBO														
Grain	Gr. 3c	Gr. 3d	Gr. 2a	Gr. 2b	Gr. 2c	Gr. 2d	Gr.1a	Gr. 1b	Gr. 1c	Gr. 3a	Gr. 3b	Gr. 3c	Gr. 3d	Gr. 2a	Gr. 2b
ppm															
Fe	1617	38.9	-	2293	-	46.6	31.1	2705	77.7	700	202	1360	5931	31.1	3008
Mn	248	-	-	325	-	-	-	472	7.75	132	-	209	558	-	441
Sc	1327	1443	1407	1222	1342	1395	1457	1354	1426	1416	2129	1370	1960	1402	1345
V	-	-	-	-	-	-	-	-	-	-	-	-	0.46	-	-
Co	-	-	-	-	-	-	-	-	-	-	-	15.08	-	-	-
Ni	-	-	-	-	-	-	-	-	-	-	-	-	-	-	-
Sr	2.60	0.55	0.46	10.9	0.39	0.65	0.96	14.6	0.93	3.45	0.93	6.02	26.33	0.91	9.93
Y	1177	305	927	1341	420	458	1098	1007	522	1679	571	1077	1816	910	1580
Nb	145	97.8	94.8	111	196	95.5	50.0	92.7	101	79.6	58.4	77.9	164	47.6	85.2
Ba	-	-	-	-	-	-	-	1.10	-	0.42	-	0.70	3.73	-	0.68
La	1.25	-	-	2.13	-	-	-	0.17	-	1.59	-	1.21	3.84	-	4.25
Ce	52.0	13.5	40.1	54.6	22.5	18.9	50.6	47.5	30.6	66.4	34.2	50.5	90.1	42.3	64.3
Pr	0.76	-	-	0.47	-	-	0.03	0.25	0.01	0.74	-	0.69	2.69	0.02	1.06
Nd	4.51	0.06	0.22	2.00	-	0.12	0.45	1.54	0.11	4.38	0.12	4.02	14.1	0.29	5.16
Sm	3.95	0.10	0.54	1.83	0.25	0.23	1.21	1.16	0.34	3.60	0.34	2.94	7.09	0.84	3.57
Eu	0.83	0.05	0.20	0.49	0.05	0.09	0.28	0.42	0.09	0.82	0.10	0.64	1.76	0.25	0.79
Gd	12.5	1.40	7.35	11.51	2.20	2.00	9.34	7.16	2.97	18.22	3.47	11.87	23.17	7.39	15.58
Tb	4.76	0.78	3.09	4.65	1.01	1.13	4.20	3.34	1.52	7.07	1.77	4.25	7.77	3.29	6.16
Dy	68.6	14.4	55.3	80.8	21.0	22.7	68.9	57.6	28.4	110	32.5	66.4	114.9	55.6	98.2
Ho	32.7	8.01	27.0	41.3	11.3	12.1	32.5	29.1	14.9	50.1	16.7	31.1	52.0	27.5	46.8
Er	202	59.2	170	259	82.8	88.6	198.6	189.9	102.1	299.1	112.3	188.2	311.2	171.4	288.5
Tm	54.6	20.1	47.1	72.3	27.1	29.6	55.4	56.4	32.2	82.0	34.0	53.6	87.5	48.6	79.8
Yb	604	271	516	838	355	403	613	658	396	886	407	613	993	545	903
Lu	128	66	110	183	85	102	117	134	83	166	84	120	202	110	187
Hf	16197	1277	15341	17048	7542	2208	4700	6754	2519	6518	3039	7743	9673	3614	6867
Ta	37.0	61.6	28.9	30.6	92.5	55.5	30.2	54.3	83.9	28.7	45.1	40.0	78.6	29.6	34.1
Pb	30.8	4.91	27.4	19.8	8.30	9.31	29.3	18.0	9.57	34.6	12.0	23.1	23.6	23.3	19.0
Th	305	55	252	241	74	93	301	220	96	362	128	255	354	246	246
U	2336	943	1715	1369	1510	1253	1675	2729	1738	2095	1693	2258	4169	1600	2687
Th/U	0.131	0.058	0.147	0.176	0.049	0.075	0.180	0.081	0.055	0.173	0.076	0.113	0.085	0.154	0.091

Sample	OBO		00-01								
Grain	Gr. 2c	Gr. 2d	Gr. 1a	Gr. 1b	Gr. 2b	Gr. 2a	Gr. 4a	Gr. 4b	Gr. 5d	Gr. 5c	Gr. 5d
ppm											
Fe	31.1	1663	-	23.3	23.3	-	-	-	-	-	-
Mn	-	23.2	-	-	-	-	-	-	-	-	-
Sc	1428	1428	1079	1230	1189	1335	1202	1358	1210	1101	1380
V	-	0.26	-	-	0.20	0.12	-	-	-	-	-
Co	-	0.30	-	-	-	13.9	-	-	-	-	-
Ni	-	-	-	-	-	-	-	-	-	-	-
Sr	0.96	1.11	0.36	0.71	0.82	0.48	-	-	-	-	-
Y	435	423	392	1236	1832	860	397	833	1497	437	442
Nb	96.2	55.0	12.8	27.9	26.7	32.0	13.6	21.9	24.7	15.5	9.27
Ba	-	-	-	-	-	-	-	-	-	-	-
La	-	0.15	0.06	-	-	-	-	-	-	-	-
Ce	21.4	19.5	57.2	149	175	144	59.1	124	209	85.3	88.1
Pr	-	0.07	0.03	0.04	0.07	0.03	-	0.05	-	0.03	-
Nd	-	0.36	0.30	0.65	1.24	0.54	-	0.72	1.51	0.24	-
Sm	0.18	0.33	0.55	1.49	2.80	1.46	0.44	1.72	3.90	0.48	0.48
Eu	0.05	0.08	0.15	0.49	0.85	0.36	0.14	0.41	0.97	0.15	0.16
Gd	2.11	2.01	3.91	13.3	21.6	9.33	3.63	9.96	19.2	4.13	4.28
Tb	1.08	0.89	1.72	5.73	8.94	3.87	1.48	4.07	7.50	1.82	1.96
Dy	20.3	17.1	27.7	89.7	135	60.0	26.9	60.4	107.5	29.6	28.3
Ho	11.2	9.15	12.2	38.9	56.6	26.3	11.9	25.3	45.7	13.1	13.5
Er	81.1	67.3	68.7	214	306	148	70.2	143	249	76.2	76.6
Tm	27.3	23.3	18.0	54.5	72.0	37.1	17.8	35.7	62.6	19.7	19.0
Yb	362	335	187	553	708	380	182	357	615	204	194
Lu	83	84	34	94	132	73	35	66	115	38	40
Hf	1418	1447	2814	4409	7139	5562	13248	10753	9059	10153	13643
Ta	114	34.0	6.82	8.26	7.74	10.3	9.01	7.48	7.10	5.53	5.32
Pb	7.09	10.0	2.18	6.98	10.9	5.59	2.10	5.55	11.3	3.30	2.82
Th	76	88	22	69	110	57	21	45	111	29	29
U	1524	1255	119	216	273	217	134	170	264	145	136
Th/U	0.050	0.070	0.181	0.321	0.402	0.264	0.159	0.264	0.421	0.204	0.216

3.3 Apatite EPMA and LA-ICPMS Major-, Minor-, and Trace-Element Analyses

Apatites from the LMG consist mainly of end-member fluorapatite with significant concentrations of REE and silica (Table 3-4). Apatite in the ore samples occurs as discrete void-filling grains or replacing other minerals (e.g. 99-4A and AH-06-6B; Figs 1-5a to d) and also occurs as large crystals sometimes forming clusters as found in ore samples 06-4B and OBO (Fig. 1-5e-f, Table B-1 and B-2). In the host rock samples, apatite occurs as subhedral to anhedral crystals, 300-600 um in length, usually located at grain boundaries of the major rock forming minerals (Fig. 1-3).

The apatite grains overall show little internal zoning in either BSE or CL, and rarely contain any visible inclusions (Fig. 1-4b-l; see also Fig. A-1). The apatite samples have been classified based on the type of alteration present in the host rock sample from which the apatite was separated as follows: least altered 99-1A and fayalite granite 99-3A; Na-altered 99-2B and 99-5A; K-altered 99-6B and 99-6C; and ore samples AH-06-6B, 06-4B, OBO, 00-01 and 99-4A. This classification based on alteration is the same as used to differentiate the whole-rock geochemistry of samples shown in Figure 3-1b.

Apatites from the LMG host and ore samples exhibit a wide range of colors in CL (Fig.1-4b-l), that vary systematically between samples, and in some cases within a single sample (e.g., 99-6C). As mentioned earlier the variety of CL colors in apatite indicates the REE CL activation is overwhelming the more commonly observed Mn^{2+} CL activation (Roeder et al., 1987). Apatite from ore samples 00-01 and 99-4A appears to have some alteration along fractures within the grains (Fig. 1-4c and e). Host rock apatite samples

99-1A and 99-5A also have some alteration along the grain margins and fractures, which appears as brighter CL emission along the edges. Apatite from samples 99-5A and 99-6C shows more within-sample variation in CL emission than any of the other samples investigated, perhaps suggesting different apatite crystallization or alteration events. Major-, minor- and trace-element data for LMG host and ore apatite samples are reported in Table 3-4, Table B-1 and B-2.

Table 3-4. Representative apatite LA-ICPMS major-, minor- and trace-element analyses from the LMG

Samples	99-1A			99-2B			99-3A			99-4A			99-5A
Alteration	Least altered			Na-altered			Fayalite granite			Ore			Na
Grain	gr 10	gr 14	gr 17	gr 14	gr 6	gr 9	gr 4	gr 2	gr 5	gr. 9	gr. 11	gr. 13	gr. 41
wt. %													
SiO2	3.32	3.66	3.01	2.86	3.29	2.91	10.8	10.9	10.0	0.75	0.81	0.81	2.19
FeO	0.01	0.07	0.11	0.12	0.04	0.03	0.65	0.60	0.55	0.01	0.01	0.01	0.02
MnO	0.04	0.03	0.03	0.01	0.01	0.01	0.18	0.17	0.17	0.02	0.03	0.03	-
MgO	0.01	0.01	0.02	0.01	0.04	0.01	0.01	0.01	0.01	0.01	0.01	0.01	0.02
CaO	48.3	48.4	48.3	48.7	48.7	48.8	33.5	34.4	33.8	53.2	53.3	53.6	50.1
P2O5	32.4	32.9	34.0	34.3	33.5	34.1	20.4	21.2	20.7	38.7	39.0	39.5	33.5
ppm													
Sc	0.49	1.03	0.33	0.27	0.26	0.28	0.51	0.45	0.62	0.44	0.48	0.58	1.23
Mn	431	435	437	434	432	-	432	432	-	-	432	-	188
As	194	200	186	693	703	632	867	816	769	1037	1151	1213	233
Sr	167	148	166	93	102	99	146	164	147	192	185	195	223
Y	23490	26826	24638	1821	2119	1074	46878	50058	43055	2409	2961	2851	8290
Zr	3.63	5.60	2.57	3.15	3.90	3.37	23.83	20.55	16.76	0.31	0.36	0.31	0.86
Nb	0.91	0.89	0.80	0.23	0.23	0.18	0.34	0.20	0.68	0.50	0.60	0.53	0.10
Sn	1.00	0.87	1.03	1.46	1.21	1.17	1.77	1.65	1.93	1.06	1.13	-	0.17
Ba	0.22	0.63	0.26	0.67	2.83	0.49	2.37	1.27	5.21	0.59	0.29	0.68	-
La	2949	3654	4623	18172	20495	18824	29692	28248	29088	3471	3472	3322	3296
Ce	11814	13039	13576	28275	31939	28291	79122	75034	75456	7463	7786	7452	10545
Pr	2109	2215	2154	2658	2976	2580	11076	10549	10425	836	902	876	1493
Nd	11813	12146	11351	9179	10132	8567	52264	50395	49071	3377	3771	3623	7456
Sm	3519	3747	3356	1187	1261	985	11837	11528	10880	564	700	677	1517
Eu	251	305	306	141	150	117	792	785	721	59	75	73	171
Gd	4002	4340	3925	755	820	537	11021	10882	10152	523	655	644	1525
Tb	708	784	705	84.8	94.8	54.4	1815	1775	1629	74	97	95	218
Dy	4433	4965	4494	389	439	232	10768	10689	9583	430	567	548	1228
Ho	932	1050	958	63.4	73.0	35.5	2137	2132	1880	91.6	117	113	270
Er	2462	2805	2567	133	154	73	5258	5292	4552	243	301	290	741
Tm	327	376	341	14.5	17.7	8.4	658	657	552	32.3	38.6	36.3	94.5
Yb	2006	2310	2096	86.2	109	53.3	3638	3609	3033	212	238	224	611
Lu	238	273	250	11.5	14.6	7.7	354	352	302	32	34	32	93
Hf	0.19	0.22	0.21	0.08	0.15	0.04	1.23	1.14	0.98	-	0.05	0.04	0.15
Ta	-	-	-	-	-	-	-	-	-	-	-	-	0.02
Th	332	411	110	1602	3154	2431	996	1013	1058	253	290	260	438
U	79.1	96.8	79.6	311	489	432	288	294	309	16.5	17.6	18.0	97.7

Note: A dash where a value is missing means that for that element the concentration is below the minimum detection limit.

Samples	99-5A		06-4B			99-6B			99-6C			OBO		
Alteration	Na-altered		Ore			K-altered			K-altered			Ore		
Grain	gr. 23	gr. 13	gr. 12	gr. 10	gr. 22	gr. 15	gr. 17	gr. 22	gr. 6	gr. 9	gr. 17	gr. 2	gr. 3	gr. 4
wt. %														
SiO2	1.36	1.59	1.15	1.09	1.01	0.25	0.41	0.10	0.51	0.50	0.40	2.73	2.90	2.69
FeO	0.02	0.04	0.02	0.01	0.02	0.02	0.03	0.07	0.02	0.04	0.03	0.04	0.05	0.04
MnO	-	-	-	-	-	0.04	0.05	0.05	0.04	0.04	0.03	0.03	0.03	0.03
MgO	0.02	0.02	106	104	112	0.01	0.01	0.03	0.01	0.01	0.01	0.01	0.01	0.02
CaO	52.5	50.8	52.8	52.6	53.0	54.0	54.9	54.8	54.2	54.5	54.7	49.4	49.1	49.3
P2O5	34.9	33.4	35.1	35.5	34.4	41.0	41.5	42.1	38.0	38.3	38.9	33.5	33.6	34.2
ppm														
Sc	0.62	0.27	0.15	0.13	0.15	1.41	1.89	0.24	2.34	2.31	2.36	0.14	0.16	0.14
Mn	168	111	119	81.3	148	434	434	429	430	-	431	436	433	430
As	176	201	1441	1589	1631	104	131	132	76.3	74.1	108	2792	2822	2823
Sr	239	173	155	162	166	169	200	215	133	95	75	290	288	291
Y	4720	3911	2542	2409	2305	572	1234	1436	1111	841	743	12300	12870	11814
Zr	1.66	0.81	0.52	-	0.46	0.19	0.67	0.11	0.74	0.29	1.79	4.67	11.05	3.20
Nb	0.03	0.04	0.11	0.16	0.17	-	-	0.00	0.04	0.02	0.03	0.11	0.12	0.11
Sn	0.10	-	0.21	0.21	0.23	0.88	0.86	0.85	0.90	0.75	0.72	0.76	0.73	0.72
Ba	0.14	0.24	0.15	0.18	0.15	0.39	3.81	0.71	0.43	-	1.25	0.46	0.55	0.39
La	1175	6700	2301	2207	2065	754	642	296	3346	3327	1978	10143	10886	9356
Ce	3929	12163	5055	4858	4622	1635	1932	791	4221	4217	2970	21103	22476	20114
Pr	612	1220	595	563	541	175	258	116	361	346	281	2435	2593	2338
Nd	3298	4633	2553	2407	2273	701	1169	578	1307	1172	1050	10345	10973	9915
Sm	741	723	483	446	418	110	223	148	189	153	158	2011	2140	1953
Eu	106	123	59.9	55.5	51.1	34.7	49.6	41.2	44.0	29.7	26.2	195	206	190
Gd	816	704	458	432	413	101	213	166	190	141	147	2048	2149	1961
Tb	115	96.7	68.8	64.4	61.7	13.2	28.7	26.3	25.9	19.4	19.0	326	343	312
Dy	662	556	401	375	358	71.8	163	162	151	112	104	2012	2115	1928
Ho	145	123	84.3	80.1	76.1	15.5	35.3	36.8	34.1	25.3	22.1	441	468	424
Er	400	352	233	222	207	42.8	99.2	107	97.0	72.6	62.1	1230	1312	1187
Tm	50.0	47.1	31.8	29.9	28.1	5.9	13.7	15.0	13.1	10.2	8.4	168	179	162
Yb	321	337	213	199	191	44.7	102	110	92.0	76.1	60.1	1055	1118	1019
Lu	50.3	55.3	29.9	27.6	27.3	8.1	18.0	19.4	15.9	13.7	11.2	130	138	125
Hf	0.07	0.06	0.16	0.05	0.03	0.02	0.03	-	-	-	0.03	0.16	0.14	0.48
Ta	0.01	0.01	0.01	0.01	0.01	-	-	-	-	-	-	-	-	-
Th	272	459	235	176	252	76.6	71.1	1.81	268	139	259	1571	1743	1303
U	22.8	43.9	62.6	50.5	46.3	18.8	57.0	3.3	31.2	21.4	25.9	247	274	227

Samples	00-01			AH-06-6B		
Alteration	Ore			Ore		
Grain	gr. 19	gr. 25	gr. 27	gr. 44	gr. 32	gr. 19
wt. %						
SiO2	4.21	4.93	4.73	3.17	3.78	5.70
FeO	0.16	0.12	0.15	0.02	0.04	0.07
MnO	0.06	0.06	0.06	-	-	-
MgO	0.03	0.02	0.02	0.02	0.02	0.02
CaO	46.0	45.4	44.8	50.4	49.5	45.6
P2O5	30.5	30.0	29.7	32.9	32.9	28.7
ppm						
Sc	0.36	0.38	0.39	0.28	0.30	0.47
Mn	431	436	-	123	84	211
As	1250	1205	1262	852	850	1074
Sr	197	187	187	118	114	113
Y	30346	31911	31281	16727	20378	27733
Zr	3.00	3.56	5.58	3.92	3.05	8.09
Nb	1.71	2.22	2.13	2.14	2.34	1.89
Sn	0.98	1.05	0.92	0.22	0.28	0.32
Ba	0.20	0.21	-	0.07	0.14	0.10
La	4056	4083	4212	390	351	1755
Ce	21002	22954	23899	4968	4362	17512
Pr	3810	4239	4450	1522	1346	4263
Nd	20582	22953	23896	11048	10140	25753
Sm	5443	5958	6061	3468	3715	6530
Eu	606	666	670	341	393	615
Gd	5492	6061	6118	3586	4019	6190
Tb	881	979	971	565	661	979
Dy	5332	5956	5820	3371	4062	5757
Ho	1104	1251	1220	703	849	1224
Er	2893	3293	3235	1944	2365	3401
Tm	375	430	425	271	336	489
Yb	2247	2602	2569	1885	2318	3396
Lu	262	307	302	264	326	474
Hf	0.30	0.32	0.38	0.46	0.55	0.82
Ta	-	-	-	0.12	0.13	0.17
Th	545	673	741	1082	1381	3901
U	164	260	223	326	415	1100

Sr versus As (Fig. 3-5a), shows distinct groupings of samples based on their rock types or alteration. The ore apatite is generally enriched in As compared to the host apatite. Host samples 99-2B and 99-3A are both more enriched in As compared to 99-1A, 99-5A, 99-6B and 99-6C, but contain less As compared to the ore apatite. All of the ore apatite, as well as host apatite samples 99-1A, 99-2B and 99-3A, have fairly consistent Sr concentrations, whereas apatite from host samples 99-5A, 99-6B and 99-6C show a large spread in Sr concentrations within the each sample. Apatite from ore sample OBO and some outliers from host sample 99-5A show the highest As concentrations among all

samples, although these As-enriched apatite show generally similar concentrations of Sr as the other samples.

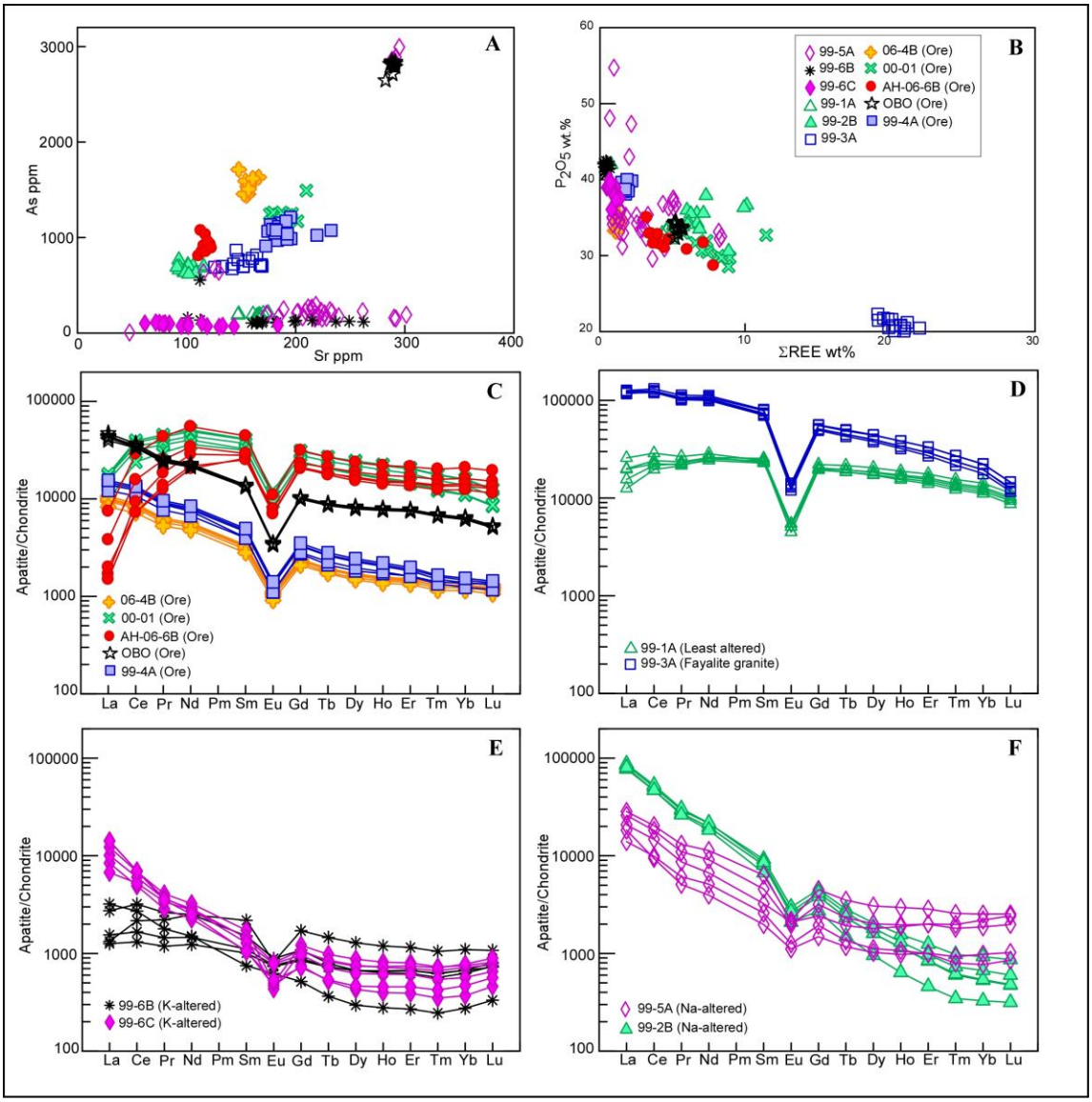

Figure 3-5: A) Plot of Sr (ppm) vs. As (ppm) of the LMG host rock and ore apatite. OBO and 99-6B have the highest As of the apatite samples. Sr (ppm) vs. As (ppm) defines well the different apatite based on samples (ore vs. host) and alteration type (unaltered vs. Na-altered vs. K-altered. B) ΣREE (wt.%) vs. P_2O_5 (wt.%) in LMG host rock and ore apatite. 99-3A, open blue squares has the highest REE of all the host and ore apatite samples and lowest P_2O_5. C) Anders and Grevesse

(1989) chondrite normalized REE plot of representative apatite from ore samples AH-06-6B, 06-4B, OBO, 00-01 and 99-4A. D) Chondrite normalized REE plot of representative least altered apatite sample 99-1A and fayalite granite 99-3A. E) Chondrite normalized REE plot of representative apatite from K-altered samples 99-6B and 99-6C. F) Chondrite normalized REE plot of representative apatite from Na-altered sample 99-2B and variably Na altered 99-5A.

3.3.1 Host-rock apatite

The EPMA data for the LMG host rock apatite show a wide compositional range in CaO (32.8 to 55.4 wt.%) and P_2O_5 (21.0 to 41.5 wt.%; Fig. 3-5b, Table 3-4, Table B-1 and B-2). In comparison, stoichiometric apatite contains approximately 55 wt. % CaO and approximately 42 wt. % P_2O_5 (e.g., Ca = 39.7 wt. % El.; P = 18.4 wt. % El.; F = 3.8 wt. % El.). Apatite from sample 99-3A has the highest REE concentrations ever reported (to our knowledge) for apatite with up to 22 wt.% total REE and 5 wt.% Y. F shows a wide range in concentrations in the LMG host rock apatites, from 2.9-4.6 wt.% (Table B-2).

Major- and minor-element data for apatite, correlate with host rock alteration type. The K-altered samples have generally higher P_2O_5, CaO, F, and lower SiO_2 contents compared to the least altered, and Na-altered samples (Fig. 3-5a, Table 3-4, Table B-1 and B-2). Sample 99-5A, which experienced both K- and Na-metasomatism, exhibits significant intra-sample variability in major-elements in apatite. It is possible that the apatite with higher P_2O_5, CaO and F and lower SiO_2 in this sample reflect predominately K-metasomatic alteration, whereas apatite with higher SiO_2 and lower P_2O_5, CaO and F represents less altered (or Na-altered) apatite. The highest REE enriched apatite (99-3A) has lower CaO, P_2O_5, and F and higher SiO_2 compared to all the other samples.

Arsenic occurs above detection limits for the EPMA under the conditions used, and was measured by both EPMA and LA-ICPMS in all the LMG apatite samples (Fig. 3-5a; Table 3-4, Table B-1 and B-2). Arsenic in the host rock apatite ranges from 100-2990 ppm. Strontium spans a lower range in concentration between samples, from 60-300 ppm, the lower end of which is atypical for igneous apatite (Dempster et al., 2003).

The REE (and Y) concentrations in the host rock apatite can be quite variable, ranging from 0.26 to 22 wt.% total REE, and 0.04 to 5 wt.% Y (Fig. 3-5b; Table 3-4, Table B-1). The chondrite normalized REE patterns for apatite from samples 99-1A (least altered) show a weak negative to flat slope with a negative Eu anomaly (Fig. 3-5d). Sample 99-3A (fayalite granite, Fig. 3-5d) has a weak negative slope with a negative Eu anomaly; however, the apatite in this sample has about an order of magnitude greater REE concentration compared to 99-1A, and higher REE concentration than all of the other apatite samples.

Apatite from samples 99-2B and 99-5A (Na-metasomatised samples) have an overall negative slope in REE that flattens between Tm and Lu, and a moderate negative Eu anomaly. The REE concentrations in apatite from 99-5A are more heterogeneous than those from 99-2B (Fig. 3-5f). Apatite from samples 99-6B and 99-6C (K-metasomatised samples) have similar REE patterns from Gd through Lu (slightly convex-up, with a moderate negative Eu anomaly; Fig. 3-5e); however, 99-6C (Fig. 3-5e) has a negative slope from La-Sm, with greater concentrations of LREE compared to 99-6B.

3.3.2 Ore Apatite

The P_2O_5 and CaO concentrations in the apatite from ore samples range from 31.2-40.4 wt.% P_2O_5 and 44.8-54.5 wt.% CaO (Fig.3-5b; Table 3-4, Table B-1 and B-2). Many of the analyses are distinctly non-stoichiometric. SiO_2 concentrations are correlated with REE concentrations, and inversely correlated with concentrations of P_2O_5 and CaO.

Arsenic in the ore apatite samples ranges from 808 to 2844 ppm with AH-06-6B and 99-4A containing the lowest concentrations and 06-4B and OBO containing the highest. Strontium on the other hand ranges from 111 to 291 ppm, with AH-06-6B and 06-4B containing the lowest and 00-01 and OBO containing the highest concentrations (Fig. 3-5a; Table 3-4, Table B-1 and B-2).

The ore apatite ranges from 1 to 11 wt.% REE, and 0.2 to 4 wt.% Y with apatite in ore sample 00-01 containing the highest total REE and Y concentrations of the ores (although less than apatite from host-rock sample 99-3A), ranging from 6-11 wt.% REE and 2-4 wt.% Y (Fig. 3-5b, Table 3-4, Table B-1). The apatite from the ore samples exhibit two types of chondrite normalized REE patterns (Fig. 3-5c). The first type is observed in samples 99-4A, 06-4B and OBO, which have an overall negatively sloped REE pattern, a prominent negative Eu anomaly, and a weakly convex-up curvature that becomes flat between Tm to Lu (Fig. 3-5c). Among these three samples, apatites from sample OBO shows about an order of magnitude greater REE concentrations than the other two samples (99-4A and 06-4B). The second type, comprising apatites from AH-06-

6B and 00-01, is characterized by a positive slope in the LREE pattern, a negative Eu anomaly, and slightly negative sloped (00-01) to flat (AH-06-6B) HREE pattern.

3.4 Titanite EPMA and LA-ICPMS Trace-Element Analyses

Only three samples from the LMG host rocks contain titanite: 99-2B (Na-altered), 99-5A (multiple generations of Na alteration), and 99-6C (K-altered). The titanite from these samples are mostly unzoned in BSE, anhedral to subhedral, 200-250 μm in length, and inclusion free (Fig. 3-6a-c, see also Fig. A-1b). When picking the titanite crystals for this study, it was observed that the titanite grains had unusual appearance, unlike typical bronze-colored wedge-shaped titanite crystals. Nearly all titanite grains in the three titanite-bearing samples (99-2B, 99-5A, and 99-6C) were, rounded, clear, and commonly contained thin plates inferred to be hematite. In fact, it was difficult to distinguish titanite from apatite in these samples without further verification using EDS or CL. When present in thin section, the titanite occurs primarily at grain boundaries near clinopyroxene or in association with magnetite. Major-, minor- and trace-element data for LMG host rock titanite samples are reported in Tables 3-5, B-3 and B-4. None of the ore samples contain titanite.

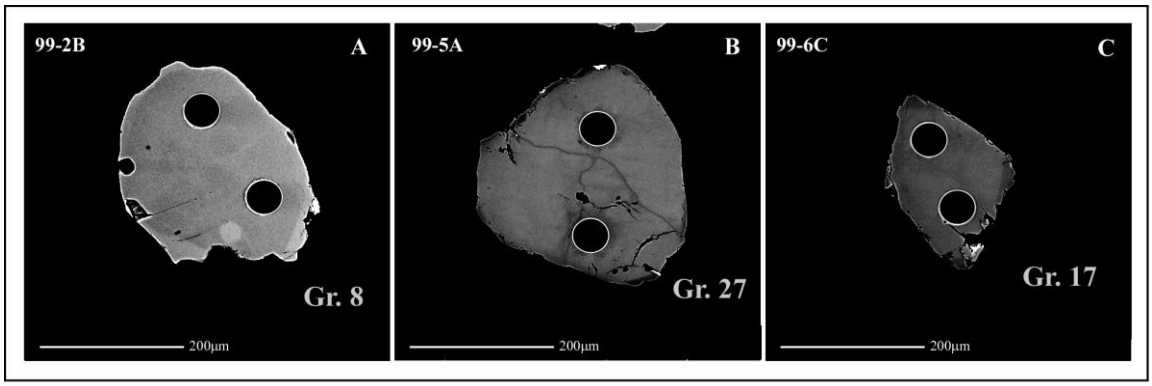

Figure 3-6: Back-scattered electron images of representative titanite from the LMG with LA-ICPMS ablation sites. A) Sample 99-2B. B) Sample 99-5A. C) Sample 99-6C.

Table 3-5. Representative titanite LA-ICPMS major-, minor- and trace-element analyses

Sample	99-5A		99-2B		99-6C	
Grain	Gr. 27.1	Gr. 27.2	Gr. 8.1	Gr. 8.2	Gr.17.1	Gr. 17.2
wt. %						
SiO2	31.9	33.9	33.1	33.0	33.6	33.0
TiO2	29.3	29.1	30.2	30.2	30.8	30.7
FeO	5.78	5.78	5.45	5.41	3.72	3.41
MgO	0.28	0.27	0.11	0.11	0.24	0.21
CaO	25.4	25.7	26.9	26.9	26.9	26.6
P2O5	0.04	0.06	0.01	0.02	0.06	0.06
ppm						
Sc	45.5	80.0	10.6	11.0	91.7	91.5
V	103	104	20.0	21.6	75.5	75.5
Mn	224	223	170	171	322	287
Cu	2.37	3.57	2.75	2.81	56.2	17.4
Zn	5.02	5.46	7.48	7.68	20.4	6.81
As	112	116	120	122	108	99.7
Sr	10.3	10.7	10.0	9.94	16.6	11.8
Y	11030	11149	2332	2292	6109	5843
Zr	1091	758	2389	2586	763	710
Nb	4929	5065	2975	2968	2267	2163
Sn	974	967	417	419	731	755
La	2477	2472	3189	3307	2974	2753
Ce	9381	9598	8064	8478	8509	7976
Pr	1531	1574	1052	1102	1160	1090
Nd	7675	7957	4446	4631	5007	4828
Sm	2038	2121	857	913	1134	1056
Eu	297	302	133	140	186	171
Gd	1992	2051	639	664	1078	1015
Tb	353.9	365.9	93.6	96.3	192	180
Dy	2239	2250	488	510	1176	1124
Ho	459	468	85.5	86.7	247	233
Er	1249	1261	202	201	680	663
Tm	178	176	25.4	25.5	102	101
Yb	1177	1197	151	151	725	705
Lu	139	142	16.1	16.2	90.4	88.9
Hf	57.0	390	110	121	46.2	45.1
Ta	287	290	161	158	141	119
Th	858	852	411	432	1009	1069
U	219	262	273	277	308	307

Titanite from sample 99-5A has the lowest and most variable CaO concentrations. Sample 99-6C has the highest TiO_2 of all the titanites analyzed, and sample 99-5A has the most variable TiO_2 concentrations, ranging from 31.2-34.4 wt.%. The SiO_2 content of titanite is similar in all three samples, ranging from 29.3-30.3 wt.%. Sample 99-6C has the highest concentration of Al_2O_3, ranging from 2.9-3.8 wt.%.

FeO contents of titanite decrease in the following order: Titanite from sample 99-2B contains 4.7-5.2 wt.%, 99-5A with 3.1-4.7 wt.%, and 99-6C contains 2.5-3.4 wt.% (Fig. 3-7a, Table B-3). Fluorine contents of titanite are 1.5-1.7 wt.% in samples 99-2B and 1.3-1.7 wt.% for 99-6C, and 1.2-1.6 wt.% in sample 99-5A (Fig. 3-7b, Table B-3).

Titanite with lower TiO_2, such as those from sample 99-2B, tend to have higher FeO and lower Al_2O_3 contents (compared to titanite from the other samples). Similar to the observations from apatite, titanite from sample 99-5A show the most intra-sample variation of each element concentration. Titanite from 99-5A also have the highest Na_2O concentrations among the three samples, ranging from 0.04-0.16 wt.% Na_2O, despite the fact that sample 99-2B is more strongly albitized than 99-5A (curiously, the Na_2O content of titanite from 99-2B is very low, as is that from K-altered sample 99-6C). Zirconium concentrations are highest in titanite from sample 99-2B, ranging from 1394 to 3376 ppm whereas Zr in titanite from 99-5A is highly variable ranging from 48-1353 ppm. Niobium is also highly variable in titanite from 99-5A, ranging from 1347-5487 ppm (which includes the highest measured Nb concentrations among the three samples).

The titanite samples tend to have high REE (e.g., Tiepolo et al., 2002) compared to the igneous titanite from sample BG (metaluminous Old Woman granodiorite, Mojave Desert, collected by Calvin Miller) and Y-13 (granodiorite from the Half Dome Porphyry in Yosemite National Park collected by Philip Piccoli), which are shown for comparison in Figure 3-7a. Yttrium concentrations in titanite range from ~0.2 wt.% Y in sample 99-2B, up to 1.4 wt.% Y in sample 99-5A (Fig. 3-7a, Tables 3-5 and B-4).

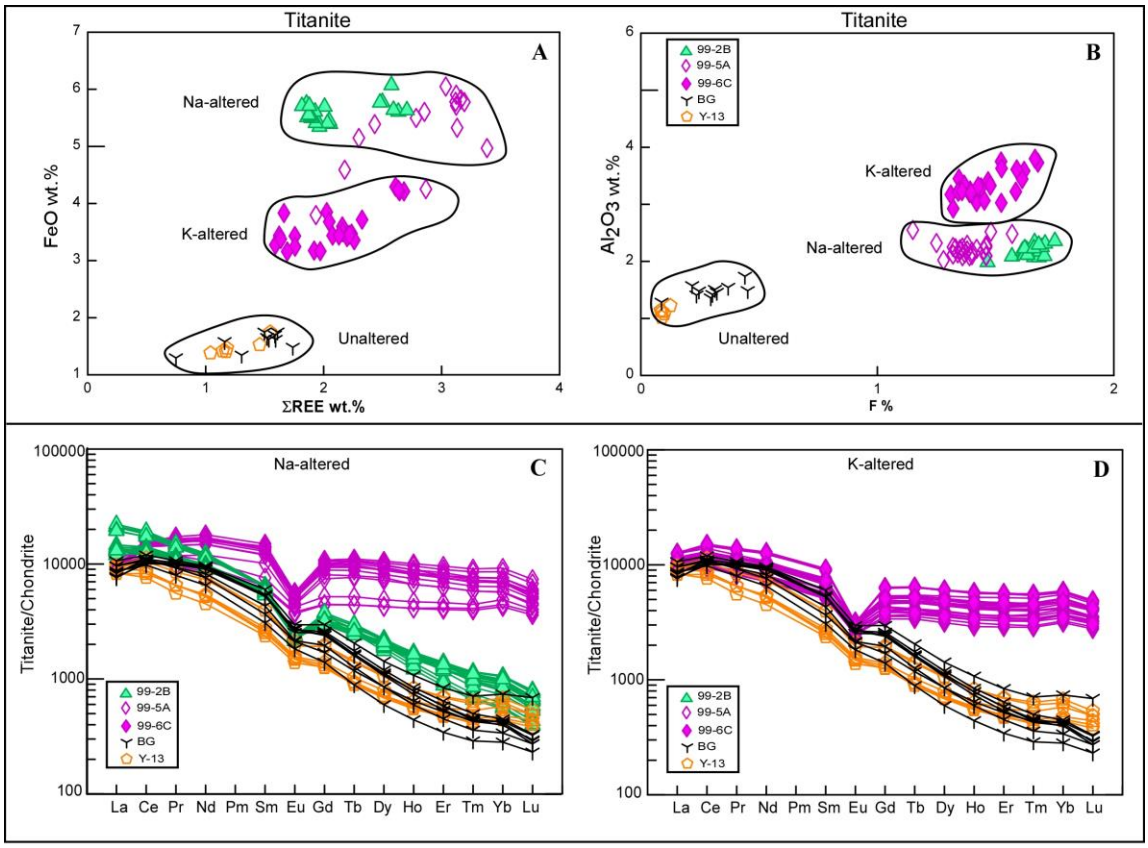

Figure 3-7: A) ΣREE (wt.%) vs. FeO (wt.%) from LMG titanite with comparison igneous titanite samples Y-13 and BG. LMG titanite are more enriched in REE and FeO compared to igneous titanite samples. B) F (wt.%) vs. Al_2O_3 (wt.%) demonstrates the F enrichment in the LMG titanite pointing towards a fluorotitanite composition. Al_2O_3 is higher in the LMG samples compared to igneous titanite Y-13 and BG. C) Anders and Grevesse (1989) chondrite normalized REE plot of representative titanite from Na-altered samples 99-5A and 99-2B with igneous titanite samples Y-13 and BG plotted for comparison. D) Anders and Grevesse (1989) chondrite normalized REE

plot of representative titanite from K-altered sample 99-6C with igneous titanite samples Y-13 and BG plotted for comparison.

Titanite from the Na-altered samples (99-2B and 99-5A) exhibit two different REE patterns (Fig.3-7c). Sample 99-5A has a weakly convex up chondrite-normalized LREE pattern and a fairly flat HREE pattern with a well-defined negative Eu anomaly. Sample 99-2B has an overall negative slope REE pattern with significantly less HREE than 99-5A, and a moderate negative Eu anomaly. Figure 3-7d shows the chondrite-normalized REE pattern for titanite from K-altered sample 99-6C, which is similar in magnitude and shape to that of titanite from 99-5A (Fig. 3-7c). It is interesting to note that sample 99-5A appears to have undergone multiple episodes of alteration, likely multiple events of Na-metasomatism and possibly weak K-metasomatism. The similarities in REE pattern between samples 99-5A and 99-6C may thus reflect a signature of the K-metasomatism common to these samples, whereas other components in titanite from 99-5A show a "mixed" signature lying between strictly K-altered and Na-altered counterparts (Figs. 3-7a and b).

3.5 Major Mineral EPMA and LA-ICPMS Trace-Element Analyses

The major rock-forming minerals in the LMG host rocks consist of perthitic feldspar, microcline, albite, clinopyroxene (hedenbergite and aegerine-augite), fayalite olivine and fluorite (from 99-3A: fayalite granite), as well as quartz, magnetite and

hematite in most samples; of these, feldspar, clinopyroxene, olivine and fluorite were targeted for major- and trace-element analyses.

3.5.1 Feldspar

Electron microprobe and LA-ICPMS analyses were conducted both on discrete albite and microcline grains, as well as albite and microcline lamellae in perthitic grains (Table 3-6, Table B-5). Plagioclase in samples 99-2B and 99-5A (Na-altered samples, Fig. 1-3b and d) consist almost entirely of end-member albite (Ab_{96-100} for 99-2B and Ab_{98-100} for 99-5A). 99-5A is more perthitic (i.e., albite and microcline, Fig. 1-3d) and contains microcline lamellae with Or_{91-100}. Samples 99-6C, 99-6B (K-altered samples, Fig. 1-3e-f) and 99-3A (fayalite granite, Fig. 1-3c) consist primarily of microcline with Or contents ranging from 84-99 mol% for 99-6C, 91-97 mol% for 99-6B and 82-95 mol% for 99-3A. Feldspar from sample 99-3A is perthitic (Fig.1- 3c), with albite lamellae all consisting of Ab_{100}. The perthite in sample 99-3A consists mostly of flame perthite and is composed of intergrowths of flame shaped albite lamellae in an alkali feldspar host (Pryer et al., 1995; Pryer and Robin, 1995). Sample 99-1A, the least altered sample, contains perthite with Ab contents ranging from 81-100 mol% and Or contents ranging from 84-100 mol%. Ore sample 99-4A was the only ore with feldspar and contains <10 vol% heavily altered microcline and albite (Fig. 1-5c-d), with the majority of the sample consisting of magnetite and minor apatite and quartz.

Feldspar from the LMG consists almost entirely of Ab or Or, with little to no An component. CaO concentrations range from below detection to 1.30 wt.% in the 99-1A

albite lamellae. FeO ranges from 0.05-0.21 wt.% in 99-1A (Fig. 3-8a) with no apparent preference for the Na- or K-rich lamellae. Feldspars from sample 99-2B have higher FeO concentrations compared to 99-1A, ranging from 0.15 to 0.30 wt.%. Feldspars from sample 99-3A range from 0.06 to 0.91 wt.% FeO, with higher FeO values corresponding to the Na-rich lamellae and grains. In sample 99-5A, the FeO contents of feldspars range from 0.04-0.84 wt. % with no apparent preference between the K- and Na-rich lamellae. Feldspars from samples 99-6B and 99-6C range from below detection to 0.14 wt.%, and from below detection to 0.09 wt.% respectively (Table 3-6).

Table 3-6. EPMA major- and minor-element analyses of LMG host rock, NY-3 and SW-2B feldspar

Sample	99-1A														
Grain	10_5	4_1	4_2	4_3	4_4	2_1	2_2	2_3	2_5	2_6	6_1	6_2	6_3	6_4	6_5
wt. %															
SiO2	65.99	64.64	67.52	65.11	66.54	67.25	64.37	67.33	66.02	66.40	66.65	64.71	66.55	64.77	67.13
TiO2	-	-	-	0.04	-	-	-	0.02	0.01	0.01	-	-	-	-	0.00
Al2O3	19.65	18.55	19.95	18.88	19.90	20.19	18.60	20.25	20.41	20.75	20.84	18.77	20.00	18.60	20.53
FeO	0.09	0.10	0.13	0.08	0.16	0.10	0.06	0.12	0.12	0.07	0.06	0.05	0.12	0.05	0.10
MgO	-	-	-	-	0.01	-	-	-	0.00	-	-	-	-	-	-
MnO	-	0.02	0.02	-	0.01	0.00	-	-	0.01	-	0.01	-	-	0.01	-
BaO	0.07	0.20	-	0.08	0.06	0.04	0.26	-	0.03	-	0.02	0.21	0.02	0.26	-
SrO	0.04	-	0.13	0.05	0.11	0.04	0.02	0.11	0.06	0.16	0.12	-	0.10	-	0.17
CaO	0.55	0.03	0.51	0.09	0.62	0.53	-	0.75	0.69	1.29	1.29	-	0.71	0.01	1.00
Na2O	7.13	1.51	11.54	2.03	9.17	11.53	0.51	11.31	10.10	11.13	10.87	1.43	9.34	1.45	11.10
K2O	6.71	15.08	0.37	14.27	3.48	0.11	16.39	0.05	1.72	0.12	0.07	14.94	3.03	14.86	0.10
Total	100.22	100.13	100.17	100.63	100.06	99.80	100.22	99.93	99.17	99.93	99.93	100.11	99.86	100.00	100.14

Sample	99-2B												
Grain	1_4	7_1	7_2	7_3	7_4	10_1	10_2	10_3	10_4	6_1	6_2	8_1	8_2
wt. %													
SiO2	64.04	67.59	66.639	66.874	66.061	67.292	67.312	67.569	66.921	67.132	67.04	67.176	66.752
TiO2	-	0.01	-	-	-	-	0.0025	-	-	-	-	-	0.0155
Al2O3	18.98	20.50	20.406	20.467	20.456	20.665	20.695	20.657	20.826	20.251	20.402	20.343	20.42
FeO	0.04	0.15	0.1688	0.1743	0.1792	0.2328	0.2007	0.2334	0.1432	0.1979	0.1382	0.263	0.2293
MgO	-	-	-	-	0.0019	0.0054	-	-	-	0.0008	-	-	-
MnO	0.01	-	-	-	0.0122	-	0.0322	0.0404	0.0183	-	-	0.0155	0.0041
BaO	0.85	-	-	0.0284	-	0.0228	0.0172	-	-	-	-	-	-
SrO	0.00	0.14	0.0838	0.1049	0.1397	0.1045	0.0544	0.0367	0.0599	0.1431	0.1272	0.1064	0.0091
CaO	0.01	0.86	0.9745	0.8835	0.9912	0.9593	0.9825	0.9819	1.06	0.9257	0.8878	0.8762	0.9121
Na2O	1.09	11.26	11.26	11.31	11.32	11.4	11.34	11.26	11.30	11.46	11.44	11.34	11.38
K2O	15.41	0.12	0.1167	0.1024	0.0841	0.1734	0.1533	0.1844	0.1305	0.1503	0.1351	0.1265	0.1302
Total	100.42	100.64	99.648	99.946	99.249	100.86	100.79	100.96	100.46	100.26	100.17	100.25	99.856

Note: A dash where a value is missing means that for that element the concentration is below the minimum detection limit.

Sample	99-3A															
Grain	10_1	10_2	10_3	10_4	10_5	13_1	12_1	12_4	12_5	3_1	3_2	3_3	5_1	5_2	5_3	5_4
wt. %																
SiO2	68.33	64.25	68.38	68.08	64.70	64.82	64.86	68.29	64.92	65.30	64.67	62.99	67.88	64.16	67.72	64.79
TiO2	-	-	-	-	0.01	0.01	0.01	0.03	-	-	0.02	-	-	0.02	-	-
Al2O3	19.64	18.31	19.49	19.17	18.34	18.29	18.35	19.53	18.48	18.60	18.40	17.53	19.31	18.43	19.63	18.33
FeO	0.25	0.13	0.18	0.32	0.14	0.13	0.10	0.24	0.11	0.09	0.10	2.71	0.39	0.09	0.15	0.11
MgO	0.02	-	0.00	-	-	-	-	-	-	-	-	-	0.01	-	-	-
MnO	-	-	0.00	0.00	0.00	-	0.02	0.00	0.00	-	0.01	0.08	0.02	0.00	-	-
BaO	0.03	0.03	0.03	0.03	0.09	0.02	-	-	0.14	0.06	0.01	0.07	0.05	0.10	-	0.13
SrO	-	-	-	-	-	-	-	-	-	-	-	-	-	-	-	-
CaO	0.02	-	0.05	0.02	-	-	0.06	0.03	0.01	-	-	0.02	0.04	-	0.06	-
Na2O	11.72	0.76	11.70	11.57	0.79	1.33	1.75	11.61	1.67	2.11	2.13	0.47	11.53	1.37	11.59	1.00
K2O	0.06	15.73	0.07	0.08	15.78	15.02	14.40	0.07	14.53	13.82	13.81	15.35	0.06	14.94	0.14	15.47
Total	100.06	99.23	99.91	99.28	99.85	99.61	99.56	99.81	99.85	99.98	99.15	99.22	99.28	99.12	99.30	99.84

Sample	99-5A														
Grain	4_3	4_4	3_3	3_4	10_4	10_5	7_1	7_2	7_3	7_4	8_1	8_2	8_3	8_4	4_2
wt. %															
SiO2	64.38	67.69	67.60	63.46	67.71	64.68	67.55	67.66	63.76	64.97	67.50	64.18	67.80	67.70	67.72
TiO2	-	-	-	0.01	-	0.01	0.02	-	0.01	-	-	-	0.00	-	-
Al2O3	18.21	19.85	20.21	19.39	19.79	18.51	19.87	20.05	18.57	18.36	19.81	18.52	19.99	19.95	19.87
FeO	0.78	0.11	0.10	0.09	0.14	0.10	0.14	0.08	0.04	0.12	0.11	0.05	0.05	0.15	0.07
MgO	0.06	0.00	-	-	0.00	-	-	-	-	-	0.00	0.00	-	0.01	-
MnO	-	-	0.00	-	0.02	0.00	-	0.00	-	-	0.01	0.01	-	-	-
BaO	0.00	0.01	0.02	0.06	-	0.06	0.02	0.03	0.15	0.06	-	0.03	0.07	0.04	-
SrO	-	0.11	0.10	-	0.12	0.06	0.11	0.14	-	0.03	0.11	-	0.12	0.09	0.20
CaO	0.00	0.16	0.39	0.03	0.40	-	0.21	0.18	-	-	0.28	0.01	0.23	0.37	0.23
Na2O	0.37	11.41	11.36	0.37	11.62	0.43	11.68	11.69	0.30	0.76	11.66	0.52	11.62	11.47	11.36
K2O	15.84	0.09	0.12	16.33	0.16	16.33	0.11	0.08	16.51	15.94	0.13	16.37	0.08	0.17	0.11
Total	99.65	99.43	99.90	99.74	99.96	100.18	99.71	99.91	99.32	100.25	99.61	99.68	99.96	99.94	99.57

Note: A dash where a value is missing means that for that element the concentration is below the minimum detection limit.

Sample	99-6B								
Grain	4_3	4_4	2_2	5_1	5_2	5_3	1_2	4_1	4_2
wt. %									
SiO2	64.01	64.37	64.63	64.28	64.10	64.46	63.93	63.94	64.60
TiO2	-	-	0.03	-	0.01	-	0.02	0.02	0.01
Al2O3	18.82	18.87	18.73	18.82	18.75	18.94	18.81	19.08	18.78
FeO	0.00	0.02	0.01	0.05	0.09	0.07	0.05	0.03	0.05
MgO	-	-	-	-	-	-	-	-	-
MnO	0.00	-	0.01	0.02	0.02	0.01	0.00	-	0.00
BaO	0.60	0.65	0.63	0.74	0.60	0.70	0.80	0.58	0.58
SrO	0.01	0.00	-	-	-	-	-	-	-
CaO	-	0.01	-	0.01	0.02	0.02	0.01	-	-
Na2O	0.50	0.77	1.06	0.93	1.09	0.81	0.80	0.80	0.68
K2O	16.21	15.98	15.55	15.38	15.23	15.52	15.70	15.86	16.06
Total	100.15	100.67	100.67	100.23	99.91	100.53	100.12	100.32	100.78

Sample	99-6C														
Grain	4_1	4_2	4_3	5_2	5_3	5_4	2_1	2_2	2_3	2_4	3_4	1_1	1_2	4_4	5_1
wt. %															
SiO2	64.54	64.53	64.35	63.72	63.87	64.23	63.25	64.45	64.14	64.36	64.00	64.18	64.32	64.20	64.05
TiO2	0.00	0.01	0.02	-	-	0.03	0.00	0.02	0.00	-	-	-	0.01	-	0.01
Al2O3	18.95	19.02	18.81	18.83	18.77	18.72	18.59	18.83	19.00	18.95	18.89	18.63	18.85	19.02	18.91
FeO	0.06	0.00	0.03	0.03	0.03	0.09	0.02	0.01	0.05	0.02	0.01	0.07	0.03	0.00	0.02
MgO	-	-	-	-	-	-	-	-	-	-	-	-	-	-	-
MnO	-	0.00	0.02	-	-	0.03	-	-	-	-	0.01	-	-	0.02	-
BaO	0.85	0.82	0.97	0.92	0.87	0.80	0.89	0.85	0.91	0.81	0.84	0.94	1.17	1.02	0.79
SrO	0.00	-	0.00	0.00	0.02	0.03	-	-	0.03	0.02	0.07	-	0.01	-	-
CaO	0.02	0.02	-	0.01	-	-	0.01	0.01	0.06	0.03	0.00	-	-	-	-
Na2O	1.35	1.65	1.61	1.11	1.08	1.43	1.18	1.02	1.40	1.96	1.20	1.22	0.77	1.15	0.92
K2O	14.84	14.59	14.65	15.24	15.35	14.64	15.11	15.47	14.62	14.05	15.37	15.48	15.81	15.16	15.61
Total	100.61	100.62	100.45	99.86	100.00	100.01	99.06	100.66	100.20	100.21	100.39	100.51	100.96	100.57	100.29

Note: A dash where a value is missing means that for that element the concentration is below the minimum detection limit.

Sample	NY-3														
Grain	2_1	2_2	2_3	2_4	3_1	3_2	3_4	4_1	4_2	4_3	4_4	5_1	5_2	5_3	5_4
wt. %															
SiO2	65.21	63.69	60.37	60.39	61.01	63.80	64.93	63.48	64.02	64.84	64.72	64.77	64.80	63.63	63.37
TiO2	-	-	-	-	0.00	0.00	0.00	-	0.00	-	-	-	-	-	-
Al2O3	18.762	18.12	21.85	21.69	21.54	22.62	19.27	22.76	22.81	20.91	18.54	18.75	18.72	23.03	22.67
FeO	0.0083	0.11	0.11	0.05	0.06	0.05	0.03	0.06	0.03	0.39	0.01	0.03	0.07	0.09	0.02
MgO	-	-	-	0.00	-	-	-	0.00	0.02	0.05	-	-	-	0.01	0.02
MnO	0.002	-	0.00	0.03	0.00	0.00	-	0.01	-	-	-	-	0.01	-	-
BaO	0.2952	0.46	0.01	0.07	0.05	-	0.29	-	0.07	0.04	0.50	0.56	0.51	-	-
SrO	0.0092	0.10	0.18	0.11	0.09	0.21	0.06	0.17	0.14	0.06	0.10	0.07	0.08	0.12	0.08
CaO	0.3638	0.07	4.00	4.14	4.05	4.16	0.67	4.09	3.85	2.16	0.08	0.12	0.07	3.90	3.99
Na2O	2.9108	4.03	9.18	9.09	8.98	9.07	3.36	9.08	9.36	7.88	2.03	1.62	1.58	9.43	9.30
K2O	12.492	10.66	0.32	0.31	0.34	0.34	11.04	0.41	0.27	3.85	13.53	14.27	14.40	0.25	0.30
Total	100.05	97.23	96.02	95.88	96.13	100.24	99.65	100.06	100.56	100.17	99.50	100.19	100.23	100.45	99.75

Sample	SW-2B												
Grain	3_2	3_3	3_4	5_1	5_2	5_4	4_1	4_2	4_3	4_4	4_5	4_6	3_1
wt. %													
SiO2	64.53	65.94	65.81	64.34	64.49	66.03	65.95	66.32	64.89	64.37	64.73	65.92	64.33
TiO2	0.02	0.01	0.01	0.00	-	-	-	-	-	-	-	-	0.02
Al2O3	18.71	21.17	21.00	18.61	18.72	20.83	20.83	21.03	18.84	18.82	18.72	21.53	18.82
FeO	-	0.02	0.00	0.02	-	0.01	0.00	0.03	-	0.01	-	-	0.05
MgO	-	-	0.00	-	-	-	0.01	-	-	-	-	0.00	-
MnO	0.00	-	-	-	-	-	-	-	-	-	0.02	0.00	0.01
BaO	0.03	0.02	0.06	-	0.12	0.05	-	-	0.01	-	-	0.12	0.02
SrO	0.03	0.09	0.03	0.00	0.01	0.04	0.12	0.10	0.01	0.07	-	0.11	-
CaO	0.01	1.86	1.80	0.04	0.01	1.43	1.52	1.52	0.02	0.01	-	1.95	0.01
Na2O	1.08	10.77	10.66	1.10	1.01	10.93	10.91	11.03	1.28	0.88	0.79	10.65	0.99
K2O	15.58	0.22	0.32	15.59	15.72	0.35	0.21	0.15	15.24	16.12	16.02	0.25	15.76
Total	100.02	100.10	99.68	99.70	100.09	99.67	99.55	100.18	100.29	100.28	100.29	100.54	100.00

Note: A dash where a value is missing means that for that element the concentration is below the minimum detection limit.

Feldspars from samples 99-6C and 99-6B contain the highest Ba contents, ranging from 3752-5665 ppm (Fig. 3-8b, Table B-5). Sample 99-2B has the most consistently low Ba concentrations in feldspar (5.60-6.84 ppm), whereas 99-5A has the lowest individual analysis with 1.11ppm Ba, but ranges up to 467 ppm Ba. All other samples fall within this range in Ba concentrations, with values from 0.42 to 1276 ppm. In general, the higher Ba concentrations are associated with microcline grains and K-rich lamellae in the perthitic grains (e.g., 99-6B and 99-6C) whereas lower Ba concentrations correlate with the Na-rich lamellae and albite (99-2B).

The Sr concentrations range from 3-286 ppm (Fig. 3-8b) with both the lowest and some of the highest values from sample 99-3A. Sr concentrations in feldspars from all other samples fall within the range represented by sample 99-3A (Table 3-6, Table B-5) with the microcline grains and K-rich lamellae generally showing higher Sr than the Na-rich lamellae and grains.

Feldspars from Na-metasomatised samples 99-2B and 99-5A have the lowest REE among the samples, whereas the highest REE concentrations are found in feldspars from 99-3A. Overall, the feldspars are depleted in REE (with the exception of some feldspar from 99-3A) compared to the reference feldspar samples NY-3, which is an unaltered charnockite from the Adirondacks, and SW-2B, which is peraluminous granite from the Sweetwater Wash Pluton in the Mojave Desert, California (both collected by J.M. Hanchar) (Fig. 3-8a). The LMG feldspar crystals (especially the Na-metasomatised samples) generally have lower total REE concentrations compared to reference feldspars in Figure 3-8a, and compared to feldspars from a (non-exhaustive) literature survey (e.g.,

Hall, 1967; Ginibre, et al., 2002; Larsen, 2002; Slaby et al., 2007; Hovelmann et al., 2010).

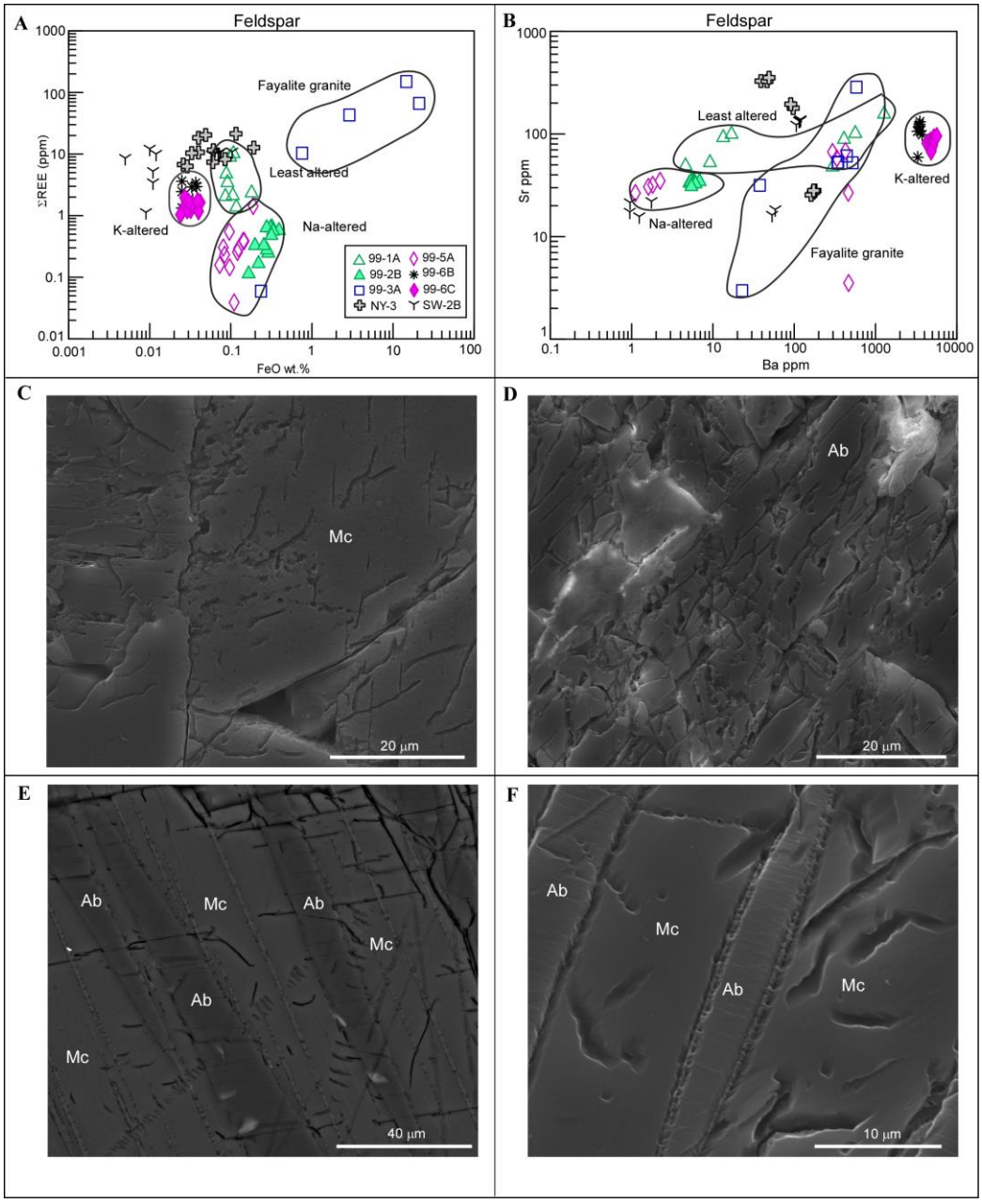

Figure 3-8: A) Plot of FeO (wt.%) vs. ΣREE (ppm) for the LMG samples with unaltered feldspar samples NY-3 and SW-2B (for comparison). LMG feldspar for the most part are depleted in REE overall compared to the unaltered samples with the exception of 99-3A which has higher REE and

FeO. B) Plot of Ba (ppm) vs. Sr (ppm) of the LMG feldspar and unaltered feldspar samples NY-3 and SW-2B demonstrating different populations of feldspar from different samples. Ba enriched samples are microcline where as Ba poor samples are the albite. C) Secondary electron image of 99-6C microcline with pores and microchannels indicating alteration. D) SEI image of albite from 99-2B with well-developed microchannels and pores, more dominant than 99-6C indicating more alteration. E) SEI image of 99-1A perthite with albite (Ab) and microcline (Mc) lamellae. F) SEI image of 99-3A perthite with albite (Ab) and microcline (Mc) lamellae.

Scanning electron microscope secondary electron imaging of the LMG feldspar was done following the methods of Waldron et al. (1994) using HF acid vapour etching to enhance any perthitic textures if they exist in the sample. HF acid etching emphasizes perthitic textures because microcline is more readily dissolved compared to albite, such that the perthitic textures as well as any pores, channels, or cleavage intersections are enhanced by etching. Figure 3-8c and d are examples of the two end-member samples: Figure 3-8c shows a grain composed predominately of microcline from sample 99-6C, whereas and Figure 3-8d shows a feldspar from 99-2B which is composed predominantly of albite. These images demonstrate the micropores and channels present in the feldspar, suggesting that alteration within sample 99-2B, was more intense relative to 99-6C (Fig. 3-8c and d) Figures 3-8e and f show feldspar from samples 99-3A and 99-1A, respectively, showing the perthitic textures enhanced by the HF etching in these samples.

3.5.2 Clinopyroxene

Clinopyroxene was found in only three of the LMG samples; ore sample 06-4B, and host rock samples 99-2B and 99-3A. The compositions of the clinopyroxene are hedenbergite (with pigeonite exsolution lamellae) for 99-3A and a more Na-rich augite-

aegerine for 06-4B and 99-2B. Major-, minor- and trace-elements from the LMG clinopyroxene from host rock and ore samples are reported in Table 3-7 and Table B-6.

Table 3-7. Clinopyroxene major-, minor- and trace-element LA-ICPMS analyses from the LMG host rock and ore samples

Sample	99-2B (Na-altered)						06-4B (Ore)							99-3A (Fayalite granite)				
Grain	gr. 1	gr.1	gr. 3	gr. 4	gr. 4	gr. 5	gr. 5	gr. 5	gr. 8	gr. 8	gr. 9	gr. 13	gr. 13	gr. 14	gr. 14	gr. 7	gr. 9	gr. 9
wt. %																		
SiO2	69.0	72.1	64.8	52.6	51.8	50.1	49.8	50.2	48.5	50.3	49.2	50.5	49.8	49.1	55.1	49.8	44.4	45.6
TiO2	0.09	0.10	0.12	0.12	0.11	0.10	0.06	0.06	0.06	0.06	0.06	0.06	0.06	0.29	0.33	0.27	0.26	0.26
FeO	8.93	36.6	32.4	33.9	32.9	28.6	14.5	14.8	14.0	14.1	14.3	14.7	14.5	104	192	334	31.5	33.3
MgO	5.62	5.79	5.45	4.93	4.54	4.65	10.4	10.4	9.92	10.4	10.1	10.7	10.5	0.24	0.27	0.24	0.26	0.27
CaO	16.2	16.1	16.4	16.2	16.2	16.1	19.8	20.1	19.7	19.8	19.9	20.0	19.7	17.1	17.6	17.1	17.4	18.0
ppm																		
Mn	1519	1505	2033	2126	2102	1745	1068	1054	1023	1040	1038	1085	1068	8283	9832	8361	17553	18511
Sc	45.3	42.9	46.4	51.9	51.3	50.7	66.3	66.1	62.3	62.0	63.8	62.7	61.8	20.6	23.6	22.0	20.6	21.8
V	3.32	3.60	3.76	3.74	3.88	3.75	55.9	55.1	54.9	56.5	55.1	56.9	56.7	1.06	1.41	1.24	1.20	1.24
Co	23.4	22.6	22.2	25.9	26.5	26.2	14.3	14.5	14.2	14.7	14.8	13.9	14.5	1.89	2.25	2.03	1.93	1.99
Ni	-	-	-	-	4.68	-	49.3	46.5	45.3	43.6	46.7	46.4	47.5	-	-	-	-	-
Cu	7.57	13.34	2.47	5.11	3.02	1.96	-	-	-	-	-	-	-	-	1.70	1.06	0.94	1.12
Zn	59.4	67.4	60.1	74.8	66.4	62.3	17.3	17.2	18.0	16.6	16.5	16.2	17.5	779	913	752	686	730
As	358	423	253	2.59	0.32	-	2.15	2.02	2.12	1.97	2.09	2.03	2.03	7.51	9.22	7.46	3.70	3.23
Sr	14.0	16.1	10.8	3.72	3.35	3.65	7.00	6.55	6.91	6.55	6.67	6.49	6.49	8.46	21	9.60	8.00	8.80
Y	5.34	5.45	7.71	3.43	1.85	0.85	114	108	104	104	106	104	101	678	720	702	693	719
Zr	138	167	225	182	177	189	107	96.9	82.9	89.3	92.8	78.5	80.5	193	248	230	285	302
Nb	0.24	0.27	0.19	0.09	0.03	0.03	0.93	0.83	0.81	0.75	0.79	0.82	0.80	0.76	0.99	0.62	0.62	0.51
Sn	26.5	28.5	31.6	15.5	12.2	13.6	18.5	18.3	20.0	20.5	19.1	19.9	19.1	17.5	24.7	17.4	24.9	23.9
Ba	72.8	85.4	47.7	0.92	-	0.65	-	-	0.37	-	0.33	-	-	1.05	8.15	1.93	1.01	0.18
La	10.8	7.21	2.51	12.9	6.45	2.33	12.7	11.8	11.3	11.6	13.0	11.9	11.8	75.3	95.0	75.3	88.1	94.7
Ce	27.3	20.8	12.1	34.0	20.7	8.7	51.8	49.1	47.6	48.9	51.3	49.8	50.7	325	385	324	393	421
Pr	3.51	3.02	2.50	4.32	3.16	1.56	9.21	8.51	8.51	8.74	8.71	8.54	8.69	61.0	72.0	61.6	79.2	84.6
Nd	13.5	11.5	12.5	16.3	12.5	6.5	46.2	44.7	40.3	42.9	43.7	43.7	44.2	326	377	326	405	430
Sm	2.20	1.78	2.92	2.36	1.85	0.98	13.9	13.4	12.7	13.0	13.2	13.7	12.8	99.2	112	102	123	130
Eu	0.38	0.27	0.48	0.35	0.26	0.15	2.22	2.00	2.00	1.94	1.89	2.06	2.01	7.25	8.30	7.74	9.95	10.4
Gd	1.29	1.32	2.14	1.36	0.97	0.58	16.8	16.8	15.4	16.0	15.4	15.4	15.6	107	120	112	131	141
Tb	0.19	0.16	0.27	0.13	0.08	0.05	3.03	2.91	2.69	2.78	2.77	2.82	2.71	19.7	21.6	20.5	24.6	25.4
Dy	1.14	1.05	1.46	0.68	0.42	0.26	19.2	18.0	17.5	17.8	17.1	17.5	17.0	142	153	148	164	169
Ho	0.20	0.19	0.29	0.11	0.07	0.05	4.99	4.69	4.51	4.52	4.48	4.48	4.38	29.6	31.0	30.5	34.6	35.4
Er	0.66	0.50	0.92	0.34	0.19	0.12	13.4	13.1	12.4	12.6	12.1	11.8	11.6	87.8	94.4	90.9	96.5	99.7
Tm	0.13	0.13	0.21	0.10	0.04	0.04	2.80	2.69	2.53	2.63	2.49	2.50	2.47	15.0	15.5	15.4	19.9	20.6
Yb	1.90	2.06	4.23	1.51	0.96	0.64	18.7	17.7	16.3	17.5	16.7	16.8	16.6	121	124	127	131	137
Lu	0.67	0.62	1.59	0.69	0.51	0.34	5.65	5.34	4.97	4.99	4.91	4.87	4.88	21.0	22.2	22.2	23.8	24.8
Hf	8.32	9.40	10.9	9.98	10.7	11.4	4.01	3.92	3.85	3.99	3.79	3.38	3.44	15.2	19.3	15.8	20.0	21.9
Ta	-	0.03	0.02	-	0.01	0.01	0.12	0.09	0.10	0.09	0.08	0.09	0.08	0.10	0.10	0.09	0.08	0.11
Th	0.20	0.21	0.21	0.12	0.01	0.04	0.17	0.16	0.13	0.10	2.34	0.17	0.08	0.04	0.06	0.03	0.02	0.04
U	0.11	0.12	0.09	0.07	0.01	0.03	0.56	0.07	0.26	0.06	0.44	0.07	0.05	0.02	0.03	0.02	0.02	0.02

Note: A dash where a value is missing means that for that element the concentration is below the minimum detection limit.

The chondrite normalized REE plots for the clinopyroxene analyses are shown in Figure 3-9a. Clinopyroxene from samples 99-3A and 06-4B have similar REE patterns, showing a convex upwards pattern between La to Eu, a fairly strong negative Eu anomaly, a flat pattern from Sm to Er, and a slight enrichment in the HREE. Between these two samples, clinopyroxene from sample 06-4B has almost an order of magnitude lower in total REE and a less prominent Eu anomaly compared to 99-3A. Sample 99-2B the REE pattern is different than the others with convex-up LREE and convex-down HREE, and lower REE in general than the other two samples (Fig. 3-9a). Note that sample 99-3A (with the highest REE concentrations in clinopyroxene; Fig. 3-9a) also has the highest REE concentrations in both apatite and feldspar (Figs. 3-5b and 3-8a), whereas sample 99-2B (with the lowest REE in clinopyroxene) has among the lowest REE concentrations in feldspar (Fig. 3-8a).

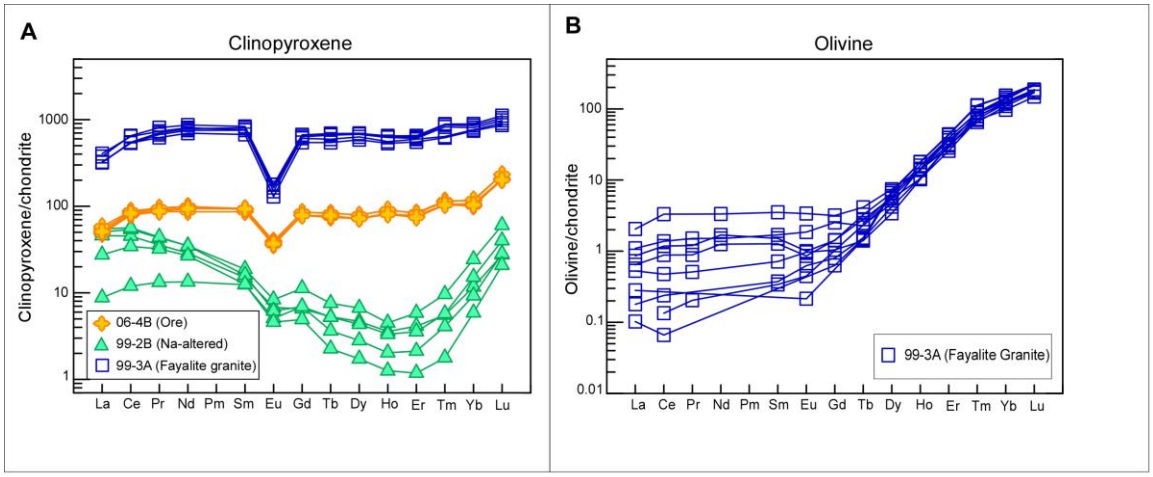

Figure 3-9: A) Anders and Grevesse (1989) chondrite normalized REE plots of clinopyroxene from ore and host rock samples 06-4B, 99-2B and 99-3A. B) Anders and Grevesse (1989) chondrite normalized REE plot for olivine (fayalite) sample 99-3A.

3.5.3 Olivine

Olivine was found in only one sample, 99-3A, and is composed of near-end-member fayalite (Table 3-8a and b). The fayalite has low MgO, Ni and Cr which may indicate a strongly fractionated magmatic or metasomatic origin. The fayalite has few measurable trace-elements; most are near or below the detection limits for LA-ICPMS with the exception of Zn and Y. The total REE range from 30-43 ppm (Table 3-8b). Figure 3-9b shows a chondrite normalized REE pattern for olivine that is generally flat from La-Eu with a positive slope from Gd-Lu.

Table 3-8a. Olivine major- and minor-element EPMA analyses from LMG fayalite granite

Sample	**99-3A (Fayalite granite)**						
Grain	17_2	18_1	18_2	19_1	19_2	2_2	3_2
SiO2	29.3	29.7	28.6	28.9	29.2	29.7	29.3
TiO2	-	-	-	-	-	-	-
Al2O3	0.01	0.01	0.01	0.00	0.01	0.03	-
FeO	68.7	68.3	68.7	68.2	68.6	68.5	69.0
MnO	2.12	2.00	2.07	2.04	2.03	2.27	2.04
MgO	0.17	0.17	0.17	0.18	0.17	0.17	0.20
CaO	-	-	-	0.02	0.00	-	0.00
Na2O	0.04	-	-	-	-	0.06	-
NiO	-	-	0.00	0.01	-	0.00	-
Cr2O3	-	-	-	-	-	-	-
Total	100.27	100.12	99.60	99.34	99.98	100.74	100.57

Note: A dash where a value is missing means that for that element the concentration is below the minimum detection limit.

Table 3-8b. Olivine LA-ICPMS major-, minor- and trace-element analyses from LMG fayalite granite

Sample	99-3A (Fayalite granite)						
Grain	gr. 17_2	gr. 18_1	gr. 18_2	gr. 19_1	gr. 19_2	gr. 2_2	gr. 3_2
wt. %							
SiO2	29.3	29.7	28.6	28.9	29.2	29.7	29.3
TiO2	0.00	0.01	0.01	0.00	0.01	0.00	0.01
FeO	70.8	72.9	69.7	68.8	71.7	71.9	71.0
MgO	0.15	0.18	0.18	0.16	0.18	0.17	0.17
P2O5	0.01	0.01	0.01	0.01	0.01	0.01	0.01
CaO	0.05	0.05	0.08	0.07	0.06	0.06	0.07
ppm							
Sc	1.71	2.61	2.32	2.44	2.23	1.85	1.84
V	-	-	-	-	-	-	-
Cr	-	-	19.2	11.1	8.82	6.69	-
Mn	39795	40250	38757	38548	12851	14260	12880
Co	4.00	4.57	4.21	4.08	4.41	4.81	4.47
Ni	-	-	-	-	46.3	52.9	9.38
Cu	-	-	-	-	-	-	-
Zn	1792	1965	1893	1723	1783	2047	1886
As	-	-	0.29	-	-	-	-
Sr	2.41	0.11	0.80	1.36	1.66	1.05	0.06
Y	16.9	26.1	25.4	19.1	21.2	36.3	34.7
Zr	0.36	0.13	0.11	0.15	0.12	-	0.08
Nb	4.58	0.14	0.20	0.18	0.17	0.37	0.21
Sn	3.30	4.43	13.21	4.69	2.44	1.25	1.26
Ba	2.67	-	0.60	1.46	1.64	1.04	-
La	0.26	0.07	0.04	0.20	0.15	0.12	0.02
Ce	0.83	-	0.14	0.71	0.53	0.29	0.04
Pr	0.15	-	-	0.12	0.09	0.05	-
Nd	0.70	-	-	0.79	0.59	-	-
Sm	0.25	-	0.06	0.22	0.19	0.11	-
Eu	0.10	0.01	0.04	0.06	0.05	0.05	-
Gd	0.50	-	0.16	0.28	0.28	0.21	0.12
Tb	0.08	0.05	0.06	0.12	0.10	0.05	0.06
Dy	1.33	1.60	1.70	1.59	1.37	0.83	1.02
Ho	0.58	1.00	0.99	0.77	0.78	0.57	0.59
Er	4.09	6.99	6.82	5.05	5.75	4.85	4.88
Tm	1.69	2.72	2.67	2.12	1.90	1.75	1.57
Yb	15.8	25.0	24.8	20.6	20.2	19.2	17.8
Lu	3.61	5.39	5.15	4.51	4.54	4.50	4.11
Hf	-	-	-	0.02	0.02	-	-
Ta	-	0.01	-	-	-	0.01	0.01
Th	0.00	0.00	-	0.00	-	-	-
U	-	-	0.00	0.00	-	-	-

Note: A dash where a value is missing means that for that element the concentration is below the minimum detection limit.

3.5.4 Fluorite

Fluorite was identified in thin section from host rock samples 99-3A as a minor phase occurring along grain boundaries and fractures. Fluorite is also present in samples 99-5A, AH-06-6B and 99-4A (i.e., found in the heavy mineral concentrates) but was not identified or not large enough for analyses in thin sections of these samples. LA-ICPMS major-, minor- and trace-elements analyses were not obtained from the LMG fluorite due to difficulties ablating fluorite (i.e., poor coupling of the laser to the fluorite crystals); however EPMA data were acquired from fluorite and are reported in Table 3-9. Ca in fluorite sample 99-3A ranges from 48.70-54.56 wt. %, F ranges from 43.09-46.25 wt.% and Na ranges from 0.05-0.09 wt.% (Table 3-9).

Table 3-9. Fluorite major- and minor-element EPMA analyses from the LMG

Sample	**99-3A (Fayalite granite)**										
Grain	gr. 15	gr. 15	gr. 15	gr. 2	gr. 2	gr. 2	gr. 2	gr. 5	gr. 5	gr. 5	gr. 5
wt. %											
F	46.3	44.9	46.2	43.1	45.9	45.7	45.6	44.9	45.6	45.8	45.0
Ca	53.6	48.7	52.8	52.5	54.6	52.4	53.7	53.2	52.0	51.1	53.2
Fe	-	-	0.02	3.27	0.01	0.01	0.02	-	0.00	0.00	0.03
Mn	0.00	-	-	0.07	-	-	-	-	0.00	-	-
Mg	0.01	0.00	0.00	0.01	-	-	0.00	0.00	0.00	0.00	-
Na	0.09	0.05	0.07	0.05	0.08	0.08	0.07	0.08	0.08	0.05	0.05
Al	0.01	-	-	0.13	-	-	-	-	0.00	0.00	0.00
Si	-	-	-	1.22	-	-	-	-	-	-	-
Ti	-	-	-	-	-	-	-	-	-	-	-

Note: A dash where a value is missing means that for that element the concentration is below the minimum detection limit.

3.6 U-Pb geochronology

3.6.1 Apatite

Isotope dilution-TIMS U-Pb analyses were done on representative apatite and titanite grains from both the host granites and ores. Grains were selected based on color, size, and shape. The U-Pb ID-TIMS dates reported are much younger than the host and ore zircon previously reported by Valley et al. (2009; 2011).

Stacked Concordia plots of the LMG apatite for comparison between samples and also between the ores and host rocks are plotted in Figure 3-10a. Figure 3-10b-j show individual Concordia plots for the LMG apatite samples (ores in red and host rocks in black). The apatite dates for both ore and host rock range from 1008-826 Ma with the exception of ore 06-4B (Fig.3-10b), which is thought to be the oldest ore sample (Valley et al., 2010). Some of the apatite dates from 06-4B are the oldest among the samples, with $^{207}Pb/^{206}Pb$ dates ranging from about 1069-932 Ma (Table 3-10). Sample 99-5A also contains apatite grains with dates younger than 853-839 Ma, with discordant ages around 780 to 740 Ma (Fig. 3-10j). Similarly to the heterogeneous intra-sample mineral chemistry noted above for sample 99-5A, this sample exhibits a wide variation in apatite ages. Samples 06-4B and 99-5A both exhibit some reverse discordance, which indicates Pb gain or U loss. Sample 99-5A also exhibits discordance indicating Pb loss or U gain. A similar pattern is seen in zircon with many having higher U in the rims versus the older cores.

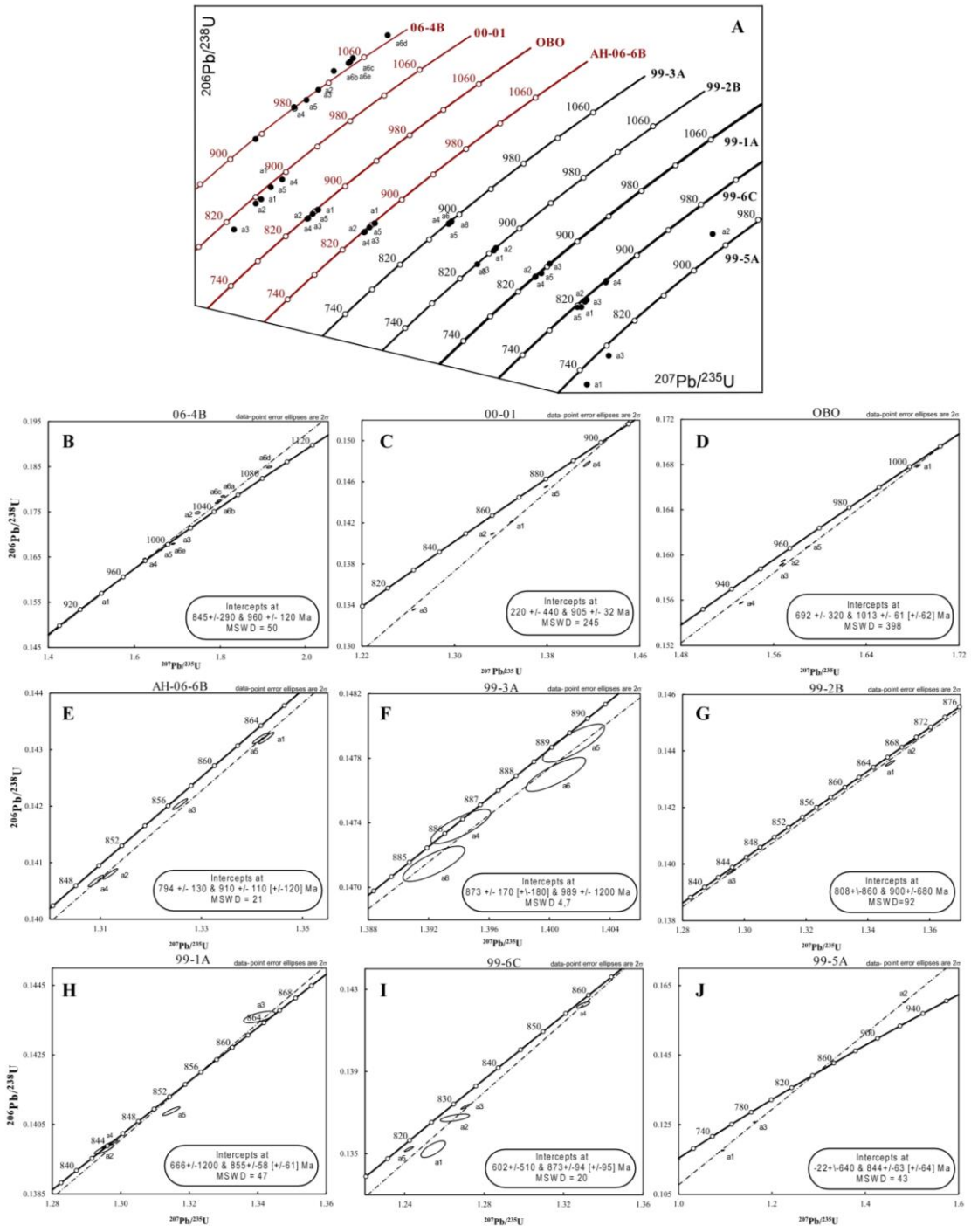

Figure 3-10: ID-TIMS U-Pb apatite geochronology. A) Stacked Concordia plots from ore (red) and host rock (black) apatite indicating a trend around 820-900 Ma. Some plots show reverse discordance which could indicate Pb gain or U loss or analytical problems. B-J) Individual apatite U-Pb Concordia diagrams with intercept ages. B) 06-4B, C) 00-01, D) OBO, E) AH-06-6B, F) 99-3A, G) 99-2B, H) 99-1A, I) 99-6C and J) 99-5A.

Note that overall both ore and host apatite are younger than the ore and host rock zircon, indicating that whatever process reset the apatite ages, or crystallized younger apatite, pervasively penetrated both the younger iron ores and the older host granites. The apatite ID-TIMS ages are corroborated by Sm-Nd isochron ages for samples 99-5A (901 ± 46 Ma) and AH-06-6B (857 ± 23 Ma) (see below).

3.6.2 Titanite

Stacked Concordia plots for the U-Pb dates for titanite from samples 99-2B, 99-5A, and 99-6C analysed by ID-TIMS can be found in Figure 3-11a. Detailed individual Concordia diagrams for each sample are presented in Figure 3-11b-d. The titanite is mostly older than the apatite and more similar in age to the ore zircon with the youngest samples from 99-5A having dates ranging from ~ 975 to 950 Ma. The U-Pb dates for the titanite from sample 99-6C are older, ranging from around 1030 to 1010 Ma (Table 3-10).

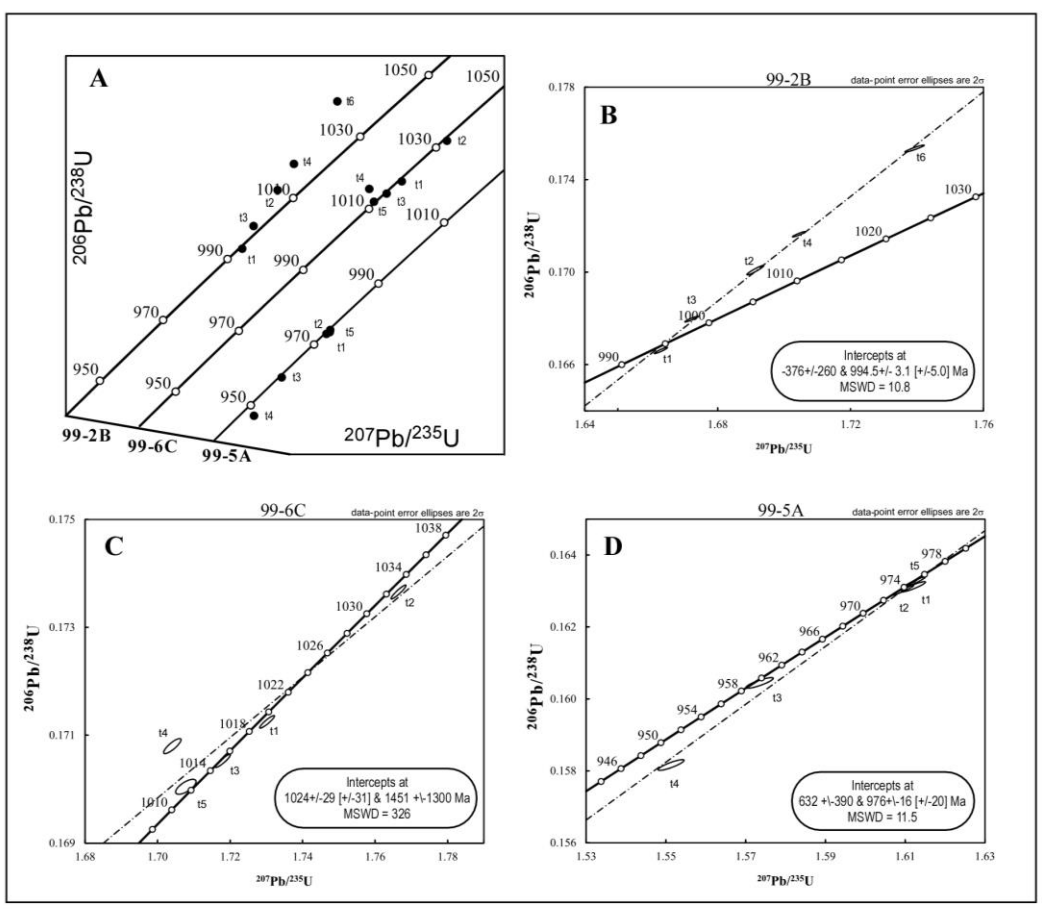

Figure 3-11: ID-TIMS U-Pb titanite geochronology. A) Stacked Concordia plots of titanite samples 99-2B, 99-5A and 99-6C. 99-6C and 99-2B have similar ages however 99-5A are much younger. B) U-Pb Concordia of 99-2B with intercept ages. This sample demonstrates reverse discordance which could indicate Pb gain or U loss or analytical problems. C) U-Pb Concordia of 99-6C with intercept ages. Two of the titanite from this sample exhibit reverse discordance. D) U-Pb Concordia of 99-5A with intercept ages.

The titanite from sample 99-2B exhibits reverse discordance, with ages from ~1035 to 990 Ma. The titanite is younger than the zircon from sample 99-2B. The oldest titanite from sample 99-2B (1035 Ma) is consistent with zircon SIMS U-Pb Concordia ages of 1033 ± 8.6 Ma from the same sample (Valley et al., 2011). Zircon crystals from

the ore, which are thought to be hydrothermal (Valley et al., 2009), range from 1038.9 ± 4.4 to 1000.9 ± 9.2 Ma, overlapping in age with titanites from 99-2B and 99-6C.

Table 3-10. Apatite and titanite ID-TIMS U-Pb results for the Lyon Mountain Granite

						Radiogenic Isotope Ratios									Isotopic Dates					
	Th	$^{206}Pb^*$	mol %	Pb^*	Pb_c	^{206}Pb	^{208}Pb	^{207}Pb		^{207}Pb		^{206}Pb		corr.	^{207}Pb		^{207}Pb		^{206}Pb	
Sample	U	x10^{-13} mol	$^{206}Pb^*$	Pb_c	(pg)	^{204}Pb	^{206}Pb	^{206}Pb	% err	^{235}U	% err	^{238}U	% err	coef.	^{206}Pb	±	^{235}U	±	^{238}U	±
(a)	(b)	(c)	(c)	(c)	(c)	(d)	(e)	(e)	(f)	(e)	(f)	(e)	(f)		(g)	(f)	(g)	(f)	(g)	(f)
										Apatite										
AH-06-6B																				
a1	3.484	58.730	99.82%	291	8.93	9674	1.071	0.0680	0.044	1.3428	0.093	0.1432	0.057	0.937	868.78	0.92	864.46	0.54	862.77	0.46
a2	3.524	25.035	99.88%	449	2.48	14897	1.084	0.0676	0.044	1.3120	0.091	0.1408	0.054	0.941	855.68	0.92	850.99	0.52	849.19	0.43
a3	3.567	27.757	99.88%	427	2.91	14082	1.096	0.0677	0.044	1.3258	0.092	0.1420	0.055	0.941	859.31	0.91	857.04	0.53	856.17	0.44
a4	3.580	27.345	99.82%	293	4.18	9642	1.101	0.0675	0.046	1.3091	0.096	0.1407	0.061	0.929	853.08	0.95	849.75	0.55	848.48	0.48
a5	3.689	9.893	99.75%	213	2.12	6931	1.133	0.0680	0.053	1.3417	0.097	0.1432	0.053	0.920	867.15	1.09	863.98	0.57	862.74	0.43
OBO																				
a1	6.210	168.051	99.77%	312	33.18	7405	1.895	0.0728	0.043	1.6848	0.092	0.1679	0.055	0.944	1007.99	0.88	1002.80	0.58	1000.42	0.51
a2	5.915	114.072	99.81%	373	18.29	9120	1.813	0.0713	0.043	1.5683	0.091	0.1595	0.055	0.944	966.54	0.89	957.76	0.56	953.93	0.48
a3	6.160	106.018	99.80%	359	18.12	8557	1.890	0.0714	0.044	1.5669	0.093	0.1592	0.057	0.937	968.91	0.90	957.21	0.58	952.12	0.51
a4	6.040	66.219	99.75%	285	14.12	6862	1.866	0.0713	0.045	1.5321	0.091	0.1558	0.052	0.944	967.11	0.92	943.33	0.56	933.17	0.45
a5	6.129	69.692	99.78%	326	13.08	7794	1.880	0.0717	0.046	1.5895	0.093	0.1607	0.056	0.933	978.03	0.93	966.09	0.58	960.85	0.50
00-01																				
a1	2.925	66.627	99.59%	117	23.28	4215	0.909	0.0689	0.050	1.3495	0.095	0.1421	0.054	0.924	894.48	1.02	867.32	0.55	856.73	0.43
a2	3.427	48.070	99.59%	125	16.96	4177	1.065	0.0686	0.049	1.3327	0.095	0.1409	0.054	0.925	886.21	1.02	860.07	0.55	849.96	0.43
a3	3.492	62.932	99.65%	151	18.70	4954	1.104	0.0687	0.049	1.2648	0.094	0.1336	0.054	0.925	889.18	1.01	830.08	0.53	808.18	0.41
a4	3.504	16.441	99.02%	53	13.75	1773	1.082	0.0694	0.066	1.4143	0.170	0.1477	0.142	0.925	911.49	1.36	894.98	1.01	888.31	1.18
a5	3.424	20.696	99.53%	110	8.28	3690	1.055	0.0687	0.052	1.3792	0.097	0.1455	0.053	0.917	890.65	1.08	880.08	0.57	875.88	0.44
06-4B																				
a1	4.594	74.133	97.97%	29	131.50	839	1.404	0.0701	0.098	1.5042	0.135	0.1555	0.068	0.716	932.47	2.01	932.10	0.82	931.94	0.59
a2	4.639	51.021	93.52%	9	301.93	263	1.392	0.0725	0.254	1.7464	0.263	0.1748	0.128	0.310	998.95	5.16	1025.84	1.70	1038.50	1.22
a3	3.347	61.567	97.69%	21	124.22	740	1.017	0.0727	0.104	1.6987	0.136	0.1695	0.067	0.675	1005.51	2.10	1008.04	0.87	1009.20	0.62
a4	4.117	57.210	97.21%	20	140.10	612	1.250	0.0715	0.121	1.6233	0.152	0.1646	0.075	0.615	972.23	2.47	979.28	0.96	982.42	0.69
a5	4.737	44.910	97.54%	24	96.60	695	1.444	0.0723	0.115	1.6619	0.147	0.1666	0.070	0.642	995.65	2.34	994.10	0.93	993.40	0.64
a6a	6.178	8.579	95.75%	16	32.48	402	1.855	0.0734	0.174	1.8054	0.195	0.1784	0.089	0.455	1024.52	3.52	1047.43	1.28	1058.45	0.87
a6b	5.672	3.738	96.21%	17	12.56	452	1.708	0.0734	0.170	1.7919	0.196	0.1770	0.082	0.507	1025.38	3.43	1042.53	1.27	1050.73	0.79
a6c	5.334	2.904	96.13%	16	9.96	443	1.605	0.0734	0.195	1.7969	0.222	0.1775	0.084	0.490	1026.18	3.95	1044.34	1.45	1053.04	0.82
a6d	5.516	1.494	96.48%	18	4.63	490	1.658	0.0750	0.224	1.9131	0.261	0.1849	0.099	0.542	1069.27	4.50	1085.68	1.74	1093.88	1.00
a6e	6.040	3.077	97.10%	24	7.83	591	1.846	0.0730	0.165	1.6898	0.196	0.1679	0.074	0.574	1013.20	3.35	1004.68	1.25	1000.78	0.68
99-2B																				
a1	6.749	71.208	99.78%	348	13.33	7819	2.073	0.0681	0.045	1.3472	0.093	0.1436	0.057	0.936	870.24	0.93	866.33	0.54	864.80	0.46
a2	4.949	45.919	99.74%	240	10.25	6562	1.518	0.0680	0.045	1.3539	0.093	0.1443	0.056	0.942	869.62	0.93	869.22	0.55	869.07	0.46
a3	5.847	45.833	99.87%	530	5.13	13099	1.797	0.0673	0.045	1.2957	0.092	0.1397	0.056	0.933	845.73	0.94	843.82	0.53	843.10	0.44

						Radiogenic Isotope Ratios										Isotopic Dates					
	Th	$^{206}Pb^*$	mol %	Pb^*	Pb_c	^{206}Pb	^{208}Pb	^{207}Pb		^{207}Pb		^{206}Pb		corr.	^{207}Pb		^{207}Pb		^{206}Pb	
Sample	U	$x10^{-13}$ mol	$^{206}Pb^*$	Pb_c	(pg)	^{204}Pb	^{206}Pb	^{206}Pb	% err	^{235}U	% err	^{238}U	% err	coef.	^{206}Pb	±	^{235}U	±	^{238}U	±
(a)	(b)	(c)	(c)	(c)	(c)	(d)	(e)	(e)	(f)	(e)	(f)	(e)	(f)		(g)	(f)	(g)	(f)	(g)	(f)
99-1A																				
a2	3.378	31.883	98.24%	29	48.32	987	1.037	0.0672	0.118	1.2951	0.177	0.1398	0.079	0.843	843.95	2.46	843.57	1.01	843.42	0.62
a3	4.029	3.309	96.39%	15	10.50	481	1.234	0.0677	0.230	1.3405	0.279	0.1436	0.094	0.648	859.60	4.77	863.44	1.62	864.93	0.76
a4	3.787	13.872	99.04%	56	11.38	1811	1.163	0.0672	0.085	1.2968	0.150	0.1399	0.071	0.952	844.26	1.78	844.29	0.86	844.31	0.56
a5	3.759	16.470	98.87%	47	16.01	1531	1.157	0.0677	0.097	1.3147	0.158	0.1409	0.073	0.904	858.88	2.02	852.21	0.91	849.64	0.58
99-3A																				
a4	3.427	38.269	98.63%	37	45.52	1243	1.050	0.0686	0.077	1.3941	0.116	0.1474	0.059	0.807	886.95	1.59	886.45	0.69	886.25	0.49
a5	3.515	35.599	98.67%	39	40.95	1285	1.077	0.0687	0.077	1.4016	0.119	0.1479	0.065	0.808	890.77	1.58	889.61	0.71	889.15	0.54
a6	3.439	23.942	98.71%	39	26.80	1320	1.055	0.0688	0.076	1.4004	0.116	0.1477	0.058	0.812	891.73	1.57	889.11	0.68	888.06	0.48
a7	3.886	14.774	98.42%	33	20.25	1082	1.084	0.0683	0.116	1.8121	0.176	0.1925	0.080	0.852	877.14	2.39	1049.85	1.15	1134.78	0.84
a8	3.664	37.956	98.49%	35	49.82	1128	1.124	0.0686	0.082	1.3923	0.120	0.1471	0.061	0.782	887.55	1.69	885.69	0.71	884.95	0.50
99-5A																				
a1	14.863	2.639	97.63%	59	5.45	725	4.814	0.0675	0.181	1.0944	0.237	0.1176	0.090	0.739	853.25	3.76	750.65	1.26	716.69	0.61
a2	10.960	3.703	98.84%	90	3.68	1492	3.221	0.0672	0.129	1.4838	0.186	0.1602	0.076	0.843	843.08	2.68	923.78	1.13	957.94	0.68
a3	11.083	4.709	98.93%	103	4.32	1615	3.505	0.0670	0.112	1.1622	0.171	0.1258	0.073	0.880	838.53	2.34	782.98	0.93	763.63	0.53
99-6C																				
a1	6.609	1.700	97.38%	28	3.88	658	2.052	0.0673	0.282	1.2544	0.403	0.1352	0.244	0.724	846.37	5.87	825.37	2.28	817.60	1.87
a2	5.692	0.762	97.08%	23	1.94	596	1.758	0.0671	0.414	1.2653	0.473	0.1367	0.110	0.623	841.08	8.61	830.27	2.68	826.23	0.86
a3	7.228	16.296	99.23%	104	10.72	2235	2.230	0.0671	0.085	1.2706	0.148	0.1373	0.072	0.933	841.56	1.77	832.65	0.84	829.32	0.56
a4	8.105	3.776	98.12%	45	6.16	913	2.491	0.0678	0.145	1.3298	0.204	0.1422	0.085	0.800	862.67	3.01	858.81	1.18	857.32	0.68
a5	5.033	8.567	99.45%	115	4.03	3129	1.552	0.0666	0.091	1.2421	0.151	0.1352	0.073	0.904	825.91	1.90	819.85	0.85	817.61	0.56
									Titanite											
99-2B																				
t1	1.771	119.931	99.90%	385	10.39	16875	0.540	0.0724	0.042	1.6629	0.097	0.1666	0.066	0.939	996.90	0.85	994.49	0.62	993.41	0.61
t2	1.112	153.039	99.80%	171	25.95	8620	0.336	0.0721	0.043	1.6913	0.122	0.1701	0.098	0.945	989.39	0.88	1005.27	0.78	1012.57	0.92
t3	1.006	71.539	99.86%	232	8.78	11920	0.305	0.0722	0.043	1.6720	0.093	0.1680	0.059	0.939	991.60	0.87	997.96	0.59	1000.86	0.54
t4	1.063	56.005	99.73%	124	12.94	6337	0.320	0.0720	0.045	1.7045	0.093	0.1716	0.055	0.938	986.62	0.92	1010.20	0.59	1021.12	0.52
t6	1.227	37.483	99.63%	94	11.84	4639	0.366	0.0719	0.073	1.7393	0.136	0.1753	0.071	0.947	984.26	1.49	1023.19	0.88	1041.48	0.68
99-5A																				
t1	3.402	6.155	99.36%	80	3.38	2689	1.038	0.0717	0.092	1.6121	0.152	0.1631	0.072	0.914	976.78	1.87	974.91	0.96	974.08	0.65
t2	4.029	8.983	99.67%	170	2.51	5277	1.229	0.0716	0.073	1.6094	0.137	0.1630	0.069	0.963	974.64	1.49	973.88	0.86	973.55	0.62
t3	4.144	4.533	98.74%	45	4.92	1365	1.265	0.0711	0.119	1.5735	0.178	0.1604	0.076	0.859	961.08	2.44	959.80	1.10	959.25	0.67
t4	3.996	9.434	98.58%	39	11.57	1208	1.226	0.0711	0.112	1.5513	0.171	0.1582	0.077	0.864	961.32	2.28	951.01	1.06	946.56	0.68
t5	4.029	15.156	99.79%	274	2.64	8463	1.228	0.0716	0.070	1.6124	0.133	0.1633	0.070	0.956	975.51	1.42	975.04	0.84	974.84	0.63
99-6C																				
t1	3.489	37.423	99.57%	121	13.67	4010	1.062	0.0733	0.050	1.7302	0.096	0.1712	0.056	0.921	1021.64	1.01	1019.83	0.62	1018.98	0.53
t2	3.717	80.708	99.80%	262	14.06	8386	1.131	0.0738	0.044	1.7664	0.095	0.1737	0.061	0.934	1035.33	0.89	1033.22	0.62	1032.22	0.58
t3	3.421	37.719	99.48%	98	16.88	3275	1.041	0.0731	0.051	1.7180	0.099	0.1705	0.058	0.914	1015.88	1.04	1015.27	0.63	1014.99	0.54
t4	3.249	49.975	98.91%	45	47.10	1563	0.982	0.0724	0.069	1.7041	0.115	0.1708	0.067	0.840	996.09	1.40	1010.06	0.73	1016.51	0.63
t5	3.478	27.801	97.75%	22	54.74	757	1.057	0.0728	0.101	1.7078	0.135	0.1700	0.067	0.689	1009.52	2.05	1011.46	0.86	1012.35	0.62

Table 3-10: (a) a1, a2, etc. are labels for analyses composed of single apatite grains or fragments of grains, labels with letters are fragments from the same grain. t1, t2, etc. are labels for analyses composed of single titanite grains or fragments of grains. (b) Model Th/U ratio calculated from radiogenic 208Pb/206Pb ratio and 207Pb/235U date. (c) Pb* and Pbc are radiogenic and common Pb, respectively. mol % ^{206}Pb* is with respect to radiogenic and blank Pb. (d) Measured ratio corrected for spike and fractionation only. Fractionation correction is 0.15 ± 0.03 (1 sigma) %/amu (atomic mass unit) for single-collector. Daly analyses, based on analysis of EARTHTIME 202Pb-205Pb tracer solution. Fractionation correction is 0.10 ± 0.02 (1 sigma) %/amu (atomic mass unit) for multi-collector Faraday-Daly analyses, based on analysis of EARTHTIME 202Pb-205Pb tracer solution. (e) Corrected for fractionation, spike, common Pb, and initial disequilibrium in 230Th/238U. Procedural Pb blank is assumed to be 1.0 pg with composition of 206Pb/204Pb = 18.35 ± 1.50%; 207Pb/204Pb = 15.60 ± 0.75%; 208Pb/204Pb = 38.08 ± 1.00% (1 sigma). The remainder of the common Pb is assigned to the titanite or apatite with a composition determined by Stacey and Kramers (1975). 206Pb/238U and 207Pb/206Pb ratios corrected for initial disequilibrium in 230Th/238U using Th/U [magma] = 3. (f) Errors are 2 sigma, propagated using algorithms of Schmitz and Schoene (2007) and Crowley et al. (2007). (g) Calculations based on the decay constants of Jaffey et al. (1971). 206Pb/238U and 207Pb/206Pb dates corrected for initial disequilibrium in 230Th/238U using Th/U [magma] = 3.

3.6.3 Zircon

Valley et al. (2009; 2011) reported host granite and ore zircon ages from the LMG and associated rocks. Dates for the samples associated with this study are given above in the sample descriptions. According to Valley et al. (2009; 2011), the host-rock zircon rims are interpreted to represent emplacement ages. However, these same zircon crystals in all samples investigated also contain cores distinguishable in BSE imaging. In order to test the possibility that the zircon cores record crystallization age, whereas zircon rims represent later growth due to either metamorphism or other fluid-related growth, a study targeting the LMG host rock zircon cores was done on 4 samples, with 100 individual zircon grains in total analysed, in order to evaluate the age distribution of older cores. Of

these samples the majority contained older cores with the exception of sample 99-2B.

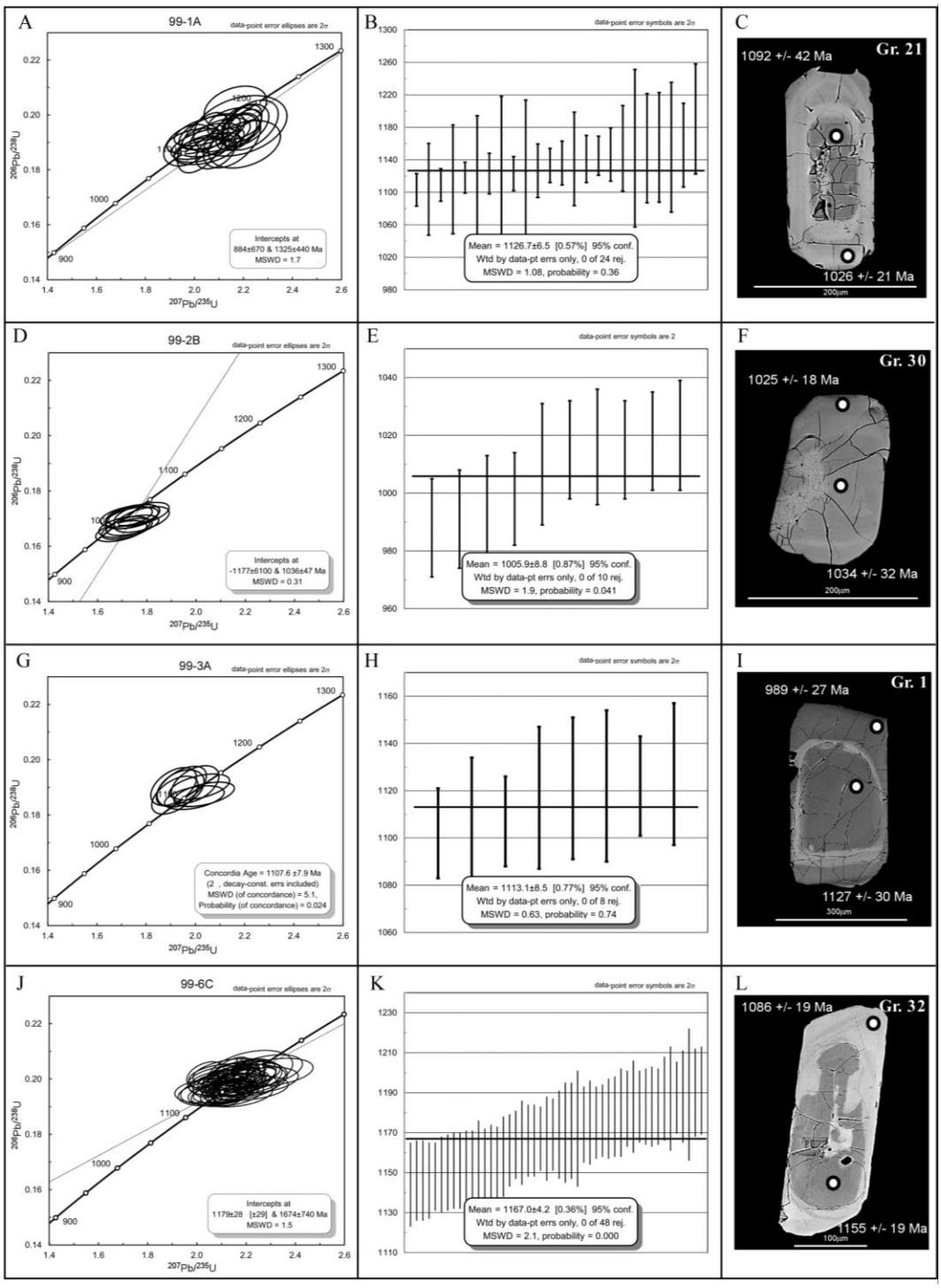

Figure 3-12: LA-ICPMS U-Pb geochronology from LMG host rock zircon cores. A) Concordia plots for 99-1A cores. B) $^{206}Pb/^{238}U$ weighted mean plot for 99-1A, with a weighted mean core

age of 1126.7 ± 6.5 Ma (2σ). C) Corresponding representative BSE image of 99-1A zircon and LA-ICPMS spot analysis with $^{206}Pb/^{238}U$ ages. D) Concordia plots for 99-2B cores. E) $^{206}Pb/^{238}U$ weighted mean plot for 99-2B, with a weighted mean core age of 1005.9 ± 8.8 Ma (2σ). F) Corresponding representative BSE image of 99-2B zircon and LA-ICPMS spot analysis with $^{206}Pb/^{238}U$ ages. G) Concordia plots for 99-3A cores. H) $^{206}Pb/^{238}U$ weighted mean plot for 99-3A, with a weighted mean core age of 1113.1 ± 8.5 Ma (2σ). I) Corresponding representative BSE image of 99-3A zircon and LA-ICPMS spot analysis with $^{206}Pb/^{238}U$ ages. J) Concordia plots for 99-6C cores. K) Weighted mean plot for 99-6C, with a weighted mean core age of 1167.0 ± 4.2 Ma (2σ) L) Corresponding representative BSE image of 99-6C zircon and LA-ICPMS spot analysis with $^{206}Pb/^{238}U$ ages.

Selected zircon cores from host LMG rock samples were dated by LA-ICPMS (Fig.3-12a-l, Table 3-11). In sample 99-1A a representative BSE image demonstrates a fractured core clearly visible against the rim that is lighter in BSE ($^{206}Pb/^{238}U$ rim ages ~ 1062-1002 Ma) (Fig. 3-12c). The cores plot along Concordia (Fig. 3-12a) and have weighted mean ages of 1126.7 ± 6.5 Ma (Fig. 3-12b). 99-2B BSE image demonstrates alteration along the fractures (Fig. 3-12f). In this image the core is also fractured and is slightly darker in BSE compared to the rim ($^{206}Pb/^{238}U$ rim ages of ~1025-978 Ma). The cores plot along Concordia (Fig. 3-12d) and have weighted mean core ages of 1005.9 ± 8.8 Ma (2 σ) (Fig. 3-12e). This sample likely constrains the age of the pervasive Na-alteration of the LMG and is similar in age to the ore zircons reported by Valley et al. (2009). A representative BSE image for sample 99-3A shows a distinct darker core surrounded by an inner lighter rim and a darker outer rim ($^{206}Pb/^{238}U$ rim ages of ~1102-913 Ma) (Fig. 3-12i). Zircon from 99-3A also tended to be larger compared to the other LMG samples dated and yields a weighted mean core age of 1113.1± 8.5 Ma (2 σ) (Fig, 3-12h). Zircon from sample 99-6C typically has obvious darker and often fractured cores with lighter rim in BSE ($^{206}Pb/^{238}U$ rim ages of ~1090-990 Ma) (Fig. 3-12l). The data

tend plot along Concordia (Fig. 3-12j) and have weighted mean core ages of 1167.0 ± 4.2 Ma (2 σ) (Fig. 3-12k).

Table 3-11. Zircon LA-ICPMS U-Th-Pb isotope data from LMG host rock zircon cores and rims

Measured Isotopic ratios								Calculated Ages						
Sample	Grain	Zone	$^{207}Pb/^{235}U$	2s	$^{206}Pb/^{238}U$	2s	RHO	$^{207}Pb/^{235}U$ age	2s	$^{206}Pb/^{238}U$ age	2s	$^{207}Pb/^{206}Pb$ age	2s	Th/U
99-1A	1.1	Core	2.0720	0.1100	0.1939	0.0054	0.5379	1155	48	1141	29	1140	35	0.0307
99-1A	3.1	Core	2.0400	0.1000	0.1866	0.0038	0.4097	1175	39	1103	20	1126	34	0.0302
99-1A	5.1	Core	2.0650	0.1000	0.1892	0.0036	0.5183	1181	30	1118	19	1137	33	0.0290
99-1A	5.3	Core	2.1050	0.1000	0.1927	0.0051	0.5065	1184	46	1136	27	1147	34	0.0296
99-1A	12.2	Core	2.0520	0.1100	0.1943	0.0046	0.5606	1119	41	1145	24	1131	34	0.0301
99-1A	15.2	Core	2.0290	0.0920	0.1874	0.0038	0.4514	1169	37	1109	20	1128	32	0.0284
99-1A	20.1	Core	2.0650	0.0940	0.1923	0.0039	0.5352	1107	37	1133	21	1133	33	0.0291
99-1A	21.1	Core	2.0030	0.0950	0.1905	0.0038	0.3990	1092	42	1123	21	1118	34	0.0304
99-1A	29.1	Core	2.0390	0.1100	0.1896	0.0047	0.5688	1146	41	1123	25	1126	35	0.0311
99-1A	A32	Core	1.9754	0.0824	0.1890	0.0062	0.3917	1107	56	1116	67	1034	26	0.2677
99-1A	A12	Core	2.0344	0.0848	0.1899	0.0090	0.5663	1127	57	1121	97	1042	13	0.1044
99-1A	A20	Core	2.0877	0.0669	0.1867	0.0052	0.4336	1145	44	1104	56	1151	21	0.2192
99-1A	A11	Core	2.1527	0.0959	0.1907	0.0081	0.4793	1166	62	1125	88	1122	30	0.4832
99-1A	A07	Core	2.1637	0.0902	0.1968	0.0048	0.2914	1169	58	1158	51	1219	36	0.3233
99-1A	A18	Core	2.1644	0.0313	0.1909	0.0030	0.5524	1170	20	1127	33	1119	13	0.3559
99-1A	A27	Core	2.1672	0.1042	0.2028	0.0063	0.3240	1171	67	1190	68	1169	30	0.1656
99-1A	A44	Core	2.1712	0.0682	0.1936	0.0053	0.4379	1172	44	1141	58	1154	19	0.2660
99-1A	A42	Core	2.1869	0.1559	0.1961	0.0090	0.3218	1177	99	1154	97	1190	52	0.2244
99-1A	A34	Core	2.1944	0.0658	0.1961	0.0062	0.5296	1179	42	1154	67	1131	16	0.5580
99-1A	A39	Core	2.1997	0.0849	0.1963	0.0063	0.4134	1181	54	1155	68	1152	28	0.2841
99-1A	A19	Core	2.2033	0.0571	0.1960	0.0049	0.4811	1182	36	1154	53	1148	11	0.3071
99-1A	A29	Core	2.2041	0.1200	0.1893	0.0071	0.3426	1182	76	1118	77	1258	43	0.3842
99-1A	A40	Core	2.2234	0.0369	0.1946	0.0030	0.4682	1188	23	1146	33	1147	18	0.3724
99-1A	A41	Core	2.2260	0.0949	0.1963	0.0074	0.4431	1189	60	1155	80	1171	25	0.3433
99-1A	3.2	Rim	1.8770	0.0930	0.1819	0.0039	0.4970	1070	32	1076	21	1062	36	0.1340
99-1A	5.2	Rim	1.7620	0.0850	0.1706	0.0032	0.5551	1029	31	1016	18	1064	28	0.1410
99-1A	15.1	Rim	1.7730	0.0780	0.1736	0.0033	0.5377	1032.8	30	1032	18	1052	29	0.1495
99-1A	20.2	Rim	1.7890	0.0890	0.1784	0.0054	0.5533	1039	33	1056	29	1018	54	0.0615
99-1A	21.2	Rim	1.7510	0.0830	0.1727	0.0039	0.6072	1026	31	1026	21	1030	34	0.2498
99-1A	27.2	Rim	1.7650	0.0900	0.1744	0.0044	0.5410	1031	34	1036	24	1024	46	0.1360
99-1A	29.2	Rim	1.8540	0.0950	0.1807	0.0047	0.6011	1064	34	1074	26	1077	40	0.0710
99-1A	1.2	Rim	1.7870	0.0890	0.1758	0.0033	0.5443	1040.8	31	1043	18	1045	27	0.1899
99-1A	12.1	Rim	1.7190	0.0880	0.1681	0.0032	0.5326	1014	31	1002	17	1026	30	0.1506
99-2B	2.2	Core	1.7190	0.0840	0.1663	0.0031	0.5532	1087	28	991	17	1017	31	0.0305
99-2B	8.1	Core	1.7790	0.0910	0.1716	0.0035	0.5539	1080	33	1020	19	1033	33	0.0319
99-2B	8.2	Core	1.7090	0.0850	0.1670	0.0031	0.4289	1036	31	996	17	1009	31	0.0307
99-2B	23.1	Core	1.7400	0.0870	0.1703	0.0032	0.4657	1034	31	1015	17	1023	31	0.0303
99-2B	24.1	Core	1.7420	0.0870	0.1676	0.0030	0.5150	1076	29	998	16	1021	32	0.0313
99-2B	25.2	Core	1.6960	0.0850	0.1655	0.0031	0.5181	1056	31	988	17	1005	31	0.0308
99-2B	27.1	Core	1.7410	0.0900	0.1707	0.0036	0.5236	1042	36	1016	20	1020	33	0.0324
99-2B	27.2	Core	1.7170	0.0860	0.1708	0.0031	0.4629	1011	29	1015	17	1013	31	0.0306

Measured Isotopic ratios								Calculated Ages						
Sample	Grain	Zone	$^{207}Pb/^{235}U$	2s	$^{206}Pb/^{238}U$	2s	RHO	$^{207}Pb/^{235}U$ age	2s	$^{206}Pb/^{238}U$ age	2s	$^{207}Pb/^{206}Pb$ age	2s	Th/U
99-2B	29.2	Core	1.7450	0.0880	0.1713	0.0031	0.4311	1045	29	1018	17	1027	30	0.0292
99-2B	30.1	Core	1.7800	0.0910	0.1697	0.0038	0.5420	1094	36	1010	21	1034	32	0.0309
99-2B	23.2	Rim	1.7280	0.0870	0.1639	0.0032	0.5286	1014	31	978	18	1083	30	0.1581
99-2B	24.2	Rim	1.7440	0.0880	0.1698	0.0031	0.4517	1024	32	1012	17	1048	32	0.1535
99-2B	25.1	Rim	1.6920	0.0860	0.1660	0.0032	0.5272	1005	31	990	17	1038	30	0.2025
99-2B	29.1	Rim	1.7430	0.0890	0.1708	0.0031	0.4815	1022	31	1016	17	1032	29	0.1310
99-2B	30.2	Rim	1.7530	0.0870	0.1724	0.0033	0.5489	1026.2	31	1025	18	1028	29	0.1844
99-3A	1.1	Core	1.9990	0.0790	0.1911	0.0055	0.4455	1096	38	1127	30	1113	26	0.0234
99-3A	5.1	Core	1.9170	0.0770	0.1872	0.0056	0.5198	1067	39	1104	30	1085	27	0.0249
99-3A	10.1	Core	1.9400	0.0780	0.1896	0.0055	0.3714	1084	43	1117	30	1096	26	0.0237
99-3A	11.1	Core	1.9430	0.0830	0.1904	0.0059	0.5445	1086	45	1122	32	1091	28	0.0257
99-3A	16.2	Core	1.9120	0.0760	0.1903	0.0056	0.4642	1020	39	1121	30	1083	27	0.0249
99-3A	30.1	Core	2.0360	0.1000	0.1875	0.0036	0.4992	1177	34	1107	19	1126	33	0.0293
99-3A	34.2	Core	1.9960	0.0990	0.1863	0.0035	0.4459	1154	33	1102	19	1117	33	0.0295
99-3A	35.1	Core	2.0170	0.1000	0.1902	0.0038	0.4757	1128	40	1122	21	1118	34	0.0304
99-3A	1.2	Rim	1.6370	0.0650	0.1658	0.0048	0.4704	985	25	989	27	958	36	0.0800
99-3A	5.2	Rim	1.4810	0.0580	0.1524	0.0046	0.4925	925	24	913	26	942	37	0.0626
99-3A	10.2	Rim	1.9350	0.0830	0.1868	0.0063	0.5558	1094	30	1102	34	1079	47	0.2122
99-3A	11.1	Rim	1.6870	0.0640	0.1698	0.0049	0.6096	1001.9	24	1010	27	986	30	0.0559
99-3A	16.1	Rim	1.6530	0.0670	0.1716	0.0051	0.3997	987	26	1019	28	946	42	0.0944
99-3A	30.2	Rim	1.7050	0.0840	0.1690	0.0032	0.4054	1012	31	1006	17	1044	36	0.1003
99-3A	35.2	Rim	1.7260	0.0880	0.1747	0.0036	0.4191	1015	32	1040	19	986	42	0.0963
99-6C	1b	Core	2.2180	0.1400	0.2029	0.0061	0.3478	1192	45	1189	33	1126	134	0.2514
99-6C	2a	Core	2.1040	0.1100	0.1982	0.0033	0.3689	1148	37	1166	18	1121	117	0.4732
99-6C	5a	Core	2.1420	0.1100	0.1985	0.0029	0.5040	1163	34	1167	16	1154	112	0.4603
99-6C	5b	Core	2.1860	0.1100	0.2001	0.0034	0.6079	1176	35	1176	18	1170	110	0.4066
99-6C	8b	Core	2.1200	0.1100	0.1953	0.0032	0.4377	1152	37	1148	17	1167	113	0.4166
99-6C	8c	Core	2.0810	0.1200	0.1961	0.0043	0.3802	1141	40	1153	23	1090	127	0.3018
99-6C	9b	Core	2.1240	0.1200	0.1947	0.0038	0.3492	1156	39	1146	20	1162	119	0.2654
99-6C	14a	Core	2.1750	0.1200	0.2007	0.0037	0.3924	1170	37	1178	20	1144	117	0.3568
99-6C	24b	Core	2.1230	0.1200	0.1993	0.0034	0.2828	1144	40	1169	18	1103	123	0.3954
99-6C	28a	Core	2.1310	0.1200	0.2027	0.0039	0.4297	1149	39	1187	21	1087	119	0.4101
99-6C	28b	Core	2.1610	0.1200	0.1946	0.0038	0.3005	1167	39	1144	21	1197	121	0.4320
99-6C	31a	Core	2.0990	0.1100	0.1950	0.0035	0.3844	1147	37	1150	19	1149	117	0.3014
99-6C	32a	Core	2.2120	0.1300	0.1967	0.0036	0.3089	1186	40	1155	19	1195	121	0.2866
99-6C	33b	Core	2.1500	0.1200	0.1989	0.0040	0.2789	1157	40	1167	21	1182	122	0.4776
99-6C	34a	Core	2.0710	0.1200	0.1948	0.0037	0.2506	1141	38	1146	20	1129	124	0.4209
99-6C	37b	Core	2.1140	0.1200	0.2006	0.0040	0.2175	1151	39	1180	22	1132	123	0.4571
99-6C	38a	Core	2.2530	0.1300	0.1996	0.0039	0.3205	1188	42	1175	21	1224	124	0.3776
99-6C	38b	Core	2.1220	0.1300	0.1992	0.0046	0.2279	1153	43	1170	25	1124	132	0.4742
99-6C	42a	Core	2.0450	0.1100	0.1958	0.0036	0.2408	1133	37	1151	19	1142	120	0.3179
99-6C	43a	Core	2.3130	0.1300	0.2025	0.0041	0.3369	1216	40	1190	22	1269	118	0.5866

Measured Isotopic ratios								Calculated Ages						
								$^{207}Pb/^{235}U$		$^{206}Pb/^{238}U$		$^{207}Pb/^{206}Pb$		Th/U
Sample	Grain	Zone	$^{207}Pb/^{235}U$	2s	$^{206}Pb/^{238}U$	2s	RHO	age	2s	age	2s	age	2s	
99-6C	44a	Core	2.2700	0.1300	0.2028	0.0049	0.4557	1189	42	1187	26	1207	120	0.4674
99-6C	44b	Core	2.1910	0.1200	0.2018	0.0042	0.3599	1176	39	1183	23	1160	121	0.3377
99-6C	48a	Core	2.1960	0.1400	0.2000	0.0053	0.2550	1178	46	1172	29	1197	138	0.4234
99-6C	48b	Core	2.2010	0.1300	0.1997	0.0044	0.3472	1174	41	1171	24	1199	123	0.4504
99-6C	59a	Core	2.1810	0.1200	0.1971	0.0038	0.3400	1172	39	1158	20	1204	118	0.3420
99-6C	60a	Core	2.1400	0.0580	0.2016	0.0034	0.2400	1161	19	1183	18	1147	33	0.3058
99-6C	64b	Core	2.0530	0.0570	0.1974	0.0033	0.2167	1132	19	1161	18	1074	35	0.4545
99-6C	65b	Core	2.1620	0.0570	0.1980	0.0033	0.4315	1169	18	1164	17	1160	28	0.4989
99-6C	67a	Core	2.1620	0.0650	0.2004	0.0036	0.1580	1171	21	1177	20	1162	43	0.5232
99-6C	69a	Core	2.1240	0.0640	0.1946	0.0035	0.2690	1156	21	1146	19	1160	40	0.2664
99-6C	69b	Core	2.2350	0.0710	0.2020	0.0043	0.2540	1192	22	1188	23	1197	52	0.2705
99-6C	69c	Core	2.1450	0.0650	0.1956	0.0035	0.3329	1164	21	1151	19	1197	39	0.2442
99-6C	71f	Core	2.1040	0.0560	0.1953	0.0035	0.4182	1148	18	1149	19	1144	31	0.3534
99-6C	77a	Core	2.1480	0.0610	0.1981	0.0034	0.3536	1165	20	1166	18	1167	35	0.3552
99-6C	81a	Core	2.1780	0.0640	0.2014	0.0035	0.2656	1175	20	1182	19	1149	41	0.5055
99-6C	84a	Core	2.2710	0.0610	0.2015	0.0035	0.2760	1203	19	1183	19	1236	29	0.4031
99-6C	85a	Core	2.2170	0.0540	0.2024	0.0033	0.5515	1187	17	1188	18	1175	20	0.4349
99-6C	88a	Core	2.0350	0.0620	0.2016	0.0038	0.3922	1128	20	1183	20	1050	38	0.4624
99-6C	99	Core	2.1310	0.0590	0.1958	0.0036	0.3947	1159	19	1152	19	1157	33	0.4166
99-6C	107	Core	2.1600	0.0590	0.1962	0.0033	0.2690	1170	18	1155	18	1199	34	0.3713
99-6C	114	Core	2.1580	0.0610	0.1997	0.0035	0.3217	1166	19	1174	19	1165	35	0.4042
99-6C	115	Core	2.1390	0.0640	0.2029	0.0041	0.5525	1160	20	1191	22	1124	31	0.3691
99-6C	118	Core	2.2000	0.0620	0.2015	0.0035	0.3134	1182	20	1183	19	1162	35	0.3784
99-6C	103b	Core	2.1410	0.0590	0.1956	0.0036	0.4676	1161	19	1152	19	1185	32	0.3900
99-6C	108b	Core	2.1750	0.0730	0.1989	0.0042	0.3672	1170	23	1169	22	1177	47	0.5563
99-6C	110a	Core	2.1030	0.0640	0.1960	0.0036	0.3150	1150	21	1153	19	1147	41	0.2938
99-6C	112a	Core	2.1450	0.0550	0.2000	0.0034	0.5437	1162	18	1175	18	1151	24	0.4595
99-6C	123b	Core	2.0950	0.0640	0.1984	0.0039	0.4941	1150	21	1165	21	1147	41	0.4114
99-6C	81b	Rim	1.7000	0.0420	0.1661	0.0028	0.4170	1009	15	990	15	1049	23	0.0913
99-6C	81c	Rim	1.8670	0.0460	0.1758	0.0030	0.5760	1070	16	1045	16	1122	21	0.1014
99-6C	65a	Rim	1.7810	0.0430	0.1733	0.0027	0.3630	1039	16	1030	15	1036	21	0.1142
99-6C	71a	Rim	1.7580	0.0420	0.1741	0.0028	0.4586	1030	15	1035	15	1023	21	0.1524
99-6C	69d	Rim	1.8170	0.0460	0.1742	0.0031	0.5021	1051	16	1036	17	1086	24	0.1214
99-6C	123a	Rim	1.8420	0.0450	0.1759	0.0030	0.4944	1060	16	1044	16	1084	22	0.1485
99-6C	2b	Rim	1.7820	0.0920	0.1764	0.0028	0.4745	1036	33	1046	15	1025	116	0.1503
99-6C	71d	Rim	1.8160	0.0430	0.1763	0.0028	0.5009	1051	16	1047	16	1073	19	0.1456
99-6C	59b	Rim	1.8870	0.0980	0.1794	0.0029	0.4987	1076	34	1062	16	1100	113	0.1998
99-6C	71b	Rim	1.8540	0.0440	0.1793	0.0029	0.5493	1064	16	1064	16	1055	18	0.1741
99-6C	1a	Rim	1.8120	0.0930	0.1796	0.0026	0.5473	1049	33	1065	14	1019	113	0.1981
99-6C	84b	Rim	2.0540	0.0670	0.1798	0.0047	0.5821	1136	21	1067	25	1311	34	0.1702
99-6C	8d	Rim	1.8610	0.0960	0.1802	0.0028	0.4309	1066	34	1068	16	1055	114	0.1185

Measured Isotopic ratios								Calculated Ages						
Sample	Grain	Zone	$^{207}Pb/^{235}U$	2s	$^{206}Pb/^{238}U$	2s	RHO	$^{207}Pb/^{235}U$ age	2s	$^{206}Pb/^{238}U$ age	2s	$^{207}Pb/^{206}Pb$ age	2s	Th/U
99-6C	43b	Rim	1.8730	0.0960	0.1806	0.0029	0.4534	1071	34	1070	16	1052	114	0.1935
99-6C	34b	Rim	1.8550	0.0970	0.1810	0.0031	0.4576	1062	34	1071	17	1052	114	0.2011
99-6C	67b	Rim	1.8890	0.0450	0.1811	0.0029	0.4997	1077	16	1073	16	1067	19	0.1533
99-6C	32d	Rim	1.8170	0.0970	0.1819	0.0032	0.5640	1047	34	1076	18	1025	116	0.2253
99-6C	77b	Rim	1.8950	0.0470	0.1816	0.0030	0.5483	1079	17	1076	17	1081	23	0.1642
99-6C	64a	Rim	1.9010	0.0460	0.1823	0.0029	0.3180	1080	16	1079	16	1074	21	0.1482
99-6C	67c	Rim	1.8720	0.0500	0.1823	0.0032	0.5543	1071	18	1079	18	1045	27	0.1465
99-6C	31b	Rim	1.8670	0.0970	0.1826	0.0030	0.4176	1069	34	1080	16	1014	114	0.2362
99-6C	88b	Rim	1.8930	0.0460	0.1824	0.0030	0.4744	1077	16	1081	16	1059	22	0.1501
99-6C	8e	Rim	1.9010	0.1000	0.1830	0.0033	0.5095	1080	34	1082	18	1060	116	0.1749
99-6C	108c	Rim	1.9030	0.0470	0.1828	0.0030	0.4400	1082	16	1083	16	1088	22	0.2387
99-6C	32c	Rim	1.8400	0.0960	0.1839	0.0034	0.4953	1058	34	1086	19	1003	115	0.2699
99-6C	33c	Rim	1.8620	0.0980	0.1837	0.0034	0.5700	1067	34	1087	19	1060	113	0.2696
99-6C	71c	Rim	1.9060	0.0480	0.1843	0.0030	0.4756	1081	17	1090	17	1067	22	0.1904

3.7 Radiogenic Isotopes

3.7.1 Sm-Nd isotopes

Sm and Nd isotopes were measured on individual apatite and titanite grains in order to determine isochron ages and for ε_{Nd} calculations. The ε_{Nd} was used to constrain the REE source for the apatite and titanite, e.g. mantle, crustal, or some combination of these two. Sm-Nd isotopes show a distinctly younger apatite Sm-Nd isochron age (Fig. 3-13a-b), compared to the U-Pb zircon age (~1060 Ma) from the host-rock and ore (~1000 Ma). The widest spread of Sm/Nd came from AH-06-6B (ore apatite) which yields an isochron age of 857 ± 23 Ma with an MSWD of 1.6. The best fit for the LMG host rock is for 99-5A and yields isochron age of 901 ± 46 Ma (2 σ) with an MSWD of 2.5.

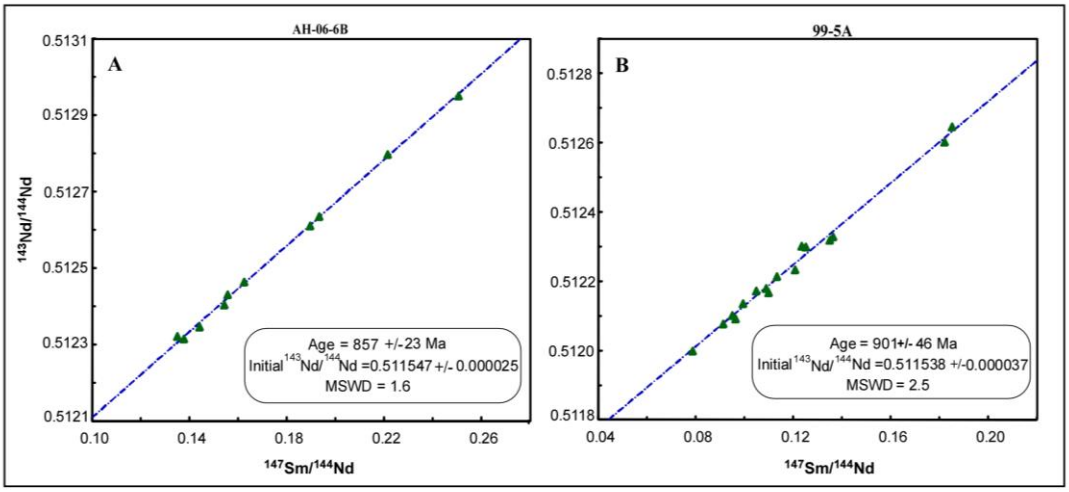

Figure 3-13: Sm-Nd isochron plots for select apatite samples; A) AH-06-6B (ore) with an age of 857 ± 23 Ma and B) 99-5A (host) giving an age 901 ± 46 Ma indicating that the ages of the ore and host apatite are within error of each other and similar to the ID-TIMS apatite ages.

Table 3-12. Sm-Nd isotope data from the LMG titanite and apatite with historic whole-rock Sm-Nd isotope data

Sample	Rock type	147Sm/144Nd	143Nd/144Nd	2SE	Eu/Eu*	Author	ε_{Nd} 1020ma	ε_{Nd} 1060 Ma	ε_{Nd} 1150 Ma
Adirondack Tonalite									
AM87-12	Tonalite	0.11380	0.51212	0.00016	-	Daly and McLelland, 1991	0.77	1.19	2.14
AM86-12	Tonalite	0.10530	0.51207	0.00002	-	Daly and McLelland, 1991	0.86	1.33	2.38
LDT	Tonalite	0.09410	0.51196	0.00002	-	Daly and McLelland, 1991	0.16	0.68	1.86
AMCG Granitoids									
DIA	Syenite	0.12640	0.51222	0.00002	-	Daly and McLelland, 1991	1.09	1.45	2.26
AM86-15	Rapakivi granite	0.12820	0.51220	0.00002	-	Daly and McLelland, 1991	0.47	0.81	1.60
AC85-6	Mangerite	0.12310	0.51224	0.00001	-	Daly and McLelland, 1991	1.92	2.29	3.14
AM86-17	Charnokite	0.11570	0.51212	0.00002	-	Daly and McLelland, 1991	0.44	0.85	1.78
AM86-9	Granite	0.12030	0.51222	0.00002	-	Daly and McLelland, 1991	1.79	2.18	3.06
Younger Granitoids									
AM86-6	Granodiorite	0.12030	0.51224	0.00001	-	Daly and McLelland, 1991	2.18	2.57	3.45
AM86-4	Alaskite	0.14200	0.51230	0.00001	-	Daly and McLelland, 1991	0.56	0.83	1.46
SK2A	Trondhjemite	0.12550	0.51227	0.00002	-	Daly and McLelland, 1991	2.19	2.55	3.37
Lyon Mountain Granite Titanite									
99-2B-2.1	Albite Granite	0.10631	0.51212	0.00002	0.43310	Buchanan et al.	1.70	2.16	3.20
99-2B-3.1	Albite Granite	0.10815	0.51211	0.00002	0.43183	Buchanan et al.	1.27	1.73	2.75
99-2B-4.1	Albite Granite	0.11861	0.51218	0.00002	0.49674	Buchanan et al.	1.38	1.78	2.68
99-2B-6.1	Albite Granite	0.12450	0.51228	0.00003	0.51060	Buchanan et al.	2.48	2.85	3.68
99-2B-5.1	Albite Granite	0.11229	0.51218	0.00002	0.42989	Buchanan et al.	2.23	2.66	3.63
99-2B-8.1	Albite Granite	0.11799	0.51219	0.00003	0.50915	Buchanan et al.	1.62	2.03	2.93
99-2B-10.1	Albite Granite	0.12170	0.51223	0.00002	0.50439	Buchanan et al.	1.89	2.27	3.14
99-2B-11.1	Albite Granite	0.12413	0.51225	0.00002	0.50528	Buchanan et al.	1.91	2.28	3.12
99-2B-15.1	Albite Granite	0.12343	0.51224	0.00003	0.50341	Buchanan et al.	1.85	2.22	3.07
99-2B-19a.1-1	Albite Granite	0.12507	0.51226	0.00003	0.50390	Buchanan et al.	2.02	2.38	3.21
99-2B-19a.1-2	Albite Granite	0.12521	0.51227	0.00002	0.50622	Buchanan et al.	2.16	2.53	3.35
99-6c-18.1	Microcline Granite	0.14771	0.51234	0.00003	0.43765	Buchanan et al.	0.69	0.94	1.50
99-6c-17.1	Microcline Granite	0.14100	0.51235	0.00003	0.45564	Buchanan et al.	1.67	1.96	2.59
99-6c-16.1	Microcline Granite	0.14299	0.51233	0.00003	0.41519	Buchanan et al.	1.13	1.40	2.01
99-6c-15.1	Microcline Granite	0.14564	0.51233	0.00002	0.50424	Buchanan et al.	0.79	1.05	1.64
99-6c-13.1	Microcline Granite	0.14137	0.51233	0.00003	0.46780	Buchanan et al.	1.34	1.62	2.25
99-6c-9.1	Microcline Granite	0.14744	0.51238	0.00002	0.36674	Buchanan et al.	1.54	1.79	2.36
99-6c-8.1	Microcline Granite	0.14175	0.51240	0.00005	0.52972	Buchanan et al.	2.67	2.95	3.58
99-6c-6.1	Microcline Granite	0.14644	0.51238	0.00002	0.44348	Buchanan et al.	1.68	1.94	2.51
99-6c-5.1	Microcline Granite	0.14879	0.51238	0.00003	0.54537	Buchanan et al.	1.22	1.46	2.01
99-6c-3.1	Microcline Granite	0.14733	0.51236	0.00002	0.36826	Buchanan et al.	1.15	1.40	1.97
99-5A-8.1	Perthite Granite	0.16643	0.51254	0.00002	0.41287	Buchanan et al.	2.02	2.17	2.51
99-5A-7.1	Perthite Granite	0.17747	0.51250	0.00003	0.54094	Buchanan et al.	-0.10	0.00	0.21
99-5A-4.1	Perthite Granite	0.17958	0.51255	0.00003	0.47082	Buchanan et al.	0.65	0.73	0.92
99-5A-3.1	Perthite Granite	0.19910	0.51264	0.00002	0.43533	Buchanan et al.	-0.17	-0.18	-0.22
99-5A-4.1	Perthite Granite	0.17223	0.51248	0.00003	0.59928	Buchanan et al.	0.12	0.25	0.52
99-5A-21.1	Perthite Granite	0.16286	0.51252	0.00002	0.45160	Buchanan et al.	2.15	2.32	2.71
99-5A-22.1	Perthite Granite	0.17116	0.51256	0.00002	0.42077	Buchanan et al.	1.83	1.96	2.25

Sample	Rock type	147Sm/144Nd	143Nd/144Nd	2SE	Eu/Eu*	Author	ε_{Nd} 1020ma	ε_{Nd} 1060 Ma	ε_{Nd} 1150 Ma
99-5A-33.1	Perthite Granite	0.17166	0.51257	0.00002	0.40235	Buchanan et al.	1.98	2.11	2.39
99-5A-27.1	Perthite Granite	0.16380	0.51256	0.00002	0.41556	Buchanan et al.	2.75	2.92	3.29
99-5A-38.1	Perthite Granite	0.17399	0.51260	0.00003	0.38688	Buchanan et al.	2.29	2.40	2.65
Lyon Mountain Granite Host Apatite									
99-1A-13.1	Perthite Granite	0.11324	0.51218	0.00001	0.31794	Buchanan et al.	1.98	2.41	3.37
99-1A-9.1	Perthite Granite	0.10105	0.51212	0.00002	0.32217	Buchanan et al.	2.43	2.92	4.03
99-1A-14.1	Perthite Granite	0.10346	0.51212	0.00002	0.32015	Buchanan et al.	2.11	2.59	3.67
99-2B-1.1	Albite Granite	0.16500	0.51247	0.00002	0.48274	Buchanan et al.	0.95	1.11	1.47
99-2B-3.1	Albite Granite	0.07969	0.51198	0.00001	0.43164	Buchanan et al.	2.61	3.21	4.56
99-2B-5.1	Albite Granite	0.07495	0.51195	0.00001	0.41676	Buchanan et al.	2.59	3.22	4.62
99-2B-9.1	Albite Granite	0.06946	0.51192	0.00001	0.45048	Buchanan et al.	2.63	3.29	4.76
99-2B-12.1	Albite Granite	0.06709	0.51191	0.00001	0.51947	Buchanan et al.	2.70	3.36	4.86
99-2B-16.1	Albite Granite	0.07311	0.51198	0.00002	0.43559	Buchanan et al.	3.44	4.07	5.50
99-3A-2.1	Fayalite Granite	0.13960	0.51239	0.00001	0.19554	Buchanan et al.	2.64	2.93	3.58
99-3A-4.1	Fayalite Granite	0.13827	0.51238	0.00001	0.19400	Buchanan et al.	2.73	3.03	3.70
99-3A-8.1	Fayalite Granite	0.13609	0.51234	0.00002	0.19166	Buchanan et al.	2.25	2.55	3.25
99-3A-7.1	Fayalite Granite	0.13582	0.51235	0.00001	0.19670	Buchanan et al.	2.43	2.74	3.44
99-3A-10.1	Fayalite Granite	0.13445	0.51235	0.00001	0.19142	Buchanan et al.	2.59	2.91	3.62
99-3A-15.1	Fayalite Granite	0.13499	0.51235	0.00001	0.19702	Buchanan et al.	2.57	2.88	3.59
99-3A-23.1	Fayalite Granite	0.13610	0.51234	0.00002	0.19219	Buchanan et al.	2.19	2.50	3.19
99-5A-20.1	Perthite Granite	0.12058	0.51223	0.00001	0.34830	Buchanan et al.	2.13	2.52	3.40
99-5A-17.1	Perthite Granite	0.09459	0.51210	0.00003	0.51147	Buchanan et al.	2.94	3.46	4.64
99-5A-17.1 rep	Perthite Granite	0.09604	0.51209	0.00002	0.51065	Buchanan et al.	2.57	3.08	4.24
99-5A-27.1	Perthite Granite	0.10954	0.51217	0.00002	0.36939	Buchanan et al.	2.26	2.70	3.71
99-5A-27.1 rep	Perthite Granite	0.10856	0.51218	0.00002	0.36796	Buchanan et al.	2.65	3.10	4.12
99-5A-34.1	Perthite Granite	0.10455	0.51217	0.00004	0.62358	Buchanan et al.	3.04	3.51	4.57
99-5A-34.1 rep	Perthite Granite	0.09931	0.51214	0.00002	0.64417	Buchanan et al.	2.98	3.47	4.60
99-5A-54.1	Perthite Granite	0.07860	0.51200	0.00002	0.75802	Buchanan et al.	3.01	3.62	4.98
99-5A-64.1	Perthite Granite	0.11290	0.51221	0.00001	0.30365	Buchanan et al.	2.76	3.19	4.15
99-5A-73.1	Perthite Granite	0.12319	0.51230	0.00003	0.37181	Buchanan et al.	3.10	3.48	4.32
99-5A-71.1	Perthite Granite	0.18192	0.51260	0.00001	0.36574	Buchanan et al.	1.32	1.40	1.56
99-5A-69.1	Perthite Granite	0.18502	0.51265	0.00002	0.26933	Buchanan et al.	1.75	1.81	1.94
99-5A-41.1	Perthite Granite	0.12506	0.51230	0.00002	0.32525	Buchanan et al.	2.81	3.17	4.00
99-5A-23.1	Perthite Granite	0.13605	0.51233	0.00002	0.39742	Buchanan et al.	1.98	2.29	2.99
99-5A-21.1	Perthite Granite	0.13460	0.51232	0.00002	0.53488	Buchanan et al.	1.95	2.27	2.98
99-5A-39.1	Perthite Granite	0.09116	0.51208	0.00003	0.76112	Buchanan et al.	2.94	3.48	4.70
99-6C-27.1	Microcline Granite	0.09462	0.51201	0.00002	1.85903	Buchanan et al.	1.06	1.58	2.75
99-6C-20.1	Microcline Granite	0.09567	0.51209	0.00004	0.41545	Buchanan et al.	2.67	3.19	4.35
99-6C-17.1	Microcline Granite	0.09430	0.51205	0.00002	0.48292	Buchanan et al.	2.04	2.56	3.74
99-6C-9.1	Microcline Granite	0.08269	0.51197	0.00002	0.62934	Buchanan et al.	1.86	2.44	3.76
99-6C-2.1	Microcline Granite	0.08974	0.51202	0.00002	0.41501	Buchanan et al.	1.99	2.54	3.78
99-6C-4.1	Microcline Granite	0.09995	0.51208	0.00003	0.33565	Buchanan et al.	1.74	2.23	3.35
99-6C-22.1	Microcline Granite	0.09875	0.51208	0.00002	0.34510	Buchanan et al.	2.03	2.53	3.66
99-6C-31.1	Microcline Granite	0.09663	0.51208	0.00004	0.41224	Buchanan et al.	2.28	2.80	3.95
99-6C-22.1	Microcline Granite	0.10722	0.51215	0.00001	0.30673	Buchanan et al.	2.30	2.76	3.79

Sample	Rock type	147Sm/144Nd	143Nd/144Nd	2SE	Eu/Eu*	Author	ε_{Nd} 1020ma	ε_{Nd} 1060 Ma	ε_{Nd} 1150 Ma
99-6C-24.1	Microcline Granite	0.10357	0.51215	0.00001	0.31354	Buchanan et al.	2.62	3.09	4.17
99-6C-17.1	Microcline Granite	0.11393	0.51219	0.00002	0.31657	Buchanan et al.	2.07	2.49	3.44
Lyon Mountain Granite Ore Apatite									
06-4B-15.1	Ore	0.11541	0.51219	0.00002	0.36583	Buchanan et al.	1.88	2.29	3.23
06-4B-2.1	Ore	0.11576	0.51214	0.00003	0.36232	Buchanan et al.	0.94	1.35	2.28
06-4B-4.1	Ore	0.11552	0.51216	0.00002	0.36267	Buchanan et al.	1.31	1.72	2.66
06-4B-22.1	Ore	0.11650	0.51217	0.00001	0.36251	Buchanan et al.	1.50	1.91	2.83
06-4B-34.1	Ore	0.11556	0.51217	0.00002	0.36598	Buchanan et al.	1.45	1.87	2.80
06-4B- 33.1	Ore	0.12104	0.51219	0.00001	0.35165	Buchanan et al.	1.21	1.59	2.46
06-4B- 10.1	Ore	0.11500	0.51215	0.00002	0.36195	Buchanan et al.	1.31	1.72	2.66
06-4B- 12.1	Ore	0.11546	0.51216	0.00003	0.36536	Buchanan et al.	1.28	1.70	2.63
06-4B- 38.1	Ore	0.11579	0.51215	0.00002	0.36454	Buchanan et al.	1.19	1.60	2.53
AH-06-6B-1.1	Ore	0.14393	0.51235	0.00001	0.27140	Buchanan et al.	1.27	1.54	2.14
AH-06-6B-3.1	Ore	0.25019	0.51295	0.00001	0.29016	Buchanan et al.	-0.83	-1.11	-1.74
AH-06-6B-4.1	Ore	0.16227	0.51246	0.00001	0.26516	Buchanan et al.	1.16	1.33	1.73
AH-06-6B-14.1	Ore	0.18923	0.51261	0.00001	0.27293	Buchanan et al.	0.50	0.54	0.62
AH-06-6B-19.1	Ore	0.15414	0.51241	0.00001	0.26991	Buchanan et al.	1.08	1.30	1.78
AH-06-6B-32.1	Ore	0.22125	0.51280	0.00002	0.28396	Buchanan et al.	-0.01	-0.14	-0.44
AH-06-6B-44.1	Ore	0.19311	0.51264	0.00001	0.26453	Buchanan et al.	0.48	0.49	0.53
AH-06-51.1	Ore	0.13467	0.51232	0.00001	0.26615	Buchanan et al.	2.02	2.34	3.05
AH-06-51.1	Ore	0.15527	0.51243	0.00001	0.27999	Buchanan et al.	1.45	1.66	2.13
AH-06-51.1	Ore	0.13735	0.51232	0.00002	0.27156	Buchanan et al.	1.52	1.82	2.50
00-01-25.1	Ore	0.16049	0.51244	0.00002	0.31341	Buchanan et al.	0.88	1.06	1.47
00-01-19.1	Ore	0.16002	0.51244	0.00002	0.31450	Buchanan et al.	0.95	1.14	1.56
00-01-10.1	Ore	0.15092	0.51239	0.00002	0.31465	Buchanan et al.	1.20	1.43	1.95
00-01-2.1	Ore	0.14517	0.51233	0.00002	0.31368	Buchanan et al.	0.84	1.10	1.69
00-01-27.1	Ore	0.15329	0.51239	0.00002	0.31541	Buchanan et al.	0.92	1.14	1.64
00-01-28.1	Ore	0.15592	0.51240	0.00003	0.31186	Buchanan et al.	0.72	0.92	1.39

ε_{Nd} values for titanite and apatite samples from this study and ε_{Nd} values for whole-rock Sm-Nd of the Adirondack Highlands from literature can be found in Table 3-12. ε_{Nd} values were calculated at 1150, 1060 and 1020 Ma Table 3-12 and Figure 3-14. These ages were selected based on the U-Pb apatite and titanite ID-TIMS ages and based on U-Pb LA-ICPMS and SIMS ages of zircon host and ores discussed above. ε_{Nd} was calculated at all of these ages because it is unclear if the formation of apatite and titanite occurred when the LMG formed and the U-Pb isotopes were reset during alteration or if entirely new apatite and titanite formed. The initial ε_{Nd} whole- rock values reported for the Adirondack Highland rocks are plotted as a grey field, in particular the granitoids, overlap with the LMG values. Apatites from samples 99-2B, 99-3A and 99-5A have higher ε_{Nd} indicating greater mantle input compared to other samples or an REE enrichment from the original source.

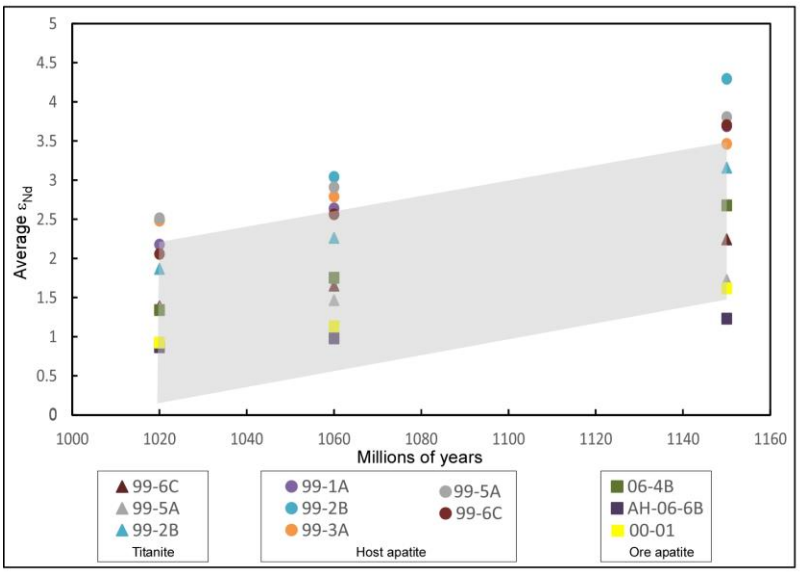

Figure 3-14: Average ε_{Nd} vs. age of the host rock apatite and titanite as well as the ore apatite. Titanite and apatite samples have been plotted at 1150, 1060 and 1020 Ma with a light grey

polygon outlining the ε_{Nd} of the Adirondack Highland granitoids from Daly and McLelland, 1991 at those ages.

Chapter 4. Discussion

4.1 Nature and Role of the LMG Metasomatism and Potential REE Sources

As noted above, in this study we define metasomatism as the process by which compositional changes in the system are driven by hydrothermal fluids that replace, recrystallize, or crystallize new mineral phases. Sodium metasomatism of K-feldspar and plagioclase (i.e., albitization) can be associated with enrichment of HFSE and REE (e.g., Taylor et al., 1981). In particular, albitization of granites is commonly associated with higher concentrations of Fe, U, Th, Zr, Nb, Y and HREE relative to unaltered granite, whereas K-metasomatism is associated with increased Rb, Li and Zn in comparison to unaltered rocks (Kinnaird, 1985). Generally, the fluids responsible for REE enrichment (and concomitant albitization) contain F or Cl, which even in low concentrations can be effective ligands for transporting HFSE and REE (Cathelineau, 1987; Salvi and Williams-Jones, 1996; Willams-Jones et al., 2012).

The REE and HFSE re-mobilization in the LMG is likely related to Na-rich hydrothermal fluids, rather than K-metasomatism. Field relationships and petrography illustrate that Na-alteration was more prominent than K-alteration (Valley et al., 2011), Na-alteration post-dates most potassic metasomatic events; and that most of the ores and REE-rich phases (apatite and titanite) are associated with Na-alteration (albitization) (Valley et al., 2010; 2011) that contributed to their formation. The substantial post-emplacement alteration of the LMG, particularly in the case of Na-altered rocks and to a lesser extent for K-altered rocks is demonstrated in the A-CN-K diagram (Fig. 3-1c). In

Al_2O_3-CaO*+Na_2O+K_2O-FeO+MgO (A-CNK-FM) compositional space, (Fig. 3-1d; Nesbitt and Young, 1989), the LMG host rock samples show Fe addition especially prevalent in the Na-altered samples, suggesting that Na-alteration or metasomatism is the dominant type of alteration type associated with mobilization of Fe and subsequent Fe ore mineralization.

Previous studies, both analytical and experimental, have shown that fluids enriched in Cl and F facilitate the mobilization of Zr, U, and REE (that are commonly referred to as "immobile" elements) in the form of chloride and fluoride complexes. Aqueous complexes of these elements are later deposited due to mixing with Ca-bearing fluids, because fluoride complexes destabilize with Ca due to the insolubility of fluorite (Salvi and Williams-Jones, 1996). In the case of chloride complexes, a decrease in temperature or an increase in pH are required in order to precipitate the REE and HFSE (Willams-Jones et al., 2012). Fluorite is virtually insoluble, such that high F concentrations are precluded in Ca-rich brines. However, F-rich fluids are permitted if Ca concentrations are low (or Ca is immobilized in minerals, rather than in the fluid). The lack of anorthite and the rare Ca bearing major minerals in the LMG samples indicate that Ca is scarce in the LMG hydrothermal system. There is also definitive evidence that F was present in the system, in the form of fluorite in some samples, but also in the elevated F concentrations in the fluorapatite and titanite, which are interpreted to be metasomatic due to their crystallization in Na-alteration zones.

The exact process(es) which caused REE enrichment in the LMG rocks is not clear, and it is possible that several processes (i.e., multiple fluid events) contributed to REE enrichment in these rocks. Is it clear however that the Na-alteration played a more

dominate role in the formation of the REE-rich apatite and titanite as these phases tend to form only in Na-altered areas. U-Pb dates from the LMG indicate that REE enrichment postdates granite emplacement, initial metasomatic alteration, and mineralization, implying a metasomatic or hydrothermal event that was not coeval with the LMG magmatism. The titanite U-Pb dates are similar in age to the ore zircon dates reported by Valley et al. (2009), which supports a younger metasomatic event generally coeval to the Fe mineralization. The source of the REE was likely locally derived from surrounding rocks and minerals. Depletion of REE in feldspar and clinopyroxene in the albitized samples (Fig. 3-8a; Fig. 3-9a) compared to the unaltered or K-metasomatised samples (99-6B, 99-6C) indicates that Na-alteration stripped the minerals of the LMG and associated metasomatized granites of REE and later deposited them as REE-rich apatite and titanite in Na-alteration zones.

4.1.1 Sm-Nd and Lu-Hf isotopes

The in situ Sm-Nd isotopic data from apatite and titanite have calculated initial ε_{Nd} values (Table 3-12) similar to the rocks of the surrounding Adirondacks area (Daly and McLelland, 1991), suggesting that the source of the Sm and Nd was local. The host-rock apatite tends to have slightly higher ε_{Nd} values than both the ore apatite and host rock titanite (Fig. 3-14). This may indicate that the titanite and ore apatite crystallized from a common source, as both are thought to be secondary based on their petrography and association with Na-alteration zones. The host apatite with the highest ε_{Nd} values all

correspond with Na-altered samples, this may reflect fluid alteration and modification of the original Sm-Nd ratio, or that they simply formed from a more juvenile source.

Initial Hf isotope composition of ore zircon, with the exception of older and K-altered 99-4A, have values which are highly radiogenic, with εHf (*t*) greater than +10 and as high as +40 (Valley et al., 2010) indicating that the ore zircon most likely was derived from a REE-rich apatite or clinopyroxene source (i.e., likely an ore/skarn-like body), thus the REE-rich apatite and/or clinopyroxene must have been already emplaced 20-40 m.y. prior in order to accommodate ^{176}Hf growth (Valley et al., 2010).

4.2 Evidence for a Metasomatic or Magmatic Origin of the LMG Host Rocks and Ores

The LMG exhibits A-type or ferroan granite characteristics (Whalen et al., 1987; Frost and Frost, 2011) with Fe-index ranging from 0.92-0.99, K_2O/Na_2O ratios from 0.01-7.78 and 10,000*Ga/Al ratios ranging from 3.35 (99-6C) to 5.75 (99-3A) and high HFSE and REE (Table 3-1). Some of the alkali enrichment can be attributed to the post-emplacement metasomatic alteration caused by hydrothermal fluids (albite granite and microcline granite), although the protolith was likely rich in Fe and alkali elements e.g. sample 99-1A; Table 3-1. Na-metasomatism of such a Fe- and alkali-rich rock may preferentially result in anomalously elevated Fe, HFSE and REE (Kinnaird, 1985). For example, Figure 3-1d shows that Fe is associated with the Na-alteration, whereas Figure 3-8a shows that feldspars in the LMG host rocks are depleted in REE relative to typical igneous rocks.

Iron oxide copper gold and IOA type deposits are known to be associated with alkalic volcanic and plutonic rocks and most occur in an intracratonic extensional environment, i.e., associated with anorogenic granites (Hitzman, 1992). Ferroan magmatism has been associated with other IOCG to IOA-type deposits, like the Fe-Cu-U-Au-REE deposits of the St. Francois Mountains (Pea Ridge, southeast Missouri), which are hosted in A-type or ferroan granitoids (Foose and McLelland, 1995). Other examples of IOCG or IOA ores hosted by or associated with A-type or ferroan granitoids include the world-class Olympic Dam Fe-Cu-U-Au-Ag deposit in South Australia (Hitzman et al., 1992), and the Estrela IOCG deposit and other related IOCG deposits of the Carajas Mineral Province in Brazil (Volp, 2005). These deposits commonly exhibit features that suggest both magmatic and hydrothermal origins for the deposits. Ferroan magmatism may be a critical factor in the formation of these types of deposits and could also explain the extended hydrothermal events in LMG because A-type granites tend to be high temperature and halogen-rich (Collins et al., 1982; Clemens et al., 1986).

The LMG host rocks were heavily K- and Na-metasomatised after their initial crystallization, evidence for which includes whole-rock chemistry with total alkalis up to 10 wt.%, and mineral assemblages consisting entirely of microcline plus quartz (e.g., 99-6C and 99-6B) or albite plus quartz (e.g., 99-2B). In each of these host rocks, ferro-magnesian minerals are essentially absent (99-6C, 99-6B, 99-5A, and 99-1A) apart from disseminated magnetite and rare amphibole. Many of the LMG ores are associated with Na-alteration and the formation of secondary magnetite, apatite, titanite, quartz and zircon (Valley et al., 2011). The ores commonly have alteration halos lacking all ferro-

magnesian minerals, suggesting that the albitizing fluid leached and then subsequently concentrated the Fe from the protolith to the LMG. The LMG is likely a combination of an original magmatic body which was then later hydrothermally altered creating both magmatic and hydrothermal minerals and features in the host-rocks and ores.

4.2.1 Zircon in the LMG host rocks and ores

Valley et al. (2009) concluded that the iron ore mineralization associated with ore zircon growth is probably not directly related to the emplacement of the host granites, and suggested three options for the geologic significance of the dates for the ore zircon grains: 1) post host rock emplacement and metamorphism; 2) Fe oxide-rich magmas intruded as dykes and sills; and 3) hydrothermal origin of the zircon, with mineralizing fluids coming from deeply circulating meteoric waters and/or brines, or younger and as yet unidentified magmatism. Valley et al. (2009) suggested that the latter scenario is most likely option for the ore emplacement which produced zircon; that the zircon and ores are hydrothermal in origin. Evidence of hydrothermal origin for some of the minerals is provided by secondary growth of zircon, apatite and titanite in Na-altered zones commonly with U-Pb ages $\geq$ 20 Ma younger than the host zircon rims.

It is unclear, however, if the younger zircon rims in the host granites (~1060 Ma) represent magmatism, metamorphism, or metasomatism (i.e., recrystallization of pre-existing zircon from the ~1150 Ma granite of the AMCG suite). Many rocks in the Adirondack Highlands exhibit zircon growth from ~1090-1050 Ma (e.g., Chiarenzelli and McLelland, 1993; Alcock et al., 2004; Hamilton et al., 2004), some of which have been

described as uncharacteristic for metamorphic or magmatic zircon and have been suggested to form from recrystallization of a primary zircon during granulite facies metamorphism of the Ottawan orogeny (Chiarenzelli and McLelland, 1993). The host rock zircon rims are generally unzoned in BSE though there may be some "ghost zoning" present (e.g., Fig. 3-2d) and they are remarkably free of mineral, melt, or fluid inclusions. The morphology of the LMG host-rock zircon rims are more akin to that of hydrothermal zircon growth than magmatic zircon indicating that the rims are actually recording an alteration or hydrothermal event rather than a strictly magmatic age.

"Hydrothermal zircon" is a broad term that encompasses various formation mechanisms, including direct precipitation from an aqueous fluid, or re-crystallization in the presence of an aqueous phase (Rubin et al., 1989; Tomaschek at al., 2002; Geisler et al., 2003a and b; Hoskin, 2005; Pettke et al., 2005). Hoskin (2005) distinguished three types of hydrothermal zircon in the Boggy Plain pluton in southeastern Australia: Type 1) formed by the dissolution and reprecipitation in high-pressure, low-temperature meta-igneous rocks (Tomaschek et al., 2002); Type 2) formed by the ion exchange at low temperatures between aqueous fluids and metamict zircon (Geisler et al, 2003a and b); and Type 3) formed by direct precipitation from zircon-saturated aqueous fluid (Hoskin, 2005). In the present study, Type 2 may represent the rims of the host zircon and Type 3 classification may apply to ore zircon that are physically and chemically distinct from zircon in the adjacent host rock (Valley et al., 2009; 2010; 2011).

As described by Geisler et al. (2003a), Type 2 hydrothermal zircon consists of a metamict zircon reacting with aqueous fluids, which changes the composition of the rim,

and potentially the entire zircon if the fluid infiltrates to the core. These recrystallized rims tend to have lower REE, Th and U, as well as brighter in CL and darker in BSE. In the LMG host-rock zircon, the lack of fine-scale growth zoning in the rims, as well as the general lack of inclusions or pores, and obvious fluid alteration pathways (e.g. 99-2B) suggests a hydrothermal origin rather than a magmatic or metamorphic origin of these rims. In addition, zircon rims from samples 99-5A, 99-6B and 99-6C show the opposite trend compared to that described by Geisler et al. (2003a) for Type 2 hydrothermal zircon, with higher U in the rims than the cores, with rims that are darker in CL compared to the cores. Geisler et al. (2003a) noted that the behaviour of U during zircon re-crystallization depends on the composition of the aqueous fluid involved, and in the case of the LMG it is likely that the fluid was enriched in U and the effect of which is uncertain for the LMG zircon rims. A uranium rich fluid could enrich the hydrothermal zircon rims relative to the cores unlike the hydrothermal zircon from Geisler et al. (2003a).

4.2.2 Apatite and titanite in the LMG host rocks and ores

As mentioned above, apatite and titanite trace-element compositions are surprisingly homogenous within individual grains, with little evidence for chemical zoning and few inclusions of any type (i.e., mineral, melt, or fluid). Igneous apatite and titanite normally exhibit growth (and in the case of titanite, sectoral) zoning caused by chemical disequilibrium with the melt during growth (Paterson and Stephens, 1992, Blanc et al., 1993; Dempster et al., 2003), and commonly contain mineral, melt, or fluid inclusions. In several samples (both ore and host) from the LMG, secondary apatite and

titanite are associated with Na-alteration zones, indicating a relationship between their formation and albitization.

Hydrothermal apatite analysed by Blanc et al. (1993) were pink-yellow to pale purple in CL, with mostly irregular zoning. In contrast, magmatic apatites were dominantly yellow in CL and showed both irregular and regular growth zoning. The hydrothermal apatite of Blanc et al. (1993) is similar to the apatite found in the LMG ores and host rocks, showing a wide range of colors in CL (Fig. 1-4). The magmatic apatite reported by Blanc et al. (1993) had higher Mn and Sr and low Si and Y, whereas hydrothermal apatite had very low Mn and Fe and higher Si and Y. Among the LMG samples, most apatite are geochemically similar to the hydrothermal apatite described by Blanc et al. (1993) with the exception in samples 99-6B and 99-6C. Apatite from these samples (99-6B and 99-6C) may be magmatic in origin, or perhaps are less altered (or less enriched in REEs) compared to the other LMG apatites. The apatite from these two (K-metasomatised) samples also have the lowest total lanthanide and Y concentrations among the samples investigated.

The exceptionally high lanthanide and Y in some of the apatite and the association with faults in the area also suggests a potential hydrothermal origin. The hydrothermal fluids that could have formed the apatite (potentially including fluoride or chloride ligands) likely travelled along structurally controlled permeable pathways, such as fault planes on the regional scale, and grain boundaries at the thin-section scale. The three apatite samples with the highest lanthanide and Y abundances in this study (99-3A, 00-01, 99-2B) are each associated with a fault (00-01 may be along a fault or an intrusive contact, it is unclear from field relations), and have experienced Na-metasomatism,

supporting the hypothesis that lanthanide and Y enriched fluids percolated along fault planes. In contrast, the apatite with the lowest lanthanide and Y (99-6B and 99-6C) are not associated with faults (Fig. 1-1b) or Na enrichment. Samples 99-6B and 99-6C are entirely K-metasomatised with no evidence of albitization.

The Al concentration in titanite have previously been used to discriminate magmatic vs. hydrothermal titanite (Enami et al., 1993). Enami et al. (1993) noted that magmatic titanite from granitoids tend to be Al-poor, whereas the secondary titanite (formed during the breakdown of aluminous minerals like biotite) were Al-rich and in metamorphic rocks the coupled substitution of Al^{3+} and Fe^{3+} in the Ti *site* increases with increasing pressure. Substitution of Al for Ti depends on the Al/Ti ratio in the fluid and also the H_2O and F activity of the fluid (Lucassen et al., 2010 and references therein). Compared to the magmatic titanite in samples Y-13 and BG in this study, and compared to the results of Lucassen et al. (2010), all of the LMG titanite have elevated Al and F (Fig. 3-7a and b). Such Al and F enrichment, as well as the younger U-Pb titanite dates, the anhedral shape and the presence of titanite only in altered samples, suggest a hydrothermal origin for the LMG titanite.

4.3 Timing of Emplacement, Alteration and Mineralization

A summary of the various dates of events found throughout the LMG and Adirondack Highlands AMCG can be found in Figure 4-1. U-Pb zircon dates of the LMG host rocks and ores are summarized above in the sample descriptions. The zircon dates of

the host rocks range from ~ 1060 Ma to 1033 Ma. These dates are taken from the zircon rims and were inferred to be emplacement ages, core ages range from ~1113 to 1167 Ma. The related ore zircon U-Pb dates range from ~1039 Ma to 1001 Ma, indicating the ores are 20-60 m.y. younger than the respective hosts (e.g. Valley et al. 2009, 2011).

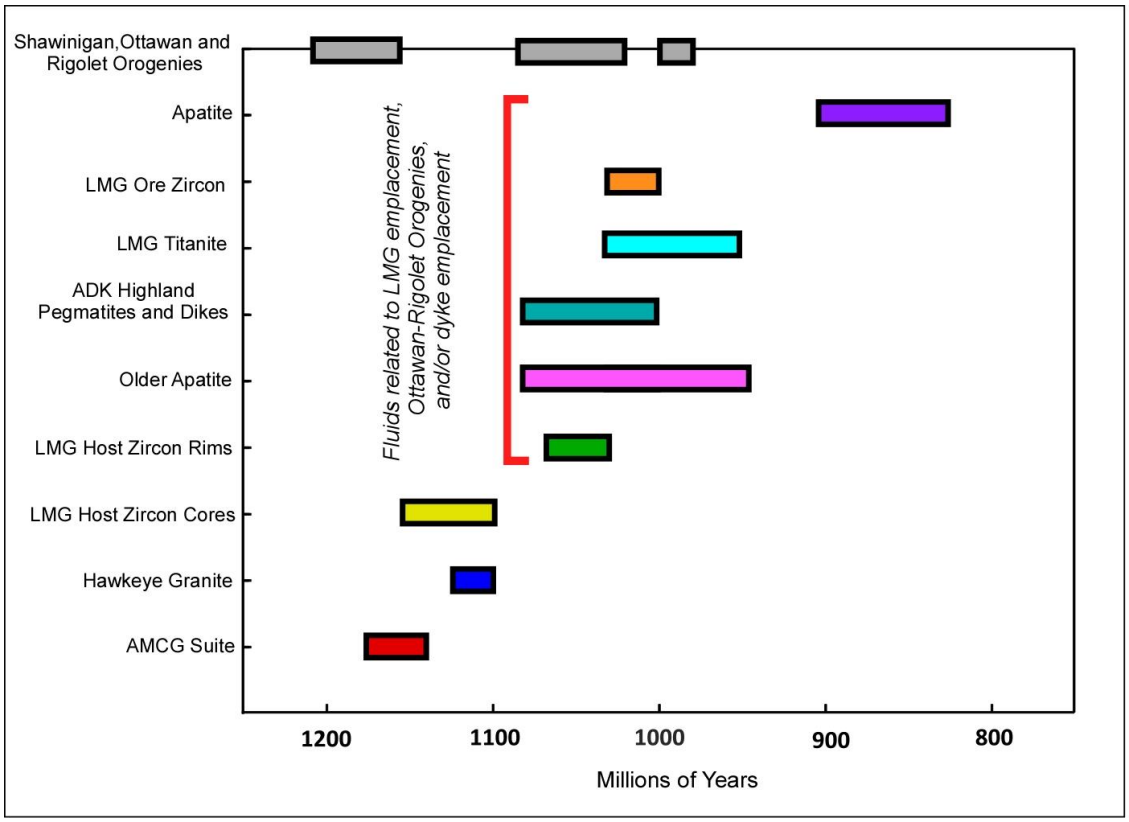

Figure 4-1: Diagram of timing of emplacement of the LMG relative to the AMCG suite and Hawkeye granite with the timing of Fe mineralization and apatite and titanite crystallization and the Ottawan and Rigolet orogenies. Apatite and titanite ages are the averages from the ID-TIMS U-Pb ages taken from this study. Hawkeye granite ages are taken from Chiarenzelli and McLelland (1991); McLelland et al. (2001). AMCG suite ages from McLelland et al. (2004). Adirondack Highland pegmatites and dykes are taken from and Selleck et al. (2004); Valley et al. (2011), Lupulescu et al. (2011) and Shawinigan, Ottawan and Rigolet orogeny ages from Rivers et al. (1997; 2008).

The titanite U-Pb TIMS dates are similar to the ore zircon ages (within error); ranging from ~1035 to 961 Ma. Sample 99-6C has the oldest titanite, which are comparable to the older ore zircon dates (~1039-1016 Ma). However, host rock samples 99-5A and 99-2B (both Na-altered) have younger titanite dates and are more comparable to the zircon ages of ore sample 00-01 (~1001 Ma). The older dates from the titanite from samples 99-2B and 99-6C also correlate with previously reported dates of titanite from the Adirondack Highlands of ~1030-1020 Ma with some younger ages of 991 Ma (Mezger et al., 1991) and 1020-950 Ma (Streepey et al., 2001).

The apatite are distinctly younger than the zircon and titanite, from the ore and host rocks with the exception of apatite sample 06-4B. The apatite TIMS dates vary from ~1069 to 826 Ma, with the oldest dates from ore apatite samples 06-4B and OBO. Overall the apatite U-Pb TIMS dates are about 200 Ma younger than the zircon hosts and about 100 Ma younger than the ore zircon and titanite. It is unclear whether these discrete ages reflect distinct pulses of hydrothermal alteration/mineralization, or reflect a protracted cooling history.

4.3.1 Genetic model for LMG and IOA ores

A genetic model for the LMG IOA ore formation and evolution, accounting for the geologic, geochronological, and geochemical, data and observations described above, has been developed and is shown in Figure 4-2. Constraints on this model come from the host-rock and ore zircon U-Pb ages, the apatite and titanite U-Pb dates, Sm-Nd and Lu-Hf isotopes, sample petrography and field relationships.

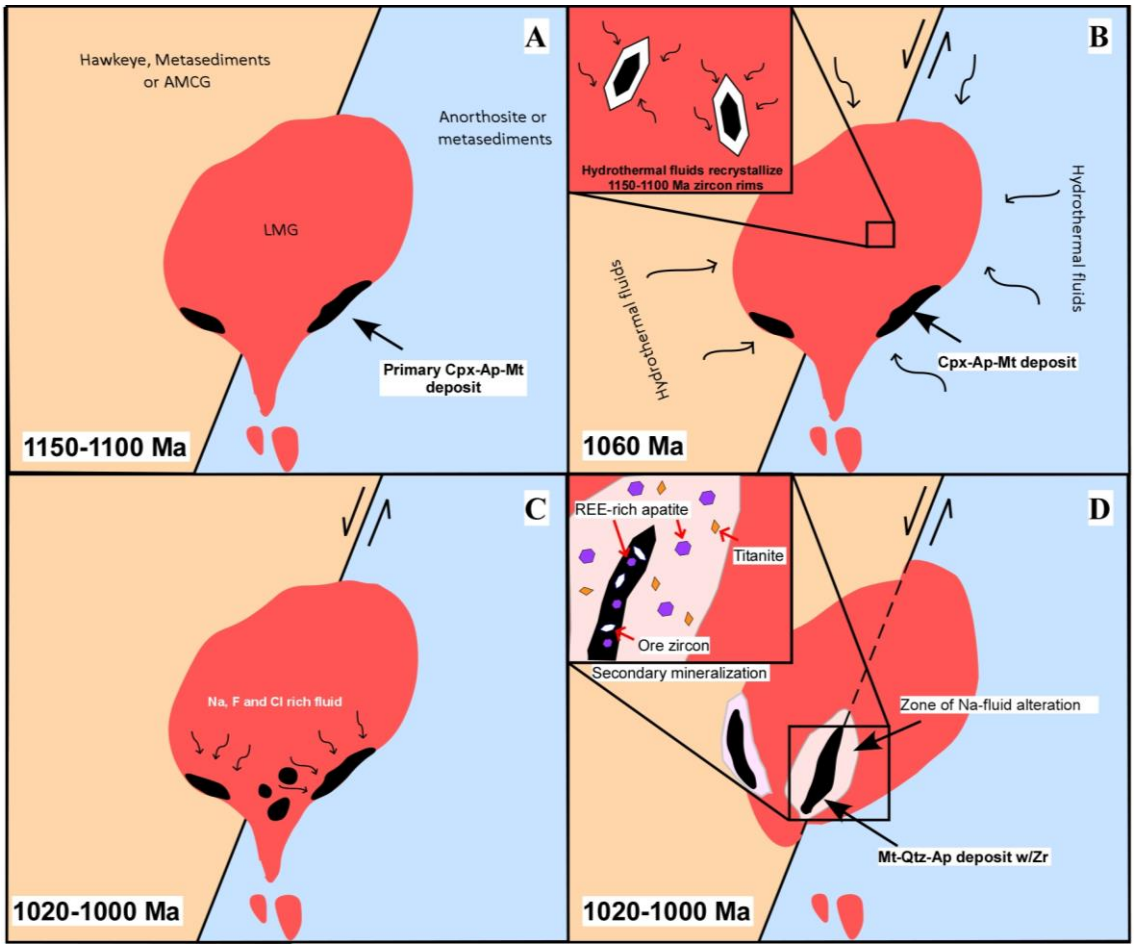

Figure 4-2: Model of the Lyon Mountain Granite emplacement, subsequent alteration and mineralization. A) Emplacement at 1150-1100 Ma with formation of original 'syndepositional' IOA ore. B) Hydrothermal alteration event at ~1060 Ma infiltrating the LMG and resetting the U-Pb host zircon rims. C) ~1020-1000 Ma continuation of the same fluid event or start of another Na, Cl, F rich hydrothermal fluid event which infiltrated the LMG and original IOA ores redistributing them along faults and contacts. D) Crystallization of ore zircon and ore apatite from the alteration of the original LMG and IOA ores, as well as crystallization or recrystallization of host apatite and titanite in alteration zones.

A-B) The LMG was initially emplaced at ~1150-1100 Ma as part of the Adirondack AMCG suite, which is of similar age and the primary IOA ore formed 'syndepositional' during waning stage of LMG crystallization. The LMG was infiltrated

by hydrothermal fluids potentially derived from the Ottawan orogeny at 1090 to 1020 Ma. Infiltrating hydrothermal fluids recrystallized the rims of the host granite zircon, resetting the U-Pb ages to that of the Ottawan orogeny at ~1060 Ma (while preserving the original magmatic cores). In this scenario, all recorded mineral ages (other than the host zircon cores) reflect hydrothermal alteration of the earlier emplaced AMCG.

This model suggests that the heat and fluid source for hydrothermal circulation came from the Ottawan orogeny at 1090-1020 Ma (Rivers, 2008), which caused extensive metamorphism and magmatism and therefore alteration of a 1150 Ma LMG granitoid rather than the emplacement of a new granitoid at 1060 Ma. Evidence supporting this interpretation is provided by the zircon rims and cores of the granite host samples, where cores have consistent older U-Pb ages and the rims lack inclusions, exhibit unusual textures and embayments more akin to hydrothermal alteration than to magmatic or metamorphic overgrowths. The younger zircon core ages found in 99-2B can be explained by the extensive Na-alteration of this sample which was pervasive enough to penetrate and alter the cores of these zircon. This Na-alteration is likely the same Na-alteration that is responsible for the formation of the younger ore zircon and are similar in age to the host zircon dates found from 99-2B in this study.

After the primary emplacement of the LMG at ~1150 Ma ‘syndepositional’ formation of primary IOA deposits occurred during waning stage of LMG crystallization. It is likely that some or all of the ores were originally emplaced with the LMG as an immiscible Fe-rich fluid or silicate melt that was later overprinted by a Na-rich hydrothermal fluid(s) (Valley et al., 2010). Geochemical evidence for this is demonstrated

by the extremely radiogenic nature of the εHf (*t*) of most of the LMG ore zircon. This high εHf (*t*) (> +10) indicates that the likely source for this radiogenic signature was REE-rich apatite or clinopyroxene (i.e., original IOA ore), which was broken down to form the ore zircon (Valley et al., 2010), indicating that the Lu- or REE-rich apatite and/or clinopyroxene must have been in place prior to the ore zircon formation.

It is unclear if this means the original apatite crystallized at 1150 Ma or 1060 Ma. Either is plausible as the ore zircon would require a minimum of only 40 million years at low dissolution rate (based on the model from Valley et al., 2010) of apatite to accumulate enough radiogenic Hf to have this signature. The U-Pb data indicates that the radiogenic ore zircon is ~1020 to 1001 Ma, which is significantly younger than 1060 Ma or 1150 Ma. Field and geochronological evidence for this can be seen in ore sample 06-4B, in which the ore (apatite, clinopyroxene and magnetite) occurs as enclaves partially resorbed in the perthite granite. In this sample the apatite dates vary and include some of the oldest apatite dates up to 1069.27 ± 4.5 (2σ) Ma. This older apatite suggests that this ore may have existed prior to the LMG alteration, as a skarn-like body (i.e., the magnetite-clinopyroxene type ore described above) that formed at the time of the original LMG emplacement. This ore sample (06-4B) also contains apatite with younger ages of 931.94 ± 0.59 Ma (2σ), perhaps indicating resetting of the U-Pb system of this sample during a later fluid infiltration of the LMG. Unfortunately, no zircon crystals were obtained from sample 06-4B; the majority of the Zr is contained in the clinopyroxene (Valley et al., 2010). Note that 06-4B is the only ore sample in the study without zircon.

C and D) Twenty to sixty million years later another metasomatic event occurred, or was possibly the continuation of the same Ottawan event (extends until ~1020 Ma), which recrystallized the host zircon rims. LMG ore zircon are similar in age to the pegmatites and dykes in the area (McLelland et al., 2001; Selleck et al., 2004; Valley et al., 2011; Lupuescu et al., 2011) suggesting that continued magmatism related to orogenic extension (Valley et al., 2011) around 1040-1016 Ma likely supplied the heat for the hydrothermal circulation for the formation of the LMG ores. These fluids were enriched in Na, F, and likely Cl, which remobilized Fe, REE and HFSE from the primary LMG IOA deposits. This resulted in the formation of the low-Ti iron-ore deposits generally located along faults or contacts around 1039-1001 Ma. Hydrothermal ore zircon, titanite and REE-rich apatite crystallized at this time and may be related to fluid flow resulting from the development of the faults in the area. The alteration and remobilization of the original IOA ores, something akin to 06-4B with magnetite, apatite and clinopyroxene resulted in the formation of the hydrothermal ore zircon and REE-rich apatite in the magnetite ore and REE enriched apatite and titanite in the host granite alteration zones, as these minerals are predominantly found in the altered areas of the host granites. Altered major minerals such as feldspar and clinopyroxene in the LMG granitoids also demonstrate evidence of HFSE, REE and Fe leaching contributing to concentration of HFSE, REE and Fe rich fluids to crystallize the REE-rich apatite around ~1007- ~825 Ma (younger ages may be the result of lower closure temperatures of apatite), or it is possible that the fluid just recrystallized the already REE-rich apatite and reset the U-Pb dates.

Titanite crystallized either during the cooling of the LMG, or was recrystallized by a later hydrothermal or metasomatic event. The titanite dates are similar to those of the ores, dykes, and pegmatites, and may represent the same fluid event. However, these IOA deposits contain low-Ti magnetite in the LMG ores and host rocks (Valley et al., 2011) and likely would have preferentially incorporated Ti, if Ti was available during magnetite crystallization (Bleil, 1976). The reason Ti was not incorporated into the magnetite is not clear, but may indicate that hydrothermal titanite crystallized prior to or during the ore mineralization, thereby sequestering the available Ti, or post-dated the ore mineralization when later Ti rich fluids were introduced into the LMG.

Chapter 5. Conclusions

1) The LMG host rocks have chemical characteristics of ferroan granites, including high Fe-index, and enrichment in alkalis, HFSE and REE. The igneous precursor of these rocks contained the chemical components necessary to create the IOA ores and high REE apatite.

2) The original ferroan LMG rocks produced a 'syndepositional' IOA deposit that was later hydrothermally altered to produce many of the ores seen today. Petrography, whole-rock CIA diagrams, and accessory mineral geochemistry, all suggest that the a Na-rich fluid was responsible for leaching and mobilizing Fe, HFSE and REE from the local LMG rocks to form the magnetite ores and accessory minerals such as zircon, apatite and titanite.

3) The timing of emplacement and subsequent metasomatic alteration poses a dilemma in unravelling the paragenesis. It is not yet possible to constrain the exact order of metasomatic or hydrothermal events. Moreover, the heat source driving these mechanisms are unclear.

The probable emplacement, mineralization, alteration and timing scenarios is as follows:

• The Lyon Mountain granite was emplaced around 1150-1100 Ma with the AMCG suite of the area and the primary 'syndepositional' IOA ore formed around this

time. The LMG subsequently experienced metasomatism or hydrothermal alteration at 1060 Ma infiltrating and altering the original host zircon rims.

• 20-60 Ma later, a hydrothermal event, enriched in Na, F and Cl, mobilized Fe, REE and HFSE occurred. This hydrothermal event remobilized the primary IOA ores, producing the low-Ti IOA iron ore deposits and with ore zircon ages around 1039-1001 Ma, coinciding with titanite and apatite crystallization/recrystallization at ~1035-825 Ma.

References

Alcock, J., Isachsen, C., Livi, K., and Muller, P., 2004, Unraveling growth history of zircon in anatectites from the northeast Adirondack Highlands, New York; constraints on pressure-temperature-time paths, Memoir - Geological Society Of America, v. 197, p. 267-284.

Anders, E. and Grevesse, N., 1989, Abundances of the elements: Meteoritic and solar. Geochimica et Cosmochimica Acta 53, p. 197-214.

Armstrong, J.T. (1988) Quantitative analysis of silicate and oxide materials: comparison of Monte Carlo, ZAF and φ(ρz) procedures. In: Microbeam Analysis - 1988, Newbury, D.E. ed, San Francisco Press, San Francisco, 239 - 246.

Blanc, P., Roger, G., and Couto, H., 1993, Recherche de signatures magmatique et hydrothermale dans des apatite du nord du Portugal: étude par cathodoluminescence, microscopie électronique à balayage et microsonde électronique, Bulletin de la Société Géologique de France, v. 4, p. 329-339.

Bleil, U., 1976, An experimental study of the titanomagnetic solid solution series, Pure And Applied Geophysics, 114, 2, p. 165-17.

Bonin, B., 2007, A-type granites and related rocks; evolution of a concept, problems and prospects, Lithos, v. 97, no. 1-2, p. 1-29.

Cathelineau, M., 1987, U-Th-REE mobility during albitization and quartz dissolution in granitoids; evidence from South-east French Massif Central, Bulletin De Minéralogie, 110, 2-3, p. 249-259.

Cherniak, DJ., 2010, Diffusion in accessory minerals; zircon, titanite, apatite, monazite and xenotime, Reviews In Mineralogy And Geochemistry, 72, p. 827-869.

Chiarenzelli, J., and McLelland, J., 1991, Age and regional relationships of granitoid rocks of the Adirondack highlands, Journal Of Geology, 99, 4, p. 571-590.

Chiarenzelli, J., and McLelland, J., 1993, Granulite facies metamorphism, palaeo-isotherms and disturbance of the U-Pb systematics of zircon in anorogenic plutonic rocks from the Adirondack Highlands, Journal Of Metamorphic Geology, v. 11, no. 1, p. 59-70.

Clemens, J, Holloway, J, and White, A., 1986, Origin of an A-type granite; experimental constraints, American Mineralogist, 71, 3-4, p. 317-324.

Collins, W, Beams, S, White, A, and Chappell, B., 1982, Nature and origin of A-type granites with particular reference to southeastern Australia, Contributions To Mineralogy And Petrology, 80, 2, pp. 189-200.

Corfu F., Hanchar J., Hoskin P. and Kinny P., 2003, An atlas of zircon textures, In Zircon, J.M. Hanchar and P.W.O. Hoskin, Eds., Reviews in Mineralogy and Geochemistry 53, Mineralogical Society of America, Washington, D.C. p. 469-500.

Crowley, J., Schoene, B., and Bowring, S., 2007, U-Pb dating of zircon in the Bishop Tuff at the millennial scale. Geology, v. 35, p. 1123-1126.

Daly, J. and McLelland, J., 1991, Juvenille Middle Protozoic Crust in the Adirondack Highlands, Grenville Province, Northeastern North America. Geology, v. 19, p. 119-122.

Dempster, T., Jolivet, M., Tubrett, M., and Braithwaite, C., 2003, Magmatic zoning in apatite: a monitor of porosity and permeability change in granites, Contributions to Mineral and Petrology, v. 145, p. 568-577.

Enami, M., Suzuki, K., Liou, J. and Bird, D., 1993, Al-Fe^{3+} and F-OH substitutions in titanite and constraints on their P-T dependence, European Journal Mineralogy, v. 5, p. 219-231.

Fedo, C, Nesbitt, H, and Young, 1995, Unraveling the effects of potassium metasomatism in sedimentary rocks and Paleosols, with implications for paleoweathering conditions and provenance, Geology, v. 23, 10, p. 921-924.

Fisher, C., McFarlane, Christopher R., Hanchar, J., Schmitz, M., Sylvester, P., Lam, R., and Longerich, H., 2011, Sm–Nd isotope systematics by laser ablation-multicollector-inductively coupled plasma mass spectrometry: Methods and potential natural and synthetic reference materials, Chemical Geology, v. 284, p. 1-20.

Foose, M., and McLelland, J., 1995, Proterozoic low-Ti iron-oxide deposits in New York and New Jersey: Relation to Fe-oxide (Cu–U–Au–rare earth element) deposits and tectonic implications, Geology, v. 23, no. 7, p. 665-668.

Frost, C., and Frost, B., 1997, Reduced rapakivi-type granites: The tholeiite connection, Geology, v. 25, no. 7, p. 647-650.

Frost, C., Frost, B., Bell, J., Chamberlain, K., 2002, The relationship between A-type granites and residual magmas from anorthosite: evidence from the northern Sherman batholith, Laramie Mountains, Wyoming, USA. Precambrian Research, v. 119, p. 45-71.

Frost, C., and Frost, B., 2011, On Ferroan (A-type) Granitoids: their compositional variability and modes of origin, Journal of Petrology, v. 52, p. 39-53.

Gallagher, D., 1937, Origin of the magnetite deposits of Lyon Mountain, New York: New York State Mus. Bull. 311, pp. 85.

Gaudette, H., Vitrac-Michard, A., and Allegre, C., 1981, North American Precambrian history recorded in a single sample; high-resolution U-Pb systematics of the Potsdam Sandstone detrital zircons, New York State, Earth And Planetary Science Letters, 54, 2, p. 248-260.

Geisler, T., Pidgeon, R., Kurtz, R., Van Bronswijk, W., and Scheicher, H., 2003a, Experimental hydrothermal alteration of partially metamict zircon, American Mineralogist, v. 88, p. 1496-1513.

Geisler, T., Rashwan, M., Rahn, W., Poller, U., Zwingmann H., Pidgeon, R. T., Schleicher, H. and Tomaschek, F, 2003b, Low-temperature hydrothermal alteration of natural metamict zircons from the Eastern Desert, Egypt, Mineralogical Magazine, v. 67; no.3, p. 485-508.

Ginibre, C., Worner, G., and Kronz, A., 2002, Minor- and trace-element zoning in plagioclase: implications for magma chamber processes at Parinacota volcano, northern Chile, Contributions to Mineralogy and Petrology, v. 143, p. 300-315.

Gerstenberger, H., and Haase, G., 1997, A highly effective emitter substance for mass spectrometric Pb isotope ratio determinations, Chemical. Geology, v.136, p. 309-312.

Goudie, D., Fisher, C., Hanchar, J., Crowley, J., and Ayers, J., 2014, Simultaneous in situ determination of U-Pb and Sm-Nd isotopes in monazite by laser ablation ICP-MS, Geochemistry, Geophysics, Geosystems, v.15, no. 6, p. 2575-2600.

Hall, A., 1967, The distribution of some major and trace elements in feldspars from the Rosses and Ardara granite complexes, Donegal, Ireland, Geochimica et Cosmochimica Acta, v. 31, p. 835-847.

Hamilton, M., McLelland, J., and Selleck., B., 2004, SHRIMP U-Pb zircon geochronology of the anorthosite-mangerite-charnockite-granite suite, Adirondack Mountains, New York; ages of emplacement and metamorphism, Memoir - Geological Society Of America, v. 197, p. 337-355.

Harlov, D., Andersson, U., Foerster, H., Nystrom, J., Dulski, P., and Broman, 2002, Apatite-monazite relations in the Kiirunavaara magnetite-apatite ore, northern Sweden, Chemical Geology, v. 191, 1-3, pp. 47-72.

Henke, B.L., Lee, P., Tanaka, T.J., Shimabukuro, R.I. & Fujikawa, B.K., 1982, Low energy X-ray interaction coefficients: photoabsorption, scattering and reflection. Atomic Data and Nuclear Data Tables, v. 27, p. 1 - 144.

Hitzman, M.W., Oreskes, N. and Einaudi, M. T., 1992, Geological characteristics and tectonic setting of Proterozoic iron oxide (Cu-U-Au-REE) deposits, Precambrian Research, v. 58, p. 241-287.

Hoskin, P., and Schaltegger, U., 2003, The composition of zircon and igneous and metamorphic petrogenesis, In Zircon, J.M. Hanchar and P.W.O. Hoskin, Eds., Reviews In Mineralogy And Geochemistry, v. 53, p. 27-62.

Hoskin, P., 2005, Trace-element composition of hydrothermal zircon and the alteration of Hadean zircon from the Jack Hills, Australia, Geochimica et Cosmochimica Acta, v. 69; no. 3, p. 637-648.

Hovelmann, J., Putnis, A., Geisler, T., Schmid, B. C., and Golla-Schindler, U., 2010, The replacement of plagioclase feldspars by albite: observations from hydrothermal experiments. Contributions to Mineralogy and Petrology, v. 159, p. 43-59.

Hughes, C., 1973, Spilites, keratophyres, and the igneous spectrum, Geological Magazine, v. 109, 6, p. 513-527.

Isachsen, Y.W. and Fisher, D. W., 1971, Geologic map of New York State: Adirondack sheet: New York State Museum Science Service Map and Chart Series 15, scale 1:250,000.

Jaffey, A.H., Flynn, K.F., Glendenin, L.E., Bentley, W.C., and Essling, A.M., 1971, Precision measurements of half-lives and specific activities of ^{235}U and ^{238}U, Physical Review C, v. 4, p. 1889-1906.

Jochum, K.P., Wilbrod, M., Raczek, I., Stoll, B., Herwig, K., 2005, Chemical characterisation of the USGS reference glasses GSA 1G, GSC-1G, GSD-1G, GSE-1G, BCR-2G, BHVO-2G and BIR-1G using EPMA, ID-TIMS, ID-ICP-MS and LA-ICP-MSD, Geostandards and Geoanalytical Research, v. 29, no.3, p. 285-302.

Kinnaird, J. A., 1985, Hydrothermal alteration and mineralization of the alkaline anorogenic ring complexes of Nigeria, Journal Of African Earth Sciences, v. 3, no. 1-2, p. 229-251.

Krogh, T.E., 1973, A low contamination method for hydrothermal decomposition of zircon and extraction of U and Pb for isotopic age determination, Geochimica et Cosmochimica Acta, v. 37, p, 485-494.

Larsen, R. B., 2002, The Distribution of Rare Earth Elements in K-Feldspar as an Indicator of Petrogenetic Processes in Granitic Pegmatites: Examples From Two Pegmatite Fields in Southern Norway, The Canadian Mineralogist, v. 40, p. 137-151.

Lucassen, F., Dulski, P., Abart, R., Franz, G., Rhede, D., and Romer, R., 2010, Redistribution of HFSE elements during rutile replacement by titanite, Contributions To Mineralogy And Petrology, v. 160, 2, p. 279-295.

Ludwig, K.R., 2003, User's Manual for Isoplot 3.00. Berkeley Geochronology Center: Berkeley, CA, p. 70.

Lupulescu, M., Chiarenzelli, J., Pullen, A., and Price, J., 2011, Using pegmatite geochronology to constrain temporal events in the Adirondack Mountains, Geosphere, v. 7, 1, p. 23-39.

McLelland, J., and Whitney, P., 1980, A generalized garnet-forming reaction for metaigneous rocks in the Adirondacks, Contributions To Mineralogy And Petrology, v. 72, 2, p. 111-122.

McLelland, J., and Isachsen, Y.W., 1985, Geologic evolution of the Adirondack Mountains: A review, in Tobi, A., and Touret, J., eds., The deep Proterozoic crust in the North Atlantic provinces: NATO Advanced Study Institute Series C, v. 158, p. 175-215.

McLelland, J.M., and Chiarenzelli, J., 1990, Isotopic constraints on emplacement age of anorthosite rocks of the Marcy Massif, Adirondack Mts., New York, Journal of Geology, v. 98, p. 19-41.

McLelland, J., Hamilton, M., Selleck, B., McLelland, J., Walker, D., and Orrell, S., 2001, Zircon U-Pb geochronology of the Ottawan Orogeny, Adirondack Highlands, New York: regional and tectonic Implications, Precambrian Research, v. 109, p. 39-72.

McLelland, J., Morrison, J., Selleck, B., Cunningham, B., Olson, C., and Schmidt, K., 2002, Hydrothermal alteration of late- to post-tectonic Lyon Mountain granitic gneiss, Adirondack Mountains, New York; origin of quartz-sillimanite segregations, quartz-albite lithologies, and associated Kiruna-type low-Ti Fe-oxide deposits, Journal of Metamorphic Geology, v. 20, p. 175-190.

McLelland, J.M., Bickford, M.E., Hill, B.M., Clechenko, C.C., Valley, J.W., and Hamilton, M.A., 2004, Direct dating of Adirondack Massif anorthosite by U-Pb SHRIMP analysis of igneous zircon; implications for AMCG complexes, Geological Society Of America Bulletin, v. 116, 11-12, p. 1299-1317.

Mezger, K., Rawnsley, C., Bohlen, S., and Hanson, G., 1991, U-Pb garnet, sphene, monazite, and rutile ages; implications for the duration of high-grade metamorphism and cooling histories, Adirondack Mts., New York, Journal Of Geology, v. 99, 3, p. 415-428.

Mitchell, R, Xiong, J, Mariano, A, and Fleet, M., 1997, Rare-earth-element-activated cathodoluminescence in apatite, Canadian Mineralogist, v. 35, Part 4, p. 979-998.

Montgomery, C., and Brace, W., 1975, Micropores in plagioclase, Contributions To Mineralogy And Petrology, v. 52, 1, p. 17-28.

Nasdala, L., Lengauer, C.L., Hanchar, J.M., Kronz, A., Wirth, R., Blanc, P., Kennedy, A.K. and Seydoux-Guillaume, A.-M., 2002, Annealing metamictisation and the recovery of cathodoluminescence, Chemical Geology, v. 191, p.121-140.

Nasdala, L., Hanchar, J.M., Whitehouse, M.J. and Kronz, A., 2005, Long-term stability of alpha particle damage in natural zircon, Chemical Geology, v 220, p. 83-103.

Nasdala, L., Kronz, A., Hanchar, J.M., Tichomirowa, M., Davis, D.W. and Hofmeister, W., 2006, Effects of natural radiation damage on back-scattered electron images of single-crystals of minerals, American Mineralogist, v. 91, p. 1739-1746.

Nesbitt, H., and Young, G., 1984, Prediction of some weathering trends of plutonic and volcanic rocks based on thermodynamic and kinetic considerations: Geochimica et Cosmochimica Acta, v. 48, p. 1523-1534.

Nesbitt, H., and Young, G., 1989, Formation and diagenesis of weathering profiles, Journal Of Geology, v. 97, 2, p. 129-147.

Pan, Y., and Fleet, M., 2002, Compositions of the apatite group minerals; substitution mechanisms and controlling factors, Reviews In Mineralogy And Geochemistry, v. 48, p. 13-49

Paterson, B., and Stephens, W., 1992, Kinetically induced compositional zoning in titanite; implications for accessory-phase/melt partitioning of trace elements, Contributions To Mineralogy And Petrology, v. 109, 3, p. 373-385.

Paton, C., Woodhead, J., Hellstrom, J., Hergt, J., Greig, A., and Maas, R., 2010, Improved laser ablation U-Pb zircon geochronology through robust downhole fractionation correction, Geochemistry, Geophysics, Geosystems - G^3, v. 11, p.3.

Pearce N.J.G., Perkins W.T., Westgate J.A., Gorton M.P., Jackson S.E., Neal C.R. and Chenery S.P., 1997, A compilation of new and published major and trace element data for NIST SRM 610 and NIST SRM 612 glass reference materials, Geostandards Newsletter: The Journal of Geostandards and Geoanalysis, v. 21, p. 115-144.

Pelleter, E., Cheilletz, A., Gasquet, D., Mouttaqi, A., Annich, M., El Hakour, A., Deloule, E., and Feraud, G., 2007, Hydrothermal zircons; a tool for ion microprobe U/Pb dating of gold mineralization (Tamlalt-Menhouhou gold deposit, Morocco), Chemical Geology, v. 245, 3-4, p. 135-161.

Pettke, T., Audétat, A., Schaltegger, U., Heinrich, C.A., 2005, Magmatic-to-hydrothermal crystallization in the W–Sn mineralized Mole Granite (NSW, Australia) Part II: Evolving zircon and thorite trace element chemistry, Chemical Geology, v. 220, p. 191-213.

Piccoli, P., and Candela, P., 2002, Apatite in igneous systems, In Phosphates – Geochemical, Geobiological, and Materials Importance, M.L. Kohn, J. Rakovan, and J.M. Hughes, Eds., Reviews In Mineralogy And Geochemistry, v. 48, p. 255-292.

Postel, A., 1952, Geology of the Clinton County magnetite district, New York, U. S. Geological Survey Professional Paper.

Pryer, L., and Robin, P., 1995, Retrograde metamorphic reactions in deforming granites and the origin of flame perthite, Journal Of Metamorphic Geology, v. 13, 6, p. 645-658.

Pryer, L., Robin, P. and Lloyd, G., 1995, An SEM Electron-channeling Study of Flame Perthite From the Killarney Granite, Southwestern Grenville Front, Ontario, The Canadian Mineralogist, v. 33, p. 333-347.

Reynolds, L.J., 2000, Geology of the Olympic Dam Cu-U-Au-Ag-REE deposit, in Porter, T.M., ed., Hydrothermal iron oxide copper-gold and related deposits: A global perspective. Volume 1: Adelaide, Australia, PGC Publishing, p. 93-104.

Rivers, T., 1997, Lithotectonic elements of the Grenville Province: Review and tectonic implications, Precambrian Research, v. 86, p. 117-154.

Rivers, T., 2008, Assembly and preservation of lower, mid, and upper orogenic crust in the Grenville Province; implications for the evolution of large hot long duration orogens, Precambrian Research, v. 167, 3-4, p. 237-259.

Roeder, Peter L., MacArthur, Duncan, Ma, Xin-Pei, Palmer, Gerald R., Mariano, Anthony N., 1987, Cathodoluminescence and microprobe study of rare-earth elements in apatite, American Mineralogist, v. 72, p. 801-811.

Rubin, J., Henry, C., and Price, J., 1989, Hydrothermal zircons and zircon overgrowths, Sierra Blanca Peaks, Texas, American Mineralogist, v. 74, 7-8, p. 865-869.

Salvi, S. and Williams-Jones, A., 1996, The role of hydrothermal processes in concentrating high-field strength elements in the Strange Lake peralkaline complex, northeastern Canada, Geochimica et Cosmochimica Acta, v. 60, no. 11, p. 1917-1932.

Schmitz, M.D., Schoene, B., 2007, Derivation of isotope ratios, errors and error correlations for U-Pb geochronology using ^{205}Pb-^{235}U-(^{233}U)-spiked isotope dilution thermal ionization mass spectrometric data. Geochemistry, Geophysics, Geosystems - G^3, 8.

Selleck, B., McLelland, J., and Hamilton, M., 2004, Magmatic-hydrothermal leaching and origin of late to post-tectonic quartz-rich rocks, Adirondack Highlands, New York, Memoir - Geological Society Of America, v. 197, p. 379-390.

Slaby, E., Seltmann, R., Kober, B., Muller, A., Galbarczyk-Gasiorowska and Jefferies, T., 2007, LREE distribution patterns in zoned alkali feldspar megacrysts from the Karkonosze pluton, Bohemian Massif- implications for parental magma composition. Mineralogical Magazine, v. 71, no. 2, p. 155-178.

Souders, A., Sylvester, P., Myers, J., 2013, Mantle and crustal sources of Archean anorthosite; a combined in situ isotopic study of Pb-Pb in plagioclase and Lu-Hf in zircon, Contributions To Mineralogy And Petrology, v.165, no. 1, p. 1-24.

Stacey, J.S., Kramers, J.D., 1975, Approximation of terrestrial lead isotope evolution by a two-stage model, Earth and Planetary Science Letters, v. 26, p. 207-221.

Streepey, M. M., Johnson, E. L., Mezger, K., van der Pluijm, B. A., 2001, Early History of the Carthage-Colton Shear Zone, Grenville Province, Northwest Adirondacks, New York (U.S.A.), Journal of Geology, v. 109, no. 4, p. 479-492.

Taylor, R.P., Strong, D.F., and Fryer, B.J., 1981, Volatile Control of Contrasting Trace Element Distributions in Peralkaline Granitic and Volcanic Rocks, Contributions to Mineralogy And Petrology, v. 77, p. 267-271.

Tiepolo, M., Oberti, R., Vannucci, R., 2002, Trace-element incorporation in titanite: constraints from experimentally determined solid/liquid partition coefficients, Chemical Geology, v. 191, p. 105-119.

Tomaschek, F., Kennedy, A., Villa, I., Lagos, M. and Ballhaus, C., 2003, Zircons from Syros, Cyclades, Greece: Recrystallization and Mobilization of Zircon During High-Pressure Metamorphism, Journal of Petrology, v. 44, no.11, p. 1977-2002.

Valley, P., Hanchar, J., and Whitehouse, M., 2009, Direct dating of Fe oxide-(Cu-Au) mineralization by U/Pb zircon geochronology, Geology, v. 37, no. 3, p. 223-226.

Valley, P., Fisher, C., Hanchar, J., Lam, R., and Tubrett, M., 2010, Hafnium isotopes in zircon; a tracer of fluid-rock interaction during magnetite-apatite ('Kiruna-type') mineralization, Chemical Geology, v.275, 3-4, p. 208-220.

Valley, P. M., Hanchar, J. M., and Whitehouse, M.J., 2011, New insights on the evolution of the Lyon Mountain Granite and associated Kiruna-type magnetite-apatite deposits, Adirondack Mountains, New York State, Geosphere, v. 7, no. 2, p. 357-389.

Van Achterbergh, E., Ryan, C.G., Jackson, S.E., and Griffin, W.L., 2001, LA-ICP-MS in the Earth Sciences - Appendix 3, data reduction software for LA-ICP-MS, *in* Sylvester, P.J., ed., Short Course volume 29: St. John's, Mineralogical Association of Canada, p. 239-243.

Volp, K., 2005, The Estrela copper deposit, Carajás, Brazil: Geology and implications of a Proterozoic copper stockwork, Mineral Deposit Research: Proceedings of the Eighth Biennial SGA Meeting, Beijing, China, 18 - 21 August 2005, Chapter 9-56, p.1085-1088.

Waldron, K., Lee, M., and Parsons, I., 1994, The microstructures of perthitic alkali feldspars revealed by hydrofluoric acid etching, Contributions To Mineralogy And Petrology, v. 116, 3, p. 360-364.

Wasteneys, H., McLelland, J., and Lumbers, S., 1999, Precise zircon geochronology in the Adirondack Lowlands and implications for revising plate-tectonic models of the Central Metasedimentary Belt and Adirondack Mountains, Grenville Province, Ontario and New York, Canadian Journal of Earth Sciences, v. 36, p. 967-984.

Whalen, J., Currie, K., and Chappell, B., 1987, A-type granites: geochemical characteristics, discrimination and petrogenesis, Contributions To Mineralogy And Petrology, v. 95, p. 407-419.

Whitney, P., and Olmsted, J., 1988, Geochemistry and origin of albite gneisses, northeastern Adirondack Mountains, New York, Contributions To Mineralogy And Petrology, v. 99, p. 476-484.

Wiedenbeck, M., Alle, P., Corfu, F., Griffin, W., Meier, M., Oberli, F., Von Quadt, A., Roddick, J., and Spiegel, W., 1995, Three natural zircon standards for U-Th-Pb, Lu-Hf, trace element and REE analyses, Geostandards Newsletter, v. 19, 1, p. 1-23.

Wiedenbeck, M., Hanchar, J., Peck, W., Sylvester, P., Valley, J., Whitehouse, M., Kronz, A., Morishita, Y., Nasdala, L., Fiebig, J., Franchi, I., Girard, J., Greenwood, R., Hinton, R., Kita, N., Mason, P., Norman, M., Ogasawara, M., Piccoli, P., Rhede, D., Satoh, H., Schulz-Dobrick, B., Skar, O., Spicuzza, M., Terada, K., Tindle, A., Togashi, S., Vennemann, T., Xie, Q., and Zheng, Y., 2004, Further characterisation of the 91500 zircon crystal, Geostandards And Geoanalytical Research, v. 28, 1, p. 9-39.

Williams-Jones, A., Migdisov, A., and Samson, I., 2012, Hydrothermal mobilisation of the rare earth elements; a tale of 'ceria' and 'yttria', Elements, v. 8, 5, p. 355-360.

Wood, S.A., 1990, The aqueous geochemistry of the rare-earth elements and yttrium: 2. Theoretical predictions of speciation in hydrothermal solutions to 350°C at saturation water vapor pressure, Chemical Geology, v. 88, no. 1-2, p. 99-125.

Worden, R., Walker, F., Parsons, I., and Brown, W., 1990, Development of microporosity, diffusion channels and deuteric coarsening in perthitic alkali feldspars, Contributions To Mineralogy And Petrology, v. 104, 5, p. 507-515.

Appendix A

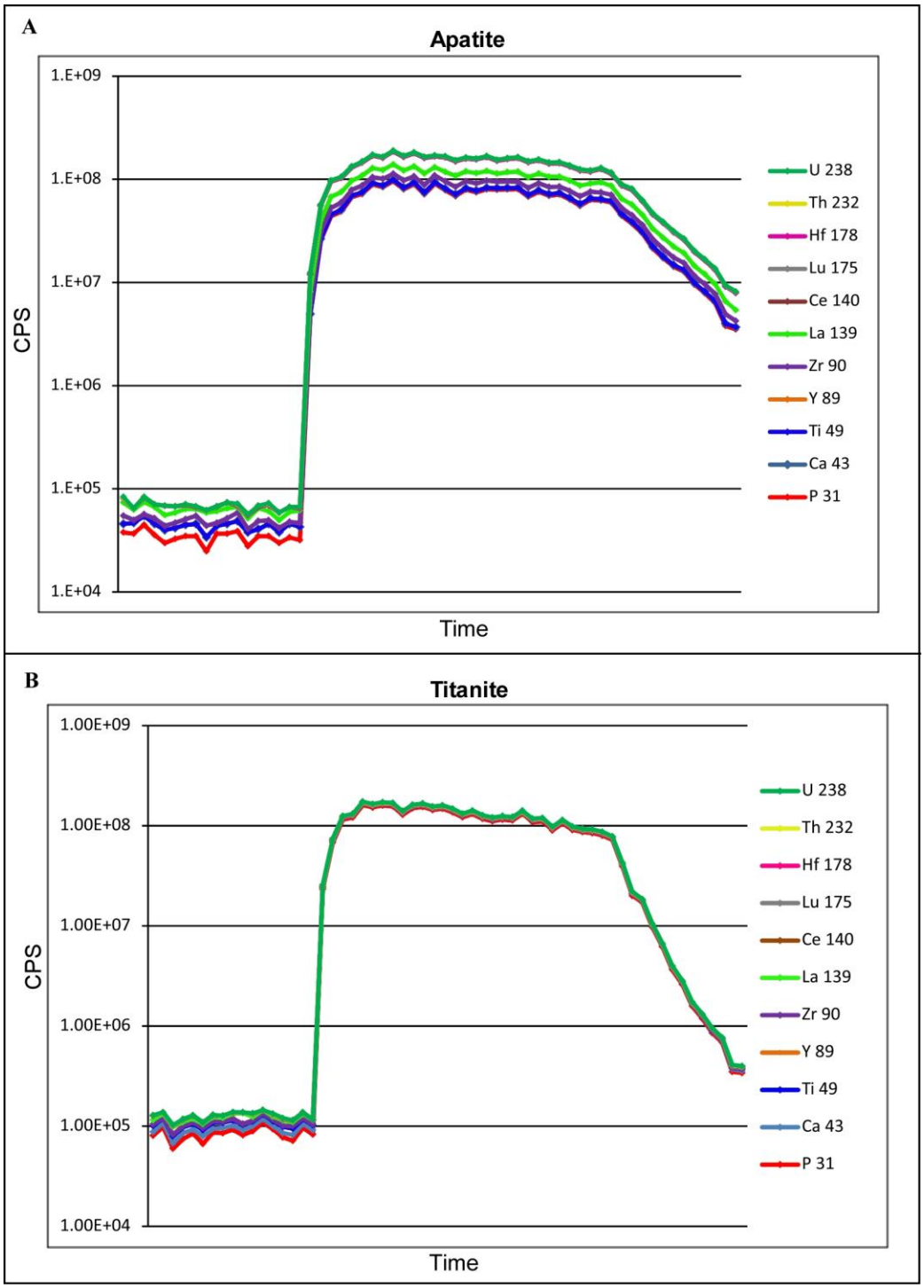

Figure A-1**:** A) Apatite time vs. Element counts per second (CPS) plot, demonstrating the smoothness of the analyses and lack of inclusions. B) Titanite time vs. Element counts per second (CPS) plot, demonstrating the smoothness of the analyses and lack of inclusions.

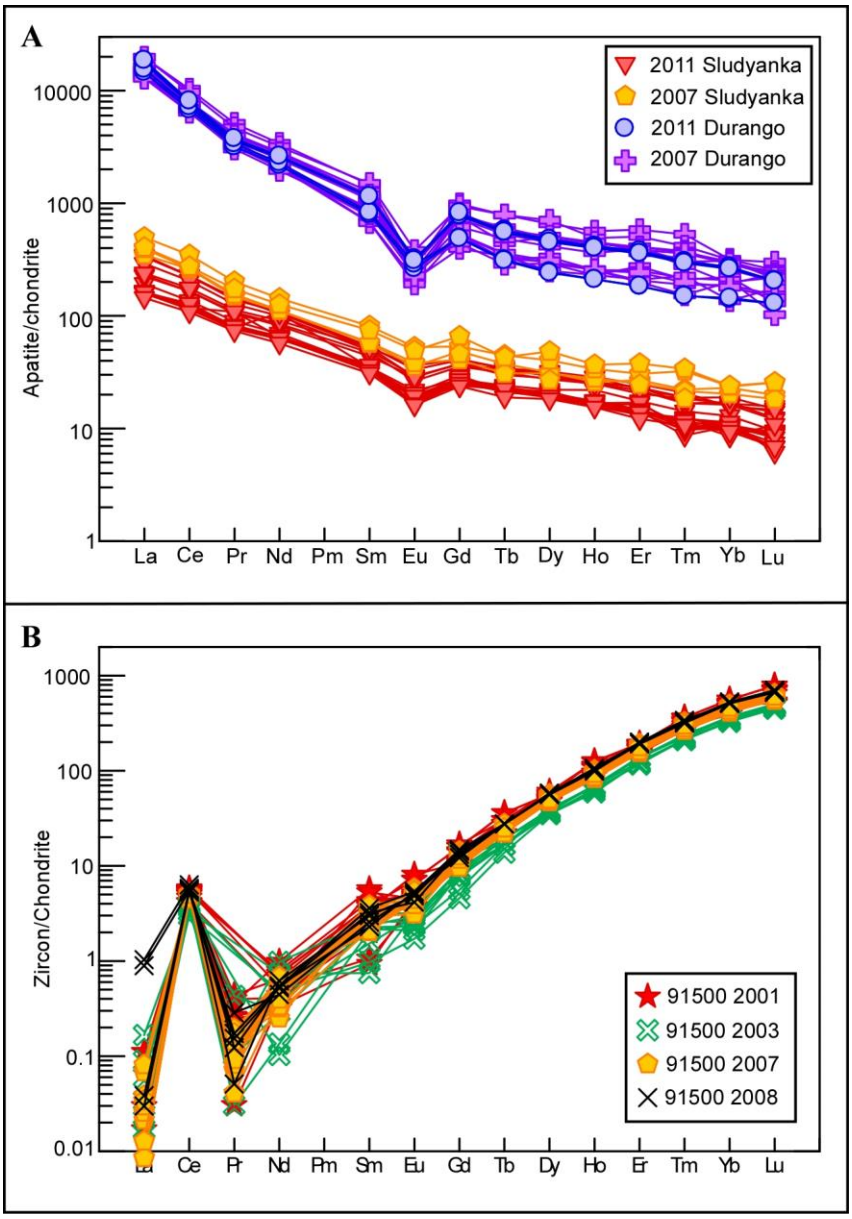

Figure A-2**:** A) Anders and Grevesse (1989) chondrite normalized REE plot for apatite standards Sludyanka and Durango from Memorial University of Newfoundland spanning 2007-2011. B) Anders and Grevesse (1989) chondrite normalized REE plot for zircon standard 91500 from Memorial University of Newfoundland spanning 2001-2008.

Table A-1: Apatite LA-ICPMS analyses on apatite standards from 2007-2011 at Memorial University of Newfoundland

Sample	Sludyanka 2011														
ppm															
La	80.4	45.2	52.6	78.7	68.4	53.9	56.1	37.5	37.5	38.6	37.1	37.4	37.8	37.6	38.7
Ce	137	82.0	100	136	124	100	106	70.8	71.1	73.8	69.8	68.9	70.0	70.7	72.9
Pr	14.1	8.8	10.3	13.6	12.5	10.6	11.1	7.80	10.6	7.93	7.60	7.50	7.88	7.95	8.1
Nd	49.0	32.6	38.2	50.9	46.4	39.7	42.3	29.9	30.4	30.9	28.9	29.2	29.4	29.2	30.5
Sm	7.62	5.14	6.44	7.90	7.21	6.96	7.70	5.31	4.83	4.98	5.09	4.91	4.98	5.29	5.11
Eu	2.02	1.22	1.60	1.87	1.63	1.48	1.61	1.01	1.05	1.10	1.02	1.12	1.15	0.93	0.91
Gd	8.14	5.34	7.41	7.98	7.33	6.98	7.36	4.72	4.99	5.40	5.20	5.07	5.84	5.38	5.67
Tb	1.24	0.87	1.08	1.25	1.22	1.14	1.19	0.81	0.77	0.84	0.80	0.83	0.76	0.82	0.81
Dy	7.77	5.36	6.79	7.44	7.08	6.63	7.20	4.53	4.59	4.94	4.84	4.73	4.74	5.16	4.78
Ho	1.59	1.22	1.39	1.44	1.41	1.39	1.56	0.90	0.92	0.98	0.87	0.91	0.97	0.93	0.96
Er	3.94	2.78	3.47	3.67	3.70	3.24	3.58	2.62	2.27	2.34	2.10	2.19	2.20	2.70	2.18
Tm	0.50	0.34	0.40	0.46	0.41	0.45	0.45	0.26	0.21	0.27	0.30	0.23	0.27	0.24	0.30
Yb	2.54	2.10	2.79	2.65	2.64	2.71	3.07	1.71	1.71	1.57	1.65	1.67	1.74	1.68	1.75
Lu	0.36	0.23	0.30	0.34	0.29	0.38	0.36	0.20	0.17	0.22	0.23	0.18	0.21	0.23	0.22
Hf	0.00	0.00	0.00	0.02	0.02	0.00	-	0.23	0.04	0.00	0.00	0.00	0.00	0.00	0.00
Ta	0.00	0.00	0.00	0.00	0.00	0.00	0.00	0.00	0.00	0.00	0.00	0.00	0.00	0.00	0.00
Th	109	131	129	111	107	129	128	126	126	127	122	122	127	126	128
U	28.2	30.2	59.9	54.2	48.5	57.7	62.5	61.6	62.3	65.2	59.1	59.7	62.6	61.4	62.4

Sample	Sludyanka 2011					Sludyanka 2007						
ppm												
La	37.4	38.0	37.5	38.0	34.0	81.7	92.6	81.7	92.6	116.9	52.2	95.2
Ce	70.2	71.0	71.1	77.5	65.1	157	159	157	159	210	105	165
Pr	7.80	7.59	7.91	7.89	7.22	14.6	15.2	14.6	15.2	19.8	9.7	17.0
Nd	49.5	29.6	30.6	29.6	26.6	51.9	52.3	51.9	52.3	66.8	40.4	59.0
Sm	5.13	5.13	5.36	4.78	4.54	8.37	8.53	8.37	8.53	11.97	7.35	11.0
Eu	1.08	0.91	0.91	0.93	0.90	1.99	2.14	1.99	2.14	2.96	1.47	2.76
Gd	5.26	5.12	5.30	4.94	4.67	9.51	7.99	9.51	7.99	10.5	9.04	13.0
Tb	0.79	0.82	0.77	0.81	0.69	1.36	1.12	1.36	1.12	1.62	1.11	1.56
Dy	5.09	4.57	4.92	4.68	4.42	7.64	7.50	7.64	7.50	9.79	6.50	11.7
Ho	0.95	0.91	0.96	0.97	0.86	1.44	1.55	1.44	1.55	1.88	1.02	2.05
Er	2.32	2.15	2.28	2.20	1.93	4.27	4.02	4.27	4.02	4.87	3.90	5.99
Tm	0.28	0.29	0.25	0.28	0.26	0.54	0.52	0.54	0.52	0.78	0.45	0.82
Yb	1.63	1.84	1.66	1.38	1.53	3.74	3.30	3.74	3.30	3.84	6.24	3.89
Lu	0.16	0.15	0.21	0.26	0.17	0.48	0.44	0.48	0.44	0.62	0.24	0.63
Hf	0.046	0.000	0.000	0.000	0.000	-	-	-	-	-	-	-
Ta	0.000	0.000	0.000	0.000	0.000	78.2	93.7	78.2	93.7	103	128	128
Th	128	125	127	128	113	37.3	34.2	37.3	34.2	35.8	57.7	57.4
U	62.3	61.8	61.7	63.3	54.8	-	-	-	-	-	-	-

Note: A dash where a value is missing means that for that element the concentration is below the minimum detection limit.

Sample	JMH Dur pt2 2011					Durango 2007								
ppm														
La	4323	4120	3415	3634	4358	4621	3676	4642	3512	3296	3697	3854	3608	3213
Ce	4753	4607	4082	4343	4880	6207	4828	5843	4617	4448	4376	4793	4508	4186
Pr	360	348	312	331	368	502	383	458	368	348	367	404	387	349
Nd	1212	1193	1013	1072	1225	1585	1331	1484	1200	1155	1242	1322	1298	996
Sm	169	168	117	122	169	215	186	220	159	158	165	169	174	133
Eu	18.1	17.3	14.8	16.2	17.3	15.9	16.1	21.3	12.0	13.4	13.1	16.3	14.2	15.0
Gd	152	153	96.9	95.7	162	194	154	185	149	121	144	161	152	100
Tb	20.0	20.9	11.5	11.2	20.1	28.5	22.0	28.6	16.2	17.6	19.3	20.9	20.1	11.6
Dy	112	116	59.8	58.6	110	160	119	171	122	101	109	124	115	80.7
Ho	22.3	23.2	11.7	11.7	22.2	31.5	24.3	27.3	21.5	20.3	23.6	25.1	25.0	14.2
Er	58.5	60.0	29.1	29.3	57.0	92.5	63.5	80.5	65.2	61.8	57.9	64.7	61.4	31.6
Tm	7.253	7.36	3.67	3.63	7.13	12.8	7.36	10.05	9.09	6.75	7.81	8.86	8.64	3.73
Yb	43.4	44.4	22.8	23.4	42.6	51.5	50.0	51.2	46.7	31.4	42.0	49.3	47.3	32.5
Lu	5.01	4.97	3.14	3.15	4.95	6.20	5.19	7.28	6.02	5.73	4.88	5.70	5.50	5.32
Hf	0.00	0.00	0.00	0.01	0.15	-	0.00	0.56	0.39	-	0.16	-	-	-
Ta	0.00	0.00	0.00	0.00	-	342	230	310	204	219	201	222	216	169
Th	257	307	196	195	271	17	12	16	10	10	11	11	11	10
U	11.3	12.8	7.7	7.3	12.7	-	-	-	-	-	-	-	-	-

Sample	Durango 2007				
ppm					
La	3029	3260	3065	3287	3021
Ce	4070	4174	4120	4066	3869
Pr	338	322	315	320	297
Nd	1011	968	962	1049	911
Sm	100	99	112	128	118
Eu	11.7	10.7	15.5	14.0	12.7
Gd	78.0	102.4	87.1	104.3	104.3
Tb	12.3	11.6	10.4	12.5	13.1
Dy	60.7	74.1	70.8	71.1	74.6
Ho	12.9	14.2	12.8	14.2	14.2
Er	43.5	40.1	33.4	32.7	38.4
Tm	5.09	5.24	5.46	4.58	4.79
Yb	35.9	33.6	22.2	30.6	29.2
Lu	3.16	2.49	4.28	3.72	3.54
Hf	-	-	-	-	-
Ta	150	145	154	157	179
Th	9.78	7.86	6.87	6.96	11.1
U	-	-	-	-	-

Note: A dash where a value is missing means that for that element the concentration is below the minimum detection limit.

Table A-2. Zircon LA-ICP-MS 91500 standard analyses from 2001-2008 at Memorial University of Newfoundland

Sample	2001-"Harvard" JK 01500 mount 1														2002-91500	
ppm																
Sr	0.00	0.00	0.00	0.00	0.00	0.00	0.00	0.00	0.00	0.00	0.00	0.00	0.00	0.00	0.00	0.00
Y	196	123	175	171	197	170	150	175	174	154	180	150	123	138	107	115
Nb	1.28	0.79	0.73	0.70	1.27	1.23	0.86	0.63	0.84	0.15	0.92	0.62	0.78	0.71	0.51	0.68
Ba	0.00	0.00	0.00	0.00	0.00	0.00	0.00	0.00	0.00	0.00	0.00	0.00	0.00	0.00	0.00	0.00
La	0.00	0.00	0.00	0.00	0.00	0.00	0.01	0.00	0.00	0.00	0.00	0.00	0.00	0.03	0.01	0.00
Ce	3.52	2.66	3.08	3.00	3.43	3.32	3.19	3.37	3.27	3.33	3.50	2.81	2.46	2.53	1.80	2.22
Pr	0.00	0.01	0.00	0.04	0.00	0.00	0.02	0.03	0.04	0.05	0.01	0.00	0.04	0.00	0.00	0.04
Nd	0.34	0.03	0.37	0.46	0.34	0.25	0.16	0.15	0.30	0.02	0.04	0.17	0.19	0.21	0.23	0.14
Sm	0.56	0.00	0.63	0.83	0.55	0.16	0.14	0.58	0.57	0.38	0.33	0.50	0.78	0.30	0.14	0.32
Eu	0.40	0.16	0.28	0.19	0.40	0.21	0.25	0.29	0.21	0.17	0.30	0.45	0.25	0.26	0.10	0.12
Gd	3.09	1.98	2.75	3.34	3.05	2.22	2.29	2.00	2.02	2.48	2.40	2.12	2.07	2.68	0.94	1.60
Tb	1.28	0.95	1.09	1.09	1.27	1.04	1.01	1.11	1.14	1.22	1.06	1.02	0.83	0.95	0.53	0.67
Dy	13.8	9.0	12.5	14.6	13.7	12.6	11.5	13.1	11.9	10.7	13.4	11.9	12.3	12.2	8.5	9.0
Ho	6.99	4.63	6.30	6.86	6.94	6.14	5.28	6.12	5.91	6.09	6.57	5.03	4.89	5.26	3.62	3.87
Er	30.7	20.1	29.9	30.1	30.5	28.0	25.0	27.1	29.1	24.6	31.0	26.8	25.1	24.3	18.5	22.1
Tm	8.81	6.23	7.82	8.69	8.74	8.06	6.90	8.23	7.89	6.89	8.27	7.32	6.70	6.54	5.31	5.68
Yb	91.1	63.6	75.9	75.5	90.2	75.2	63.8	73.2	72.8	70.4	74.5	82.3	80.7	84.6	53.9	60.1
Lu	19.1	14.5	17.4	17.6	19.0	17.3	15.7	17.1	16.9	16.0	16.8	13.0	12.4	12.5	11.6	12.2
Hf	5895	5895	5895	5895	5895	5895	5895	5895	5895	5895	5895	5895	5895	5895	5895	5895
Ta	0.73	0.49	0.59	0.49	0.73	0.67	0.50	0.78	0.46	0.37	0.61	0.57	0.42	0.54	0.54	0.47
Pb	5.14	3.01	5.39	4.77	4.95	4.54	4.13	4.33	3.90	4.33	4.22	3.11	3.55	3.67	2.88	2.45
Th	44.2	28.2	37.8	36.6	44.5	37.9	29.5	40.2	35.5	35.0	37.2	30.9	37.3	40.5	22.9	23.6
U	115	83.3	95.3	102	111	95.2	84.2	100	92.9	95.3	97.7	86.2	104	115	61.1	63.9

Note: A dash where a value is missing means that for that element the concentration is below the minimum detection limit.

Sample	2002-91500"chip 5" study Mike T MUN mount 1									2007-JK91500 1						
ppm																
Sr	0.00	0.00	0.00	0.00	0.00	0.00	0.00	0.00	0.00	0.32	0.32	0.33	0.32	0.31	0.38	0.27
Y	118	92	100	121	124	116	122	117	106	165	157	159	156	156	163	159
Nb	0.81	0.55	0.34	0.68	0.63	0.79	0.67	0.97	0.73	0.73	0.71	0.74	0.70	0.72	0.75	0.73
Ba	0.00	0.00	0.00	0.00	0.00	0.00	0.00	0.00	0.00	0.00	0.00	0.00	0.01	0.00	0.01	0.04
La	0.01	0.00	0.04	0.00	0.02	0.00	0.00	0.02	0.01	0.00	0.00	0.00	0.00	0.01	0.01	0.01
Ce	2.16	1.99	1.95	2.45	2.39	2.05	2.28	1.99	2.44	2.98	2.93	2.94	2.97	2.99	3.10	3.07
Pr	0.01	0.00	0.01	0.00	0.00	0.00	0.01	0.00	0.00	0.01	0.01	0.01	0.01	0.02	0.02	0.02
Nd	0.19	0.00	0.00	0.06	0.20	0.34	0.46	0.33	0.05	0.29	0.20	0.25	0.21	0.24	0.28	0.19
Sm	0.22	0.09	0.33	0.46	0.35	0.11	0.38	0.01	0.30	0.45	0.44	0.42	0.41	0.56	0.41	0.39
Eu	0.16	0.12	0.13	0.18	0.17	0.18	0.14	0.16	0.13	0.24	0.26	0.24	0.24	0.27	0.27	0.28
Gd	1.76	1.27	1.06	2.16	1.47	2.73	1.82	2.15	1.60	2.45	2.32	2.38	2.36	2.57	2.80	2.58
Tb	0.72	0.39	0.56	0.66	0.58	0.60	0.55	0.56	0.58	0.88	0.84	0.87	0.88	0.94	0.88	0.94
Dy	9.5	7.5	8.5	9.4	9.4	9.3	9.7	8.6	8.7	12.9	12.5	13.1	13.2	13.0	13.6	13.7
Ho	3.87	3.21	3.34	3.93	3.90	3.76	3.83	3.67	3.53	5.19	5.12	5.21	5.24	5.30	5.58	5.57
Er	21.7	17.7	19.5	22.2	21.8	19.8	21.7	20.3	19.0	28.1	27.7	28.3	28.1	29.1	29.3	30.2
Tm	5.51	4.02	5.13	5.52	5.63	5.20	5.80	5.35	5.11	7.21	7.15	7.26	7.22	7.53	7.79	7.76
Yb	58.4	46.1	53.1	59.0	57.4	54.3	58.7	55.7	54.9	75.2	75.2	76.8	76.2	79.2	80.1	79.3
Lu	12.0	10.2	10.9	11.7	11.9	11.4	11.7	11.2	11.3	15.2	15.0	14.9	15.0	15.1	15.3	15.6
Hf	5895	5895	5895	5895	5895	5895	5895	5895	5895	5895	5895	5895	5895	5895	5895	5895
Ta	0.48	0.55	0.41	0.52	0.47	0.45	0.46	0.44	0.42	0.55	0.52	0.52	0.54	0.56	0.55	0.57
Pb	2.80	2.07	2.55	2.24	2.66	2.58	2.71	2.33	2.28	3.65	3.52	3.55	3.69	3.72	3.87	4.22
Th	23.5	19.8	20.2	23.7	23.8	23.1	24.3	22.7	23.9	34.3	34.1	34.6	34.1	35.3	36.2	35.7
U	66.2	58.9	52.9	61.5	63.7	65.1	67.8	65.4	64.1	95.9	83.0	84.4	86.1	93.4	97.4	97.9

Note: A dash where a value is missing means that for that element the concentration is below the minimum detection limit.

Sample	2007-JK91500 1														
ppm															
Sr	0.30	0.29	0.32	0.22	0.29	0.27	0.23	0.26	0.28	0.24	0.24	0.23	0.23	0.16	0.25
Y	159	150	150	144	152	142	150	146	147	150	151	147	139	145	157
Nb	0.72	1.09	0.69	0.61	0.63	0.63	0.69	0.60	1.16	1.32	0.69	0.62	1.17	1.18	1.25
Ba	0.08	0.07	0.01	0.01	0.01	0.00	0.00	0.03	0.00	0.01	0.00	0.00	0.00	0.08	0.00
La	0.01	0.00	0.00	0.01	0.01	0.00	0.01	0.00	0.02	0.01	0.01	0.00	0.01	0.00	0.02
Ce	3.12	2.96	2.86	2.88	2.86	2.85	2.95	2.90	2.80	2.91	2.73	2.99	2.71	2.73	2.95
Pr	0.02	0.01	0.01	0.01	0.01	0.01	0.01	0.01	0.01	0.01	0.01	0.02	0.01	0.02	0.00
Nd	0.28	0.20	0.25	0.21	0.23	0.23	0.14	0.27	0.12	0.32	0.22	0.15	0.16	0.32	0.18
Sm	0.30	0.41	0.44	0.44	0.45	0.47	0.31	0.42	0.54	0.33	0.43	0.43	0.41	0.30	0.56
Eu	0.24	0.21	0.23	0.23	0.32	0.25	0.27	0.25	0.22	0.23	0.23	0.17	0.22	0.30	0.25
Gd	2.43	2.44	2.10	2.02	2.19	2.01	2.63	2.51	2.22	2.46	2.13	2.21	1.90	2.32	2.55
Tb	0.94	0.93	0.83	0.80	0.87	0.88	0.86	0.84	0.88	0.97	0.87	0.92	0.81	0.79	0.86
Dy	12.8	12.2	11.9	11.4	12.8	11.4	12.0	12.0	12.2	12.8	12.5	12.1	11.6	11.8	12.2
Ho	5.32	4.97	4.89	4.59	4.95	4.61	4.95	4.80	4.83	5.33	5.05	4.95	4.67	4.85	5.20
Er	28.9	26.8	25.9	24.5	26.7	24.9	27.4	26.6	26.9	28.0	27.4	26.3	25.3	25.6	28.3
Tm	7.62	6.84	6.91	6.72	6.96	6.64	6.82	6.86	7.07	6.95	7.28	6.88	6.42	6.85	7.28
Yb	77.7	72.9	71.5	71.2	70.5	68.1	71.1	72.8	75.1	75.3	77.8	70.3	66.5	70.1	75.2
Lu	15.5	14.1	13.5	13.4	13.9	13.3	13.4	13.8	13.4	13.6	14.0	14.3	13.5	13.6	14.7
Hf	5895	5895	5895	5895	5895	5895	5895	5895	5895	5895	5895	5895	5895	5895	5895
Ta	0.58	0.50	0.56	0.47	0.54	0.52	0.52	0.54	0.52	0.56	0.54	0.52	0.50	0.48	0.53
Pb	4.10	3.64	3.54	3.38	3.23	3.23	3.29	3.58	3.41	3.64	3.73	3.33	3.13	3.16	3.38
Th	35.7	32.5	32.9	30.1	32.0	30.3	30.6	32.9	31.8	33.0	32.5	32.0	29.5	31.4	34.2
U	101	94.2	98.5	85.5	93.4	86.6	91.9	96.5	95.1	94.7	97.7	89.4	85.4	86.4	94.2

Note: A dash where a value is missing means that for that element the concentration is below the minimum detection limit.

Sample	2008-JK91500 1					
ppm						
Sr	0.15	0.21	0.29	0.29	0.22	0.36
Y	169	178	174	176	171	176
Nb	0.78	0.79	0.73	0.77	0.67	0.78
Ba	0.00	0.00	0.00	0.06	0.00	0.10
La	0.21	0.01	0.00	0.24	0.01	0.00
Ce	3.32	3.41	2.85	3.76	3.22	3.49
Pr	0.03	0.02	0.00	0.01	0.02	0.01
Nd	0.21	0.26	0.00	0.29	0.24	0.25
Sm	0.38	0.34	0.20	0.44	0.47	0.53
Eu	0.28	0.30	0.32	0.27	0.23	0.30
Gd	2.61	2.91	2.54	2.88	2.78	2.37
Tb	1.02	1.00	1.07	1.02	1.02	1.00
Dy	13.7	14.0	13.8	14.0	13.6	14.1
Ho	5.56	5.58	5.95	5.80	5.50	5.90
Er	30.3	31.3	32.6	31.3	31.7	31.5
Tm	7.73	7.74	8.09	7.93	8.18	8.04
Yb	82.9	82.8	85.7	84.4	84.0	85.8
Lu	16.6	16.2	16.6	16.2	16.4	17.1
Hf	5895	5895	5895	5895	5895	5895
Ta	0.61	0.62	0.59	0.69	0.59	0.63
Pb	3.83	4.07	4.14	4.14	4.22	4.47
Th	36.0	36.2	36.7	37.3	36.9	38.2
U	112	110	105	107	107	110

Note: A dash where a value is missing means that for that element the concentration is below the minimum detection limit.

Appendix B

See supplementary data for appendix tables:

Table B-1: Apatite LA-ICP MS

Table B-2: Apatite EPMA

Table B-3: Titanite EPMA

Table B-4: Titanite LA-ICP MS

Table B-5: Feldspar LA-ICP MS

Table B-6: Clinopyroxene EPMA

Table B-7: Whole-rock analyses from LMG and associated rocks. Modified from Valley et al. (2011)